Summer 2016

REEXAMINATION OF ORE-FORMING PROCESSES IN THE EMERY MINING DISTRICT, POWELL CO., MONTANA

Jarred Zimmerman
Montana Tech of the University of Montana

REEXAMINATION OF ORE-FORMING PROCESSES IN THE EMERY MINING DISTRICT, POWELL CO., MONTANA

by

Jarred Zimmerman

A thesis submitted in partial fulfillment of the
requirements for the degree of

Masters of Science in Geoscience
Option Geology

Montana Tech
2016

Abstract

The present investigation was undertaken in collaboration with the Montana Bureau of Mines and Geology to re-evaluate the Emery district using modern methods of ore deposit study including fluid inclusions, stable isotopes, and mineral geochemistry. Results from this thesis will be an aid in reassessing the potential of the Boulder Batholith and surrounding geologic units to host large, undiscovered precious and/or base metal deposits. The Emery (aka Zosell) district was mined from the late 1800s until the early 1950s. Mineralized quartz veins are hosted by basaltic andesite flows of the late Cretaceous Elkhorn Mountain Volcanics (EMV). Two sets of veins are present: "bedding plane" veins and east-west trending, near-vertical fissure veins. Ore mineralogy includes pyrite, arsenopyrite, sphalerite, galena, boulangerite, Ag-rich tetrahedrite, chalcopyrite, and trace electrum. Tetrahedrite is the main Ag-bearing ore mineral. Two grains of electrum were found with $X_{Au} = 0.579$ and 0.565. Electron microprobe analysis indicated the arsenopyrite locally contains gold (up to 690 ppm), and previous studies have shown high gold content in both pyrite and arsenopyrite from Emery. Gangue mineralogy was dominated by quartz during the main period of ore deposition, and by carbonate minerals (ankerite, dolomite, calcite) prior to and following the main ore-forming event. Hydrothermal alteration includes silicification and sericitization closest to the veins, grading outward to propylitic and/or carbonate alteration. The latter occurs as massive or brecciated bodies, veinlets, and as carbonate minerals replacing groundmass and phenocrysts of plagioclase and augite.

Fluid inclusion homogenization temperatures in mineralized quartz veins range from 220°C to 353°C. These temperatures fit well with K/Na geothermometry based on bulk fluid inclusion leachate analyses (averaging 302 °C) and S-isotope geothermometry based on sphalerite-galena pairs (averaging 326 °C). A temperature range of 300°C to 350°C also agrees with thermodynamic calculations based on the compositions of co-existing sphalerite, pyrite, arsenopyrite, and electrum. Two broad categories of fluid inclusions were found; aqueous-rich and CO_2-rich. The CO_2-rich inclusions show three phases at room temperature and generally have low salinity while aqueous-rich inclusions have salinity from 0 to 10.8 wt% $NaCl_{eq}$, averaging 6.2 wt% $NaCl_{eq}$. Pressure estimates based on the phase behavior of the CO_2-rich inclusions are 1.2 to 1.7 kbar while aqueous-rich inclusions indicate a pressure of 1.2 kbar. Assuming the basaltic andesite host rock is at the bottom of the EMV, lithostatic pressure would have been around 1.3 kbar during vein formation. This implies that fluid pressures may have exceeded lithostatic pressures during mineralization, especially during formation of the flat veins.

Stable S and C isotopes, combined with fluid inclusion evidence, suggest that the ore-forming event at Emery involved fluids sourced from a magma that had assimilated S and possibly C from Precambrian Belt-Purcell Supergroup metasediments. Cooling, water-rock interaction, and mixing of magmatic and meteoric water are the most likely depositional mechanisms for the Ag-Au-base metal mineralization.

Keywords: Boulder batholith, fluid inclusion, paragenesis, stable isotope, geochemistry

Dedication

I want to thank my Mom and Dad for all their support and love. I want to thank Amy for putting up with my absentmindedness while writing.

Acknowledgements

I would like to thank the MBMG and Montana Tech Geological Engineering department for financial support on this project. I would also like to thank Stan Korzeb and Chris Gammons for giving me the opportunity to work on this project. I want to thank my thesis committee Stan Korzeb, Chris Gammons and Diane Wolfgram. I also want to thank Simon Paulson (University of Nevada – Reno) and Craig Cook (UWY) for isotopic analyses of carbonate minerals. I want to thank Gary Wyss (Montana Tech) for help with SEM and XRD analyses. I want to thank Ashley Huft at the MBMG for providing bulk leachate analyses. I want to thank my fellow graduate students for collaboration:

Joshua Messenger

Kyle Eastman

Jenna Kaplan

Brandon Mus

Hamadou Gnanou

Table of Contents

List of Tables

List of Figures

1. Introduction

1.1. Purpose of Study

The Emery mining district (also known as the Zosell district) is located approximately 11 km east of Deer Lodge, Powell County, Montana. The district consists of polymetallic veins mined for base and precious metals from 1887 until 1951. Economic geology and ore mineralogy for the district was described by four Master's theses, a Bachelor's thesis, and a Montana Bureau of Mines and Geology (MBMG) Memoir. The present investigation was undertaken in collaboration with the MBMG to re-evaluate the Emery District using modern methods of ore deposit study including fluid inclusions, stable isotopes, and mineral geochemistry. Results from this thesis will be an aid in reassessing the potential of the Boulder Batholith and surrounding geologic units to host large, undiscovered precious and/or base metal deposits similar to those of Butte and Golden Sunlight.

1.2. Regional Geology

The Emery mining district is located on the western margin of the Boulder Batholith and is contained in the cogenetic Elkhorn Mountain Volcanics (EMV) (Figure 1). The EMV consists of basaltic and andesitic lava flows and breccia, rhyolitic airfall and ashflow tuff, and tuff breccia. These deposits represent the remnants of an estimated 26,000 km^2, approximately 4.6 km thick volcanic field expelled from caldera-forming eruptions (Smedes, 1966). The type area is in the Elkhorn Mountains, which border the Boulder Batholith to the northeast. The EMV has been separated into three informal units (Watson, 1986). The lower unit contains basaltic, andesitic, and rhyodacite lava flows, breccias, epiclastic, and pyroclastic rocks. The middle unit contains large, welded, rhyolitic ashflow tuff. The upper unit contains basaltic and andesitic sedimentary and pyroclastic rock. The upper unit was deposited subaqueously, whereas the

lower and middle units were deposited subaerially (Watson, 1986). Since a variety of rock types and compositions may be found in nearly every unit, the nomenclature is not concrete.

Figure 1 (next page) shows the Boulder Batholith with its main pluton, the Butte Granite, and numerous satellite plutons. The earliest plutons, dating from 80.7 to 77.3 Ma, include granodiorite of the Burton Park, Unionville, and Rader Creek plutons. These plutons are found on the northern and southern margins of the Butte Granite. The second and most voluminous group of plutons has an intermediate composition and includes the Butte Granite (two pulses at 76.7 and 74.7 Ma, du Bray et al, 2012), Climax Gulch granodiorite, Donald granodiorite, and intrusions of monzogranite. The felsic group, including Deer Creek granophyre and granophyric intrusion, was emplaced between 76.7 and 73.7 Ma (du Bray et al., 2012). It is possible that the felsic group represents a differentiated magma. The age dates imply the entire Boulder Batholith was emplaced in a 6 to 10 m.y. period (du Bray et al., 2012).

Geochemically, the Boulder Batholith has been separated into the "main series" and "sodic series". The older "sodic series" has higher Na_2O and lower K_2O concentrations than the "main series" (du Bray et al., 2012). Continuous chemical trends indicate that the majority of the EMV are related to the main series of the Boulder Batholith (including the Butte Granite, Unionville granodiorite, Moose Creek monzogranite, and granophyric intrusions).

The Boulder Batholith is bound to the north by the Garnet line and to the south by the Perry line, which also mark the northern and southern margins of the Helena Embayment of the mid-Proterozoic Belt-Purcell Supergroup (Berger et al., 2011). At the time that the EMV and Boulder Batholith were being emplaced, southwest Montana was experiencing considerable tectonism and deformation. In this area of Montana, compression was east-west creating low-angle thrust plates in the Sevier orogeny, and steep reverse faults in the Laramide orogeny.

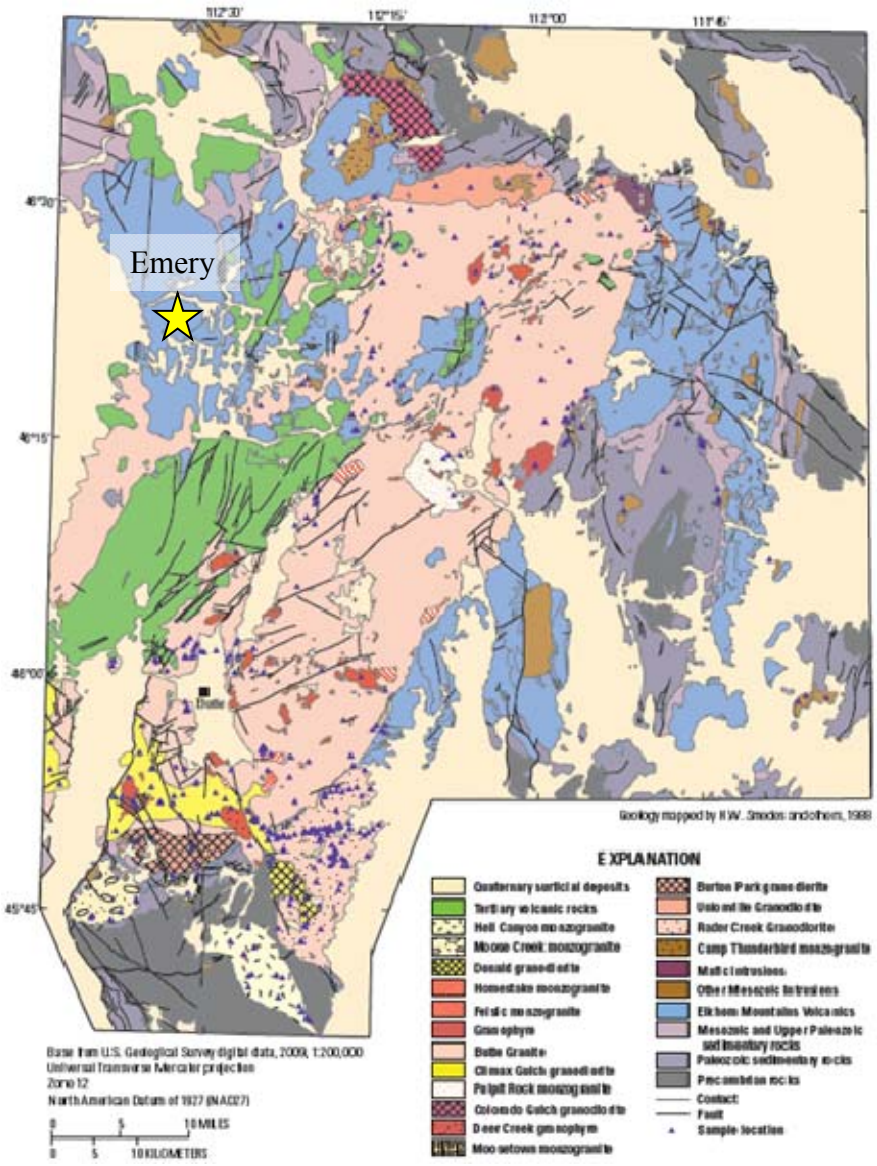

Figure 1: Geologic map of the Boulder Batholith, modified after du Bray et al., 2012

Early-stage (more mafic) magmas were emplaced at approximately the same time as over-thrust faulting and related folding were deforming the EMV and creating unconformities (Berger et al., 2011). The voluminous intermediate phase of the Boulder Batholith (nearly 70% of the total batholith volume) was emplaced in a bimodal pull-apart structure, possibly related to the Great Falls Tectonic Zone weakness being reactivated from an asymmetrically advancing thrust front (Berger et al., 2011).

The Boulder Batholith is host to many abandoned and active mining districts, including the world-class porphyry-lode deposits of Butte, Montana. With the exception of Butte, most of these mineral deposits have not been examined in detail, especially using modern methods of ore deposit investigation.

1.3. Local Geology

Robertson (1953) gave the most detailed and complete summary of the economic geology of the Emery district, and the following three sections are mainly from his work.

The Emery district is located 11 km east of Deer Lodge, Powell County, Montana (yellow star on Figure 1). Just outside the district the oldest rocks are undifferentiated and poorly consolidated Cretaceous sands, silts, and shales, but within the district the bedrock is mostly basaltic-andesite flows and breccias of the late Cretaceous EMV. Due to vegetation, poor outcrop and little variety, the volcanic flows are described by textural features such as phenocryst composition or presence/absence of vesicles and amygdules. Subtypes include pyroxene basaltic-andesite, feldspar-pyroxene basaltic-andesite, and amygdaloidal basaltic-andesite.

The most mappable feature in the mining district is a volcanic breccia horizon. The breccia outcrops as large hackly boulders and weathers to a dull brownish color. The groundmass is very fine grained with few visible phenocrysts (Robertson, 1953). Porphyritic feldspar-pyroxene basaltic andesite appears to overlie the breccia. It weathers to dark brown but unweathered samples show greenish-black groundmass with phenocrysts of labradorite (An 67) and augite with chlorite and amphibole as alteration products (Robertson, 1953). Porphyritic pyroxene basaltic andesite is dominated by pyroxene phenocrysts on hand sample scale. Plagioclase occurs in glomerophyric clusters and lath-shaped crystals. The most abundant

accessory mineral is magnetite with lesser amounts of apatite (Robertson, 1953). Amygdaloidal basaltic andesite contains amygdules of various sizes from sand size to several centimeters and number from a few percent to approximately 50 % of the total rock. The amygdules are commonly chalcedony or carbonate with hematite, chlorite, and epidote (Robertson, 1953). Red-andesite, while only minor in the district, is traceable near the Bonanza mine. It contains laths of andesine and highly chloritized amphibole and pyroxene phenocrysts (Robertson, 1953).

The most recent work completed by K. Scarberry (personal communication, 2016) describes the Emery District as dominated by lava flows probably related to the lower member of the EMV. Flows within the district are described as thermally metamorphosed with textures varying from vesicular, glassy, and aphanitic to coarse grained. The coarse-grained samples have mineral textures similar to gabbro, and may reflect longer recrystallization during metamorphism. Suspected protoliths appear to be age-equivalent to the lower member of the EMV. Breccias associated with the flows are monolithic and appear to have formed from a caldera collapse (K, Scarberry, personal communication, April, 2016).

1.4. Mineralization

Polymetallic sulfide minerals in the Emery district are found in steep fissure veins and low-angle bedding plane veins (Figure 2). The more economically important veins are located between flows in bedding plane fissures (red lines in Figure 2) which tend to follow planes of weakness between flows, most commonly in the amygdaloidal zones. The Emery-Blue-Eyed Maggie and William Coleman lodes strike northeasterly with a dip of 10° to 40° NW while the Bonanza-Hidden Hand-Argus lode strikes northwesterly with a dip of 10° to 30° NE. Ore deposition occurred during open-space filling with local reopening events (Robertson, 1953).

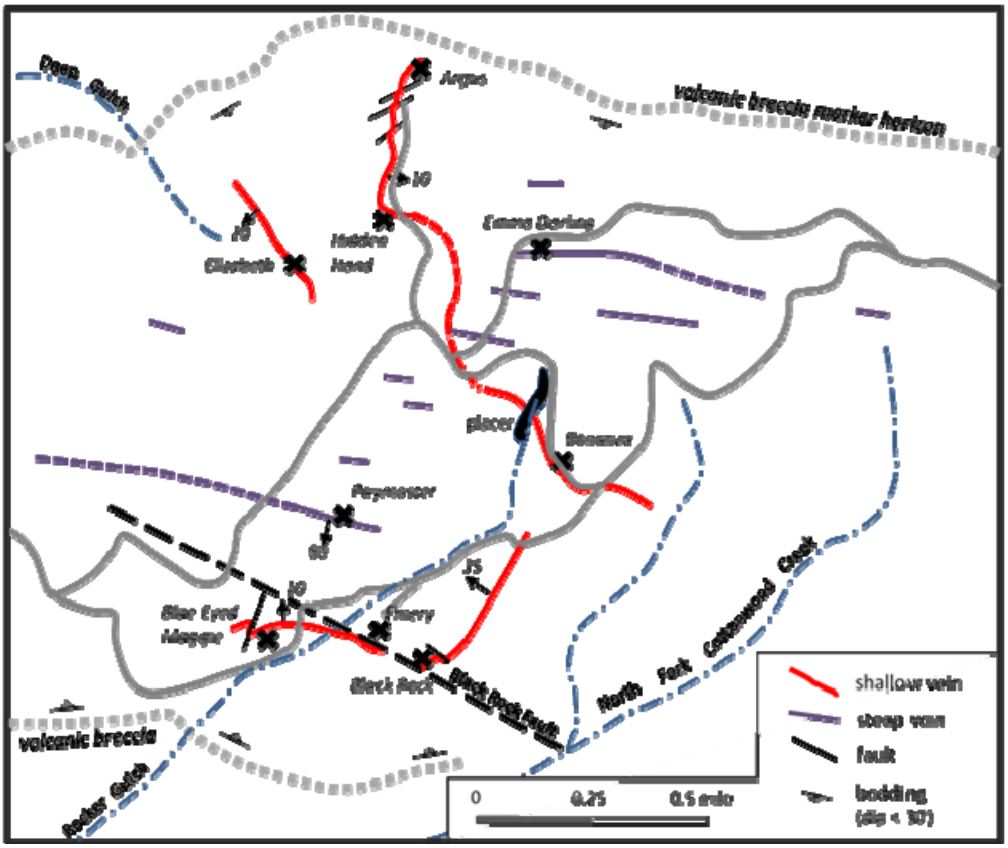

Figure 2: Map of Emery district, showing the distribution of major veins and mines. Geology from Robertson, 1953.

Nearly-vertical veins (purple lines in Figure 2) appear to have formed at approximately the same time as the bedding plane fissures. The near-vertical veins, characterized by the Black Eyed May-Emma Darling, Sterret, and Swan-Sabbath veins, trend N 100° E and appear to occupy normal tension fractures. Direction and magnitude of movement along these structures is unknown, however, some appear to have significant lateral persistence (Robertson, 1953).

The ore and gangue mineralogy for both styles of vein are similar. The veins have a quartz-carbonate gangue, with common sulfides including pyrite, arsenopyrite, sphalerite, galena, chalcopyrite, boulangerite ($Pb_5Sb_4S_{11}$), Ag-bearing tetrahedrite ($(Cu,Ag)_{10}(Fe,Zn)_2SbS_{13}$) and electrum. Timing of vein mineralization is not known but it is presumed by previous workers to be late Cretaceous, roughly overlapping with the Boulder Batholith intrusion (Robertson, 1953).

1.5. Mining History

In 1872, H. L. Hoffman discovered placer gold deposits in Rocker Gulch, Deep Gulch, and a tributary of Little Cottonwood Creek near the Sterret mine (only one placer location is marked on Figure 2). These deposits were not extensive, rarely larger than 3 m deep and 15 m wide, or unusually rich with total placer production between $1,280,600 and $1,707,450 adjusted for inflation (CPI Inflation Calculator, 2016). Except for 2 ounces panned in 1933, placer mining ceased in 1889 (Robertson, 1953).

Lodes were not discovered in the district until the late 1880s. The Hidden Hand lode was the first to be discovered in 1887 by Joe Peterson. The most economically important lode, the Emery mine, was discovered by John Renault in 1888 and the Bonanza lode (second most economically important) was discovered in 1895. Between 1891 and 1905 the rest of the principal lodes, Blue Eye Maggie, Argus, Emma Darling, and more, were discovered (Robertson, 1953).

Mining activity decreased around 1908 and 1909 without much increase until the late 1930s when the Tweedy Brothers Corp. operated the Emery mine but this increased activity was short lived (Robertson, 1953). World War II made obtaining mine equipment impossible and greatly increased the cost of labor. Shortly after WWII ended the district was able to produce concentrates, probably due in part to the high price of lead. However, once again, production was short-lived due to the recession of 1949. By 1951, rising costs of labor and material had closed most of the properties with only the Hidden Hand mine in operation. The winter of 1951 saw the close of the district, with the death of Mr. Howard, owner and operator of the Hidden Hand mine (Robertson, 1953).

Table I (Robertson, 1953) shows production from 1928 to 1948. Details are not available for production prior to 1928. From the information available, production before 1928 is

estimated at no less than $5,989,000 (corrected for inflation) (Robertson, 1953). Total lode production for the district is therefore estimated between $24,600,000 and $29,500,000 (corrected for inflation) with roughly 85% of the value from gold and silver, 10% in lead, and the remainder in zinc and copper (Robertson, 1953).

Table I: Production from 1928 to 1948

Gold	21,906 oz
Silver	591,062 oz
Lead	1,399,980 lbs
Zinc	681,200 lbs
Copper	26,020 lbs

1.6. Previous Work

In addition to the comprehensive report by Robertson (1953), several theses have also been completed on the Emery District. The earliest, by Elliott (1939), focused on the Emery mine. He described the Emery lode's structure and mineralogy. Elliott was also the first to describe the host rock. Stejer (1948) was the first to describe the Bonanza lode in terms of structure, mineralogy, and possible source of mineralizing fluids. Callaway (1950) described the Bonanza mine by expanding on mineralizing hydrothermal fluids and alteration styles associated with said fluid. Joyce (1951) completed a paragenesis study on the ore minerals of Argus, Hidden Hand, Black Eyed May, and the Emma Darling mines. Al-Khirbash (1982) utilized core from two boreholes to find a possible origin of the mineralizing fluid for the entire district and possible exploration targets using metal ratios. At the present time the author is collaborating with the MBMG, specifically Stan Korzeb, who is interested in re-evaluating the economic geology of the Boulder Batholith, and Kaleb Scarberry, who mapped the Sugarloaf Mountain quadrangle and evaluated the volcanic host rock. Preliminary results of these joint studies have been presented at a number of meetings (Korzeb et al., 2015, 2016; Scarberry, 2015).

1.7. Thesis Objectives

The focus of this thesis was to obtain a more complete understanding of the mineralization in the Emery District. Samples were collected for fluid inclusion analysis, stable isotopes (S from sulfides and C-O from carbonates), alteration and mineralization petrography, mineral chemistry, and geochemical modeling. Fluid inclusion and S-isotope data were used to determine temperature of formation and approximate depth. These analyses can also help delineate various mineralizing stages. A comprehensive mineralogical study with geochemical aspects delineated where metals of interest (Au, Ag, etc.) are found. When paragenesis is compared with fluid inclusion and stable isotope data, temperature of mineralization and fluid chemistry can be constrained.

2. Methods

2.1. Petrography

Thin sections and polished sections were selected from hand samples collected from waste rock dumps. Samples were cut and analyzed with a Niton XL3t pXRF Analyzer for Au, Ag, high concentrations of base metals (Pb, Zn, Cu), and any anomalous readings. Areas that fit the criteria were used for further analysis.

Representative hand samples were sent to the Sample Preparation and Thin Section Laboratory at the University of Utah, Salt Lake City, Utah and were completed by normal thin section means. Samples were chosen to represent the alteration styles. Some of these samples with larger amounts of sulfide minerals were polished for analysis on SEM-EDX and reflected light microscopy as well as transmitted light. Other thin sections had a cover slip.

Polished epoxy mounts were prepared at Montana Tech on a Buehler Automet 250 autopolisher. Samples were chosen from vein sections and alterations to examine the ore minerals. Thin sections and polished plugs were examined on an Aus Jena petrographic microscope with reflected and transmitted light capabilities. The following abbreviations are used throughout this thesis for petrographic analysis: PPL (plane polarized light), XPL (crossed polarized light).

2.2. Fluid Inclusions

Doubly polished thick sections were polished to 8 μm before being affixed to petrographic slides with superglue and excess sample removed using a Buehler Isomet Slow Speed Saw leaving approximately 100 μm thick section; if necessary the thick section was thinned. The new face was polished to 8 μm on a Buehler Automet 250 autopolisher. Once polished the thick section was left overnight in an acetone bath to remove the superglue and

epoxy. The sample was carefully cleaned of residue with water. Entire thick sections were examined under an Olympus BH-2 microscope to identify fluid inclusion populations for study. Thick sections were cut on the Buehler Isomet Slow Speed Saw to make chips small enough for analysis.

The following abbreviations are used throughout this thesis for fluid inclusion analysis: Tm_{ice}, temperature of melting of water ice; Tm_{clath}, temperature of melting of CO_2 clathrate; Th_{CO2}, temperature of homogenization of CO_2(l) and CO_2(v) to a single CO_2 phase; Th, temperature of total homogenization; Td, temperature of decrepitation; Tf, temperature of water freezing; Tme, temperature of eutectic melting of ice.

Fluid inclusion analyses were completed on an Olympus BH-2 microscope with a modified U.S.G.S gasflow stage connected to a Fluid Inc. Doric 400 Series trendicator, as shown in Figure 3. Liquid nitrogen from the dewer was blown across the stage in a stream of N_2 to quickly freeze the fluid inclusions to -100 °C. The chip was then warmed quickly to -10 °C and then warmed at 1 °C per minute until Tm_{ice}. Fluid inclusions were frozen between 2 and 5 times to get an average. The accuracy of the thermocouple was checked by freezing synthetic fluid inclusions of pure water. The measured Tm_{ice} was within ± 0.1 °C of 0.0 °C.

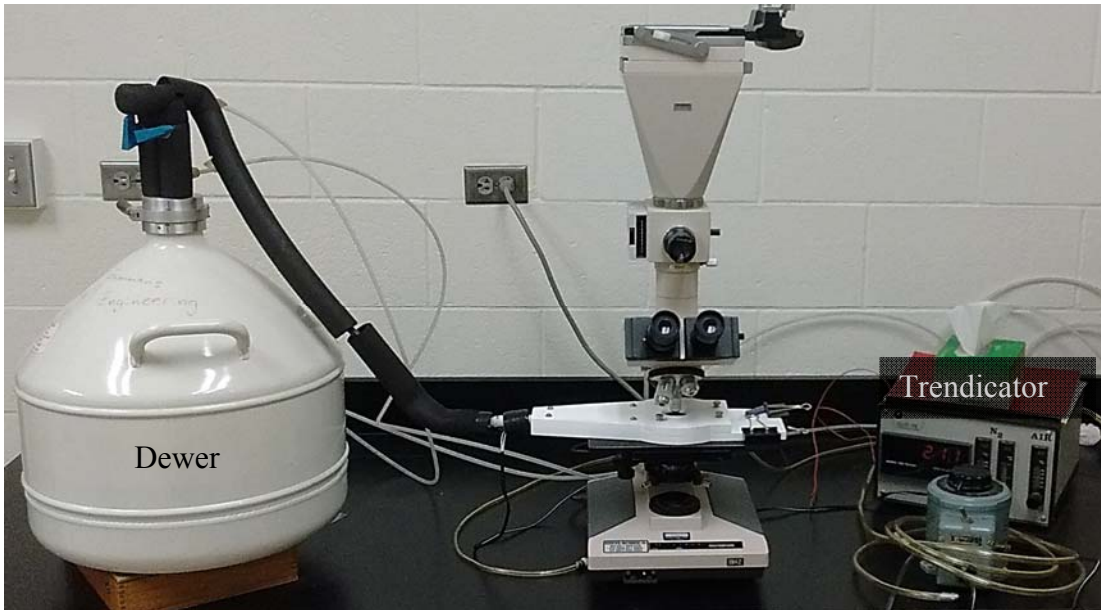

Figure 3: Modified U.S.G.S. gas-flow stage with dewer and trendicator.

If an inclusion formed a clathrate, Tm_{ice} was measured first (if possible) and temperature was raised 1 °C per minute until Tm_{clath}. Clathrate melting is expected to be between -10 and +10 °C. Tm_{clath} analyses were repeated between 3 and 5 times due to increased rates of decrepitation at lower temperatures.

Heating runs were completed after freezing runs because heating runs commonly caused the inclusions to decrepitate, stretch, or leak, thus altering the fluid and making results unreliable. During heating runs the temperature was increased quickly until the fluid inclusions began to show signs of homogenization. If the inclusion was 3 phase (liquid CO_2 + V+ H_2O (l)), the Th_{CO2} was recorded by increasing the temperature 0.5 °C per minute until the carbonic phase homogenized. Runs were repeated between 2 and 4 times to get an average.

For total homogenization (Th) the temperature was increased quickly while focusing on a field of inclusions until the vapor bubbles began to shrink. The temperature was increased 1 °C per minute until the lowest Th of the various inclusions in the field of view. The inclusion was allowed to cool and nucleate a vapor bubble before reheating for a second measurement of Th. If

the numbers were fairly close the temperature was accepted. If the numbers were off by more than 3 °C, the Th measurement was retested. If the Th changed significantly (more than 5 °C) with each reheating the inclusion was not reliable but the data was noted. The accuracy of the Th measurements was checked by homogenizing synthetic fluid inclusions trapped at the critical point of pure water. The Th values obtained were within ±1 °C of 374 °C.

2.3. Bulk Leachate

Quartz samples were selected for the probability of higher numbers of fluid inclusions based on structures such as comb and massive. Samples were ground in a porcelain mortar and pestle. Between 5.3 g and 6.7 g were placed in vials and enough deionized water was added to cover the sample. After a week of occasional agitation, the excess water was sampled and filtered through a 0.20 μm filter before being acidified with 10 drops of HNO_3. Analysis was completed at the MBMG Analytical Lab by Ashley Huft on a Thermo iCAP ICP-OES. Following this method it is not possible to determine the concentrations of individual solutes; only the cation ratios can be obtained.

2.4. Stable Isotopes

Isotope samples were chosen from hand samples and slabs. Grains were hand-picked or drilled out using a Dremmel drill under a binocular microscope to avoid contamination. Sample sizes from 2 to 5 mg were used. The sulfur isotopes were analyzed at the USGS Crustal Geophysics Geochemistry Center Stable Isotope Laboratory, Denver, Colorado using a VG Series mass spectrometer. Analytical uncertainty is estimated to be ± 0.1 ‰ for $\delta^{34}S$. Isotopes were measured against VCDT.

Carbonate mineral separates were sent to the University of Nevada – Reno for measurement of $\delta^{13}C$ and $\delta^{18}O$ on a dual inlet Micromass IsoPrime stable isotope ratio mass

spectrometer. Analyses were performed using the McCrea (1950) phosphoric acid reaction method at 90 °C. Analytical uncertainty is estimated to be ± 0.1 ‰ for $\delta^{13}C$ and ± 0.1 ‰ for $\delta^{18}O$. Carbon isotopes were measured against VPDB and oxygen isotopes against VPDB and VSMOW.

Another set of carbonate mineral separates were sent to the University of Wyoming for measurement of $\delta^{13}C$ and $\delta^{18}O$ on a Thermo Gasbench coupled to a Thermo Delta Plus XL IRMS. Analyses were performed following the procedure below, taken from (http://www.uwyo.edu/sif/instrumentation/gas-bench.html)

> "$\delta^{13}C$ and $\delta^{18}O$ ratios in carbonate minerals can be determined simultaneously by the analysis of CO_2 generated by the reaction of carbonate with 100% phosphoric acid. Headspace vials are used to process carbonate samples. A known mass of sample is placed in the headspace vial, dried overnight and then flushed with helium. A quantity of 100% phosphoric acid is then added. Depending on the carbonate material, the reaction is allowed to proceed for 24-48 hours. All of the carbon ends up in the headspace of the vial in the form of CO_2 gas, so that the $\delta^{13}C$ of the CO_2 gas is equivalent to that of the carbonate. Oxygen is partitioned both into water and CO_2 so that a calculation is required to get the isotopic composition of the carbonate from the CO_2 gas. The headspace CO_2 is analyzed using the GasBench attached to an isotope ratio mass spectrometer (GC-IRMS)."

Analytical uncertainty is estimated to be ± 0.1 ‰ for $\delta^{13}C$ and ± 0.1 ‰ for $\delta^{18}O$. Carbon isotopes were measured against VPDB and oxygen isotopes against VPDB and VSMOW.

2.5. XRD

Carbonate mineral separates were powdered in mortar and pestle for analysis on a Rigaku Ultima IV X-Ray diffractometer (XRD) in the CAMP laboratory at Montana Tech by Gary Wyss. Operating conditions were 20 degrees per minute from 5 to 90 degrees with a 40 kV acceleration voltage and 44 mA probe current.

2.6. SEM

SEM analysis was completed at Montana Tech with the assistance of Gary Wyss on a LEO 1430VP with two energy dispersive X-ray detectors (EDX), shown in Figure 4. Samples were carbon coated prior to analysis. Operating conditions were 25 kV acceleration voltage, 17 to 19 mm working distance, 550 nm^2 spot size, and 100 μA beam current. EDX spectra was collected by two Apollo 40 detectors with a 3.3 window type and collection rate of 35,000 to 55,000 counts per second. Collection time ranged from 10 to 30 seconds with a dead time of 25 to 30 %. A ZAF correction factor was used as a standardless calibration for the EDX analyses and accounts for atomic number, fluorescence, and absorption effects.

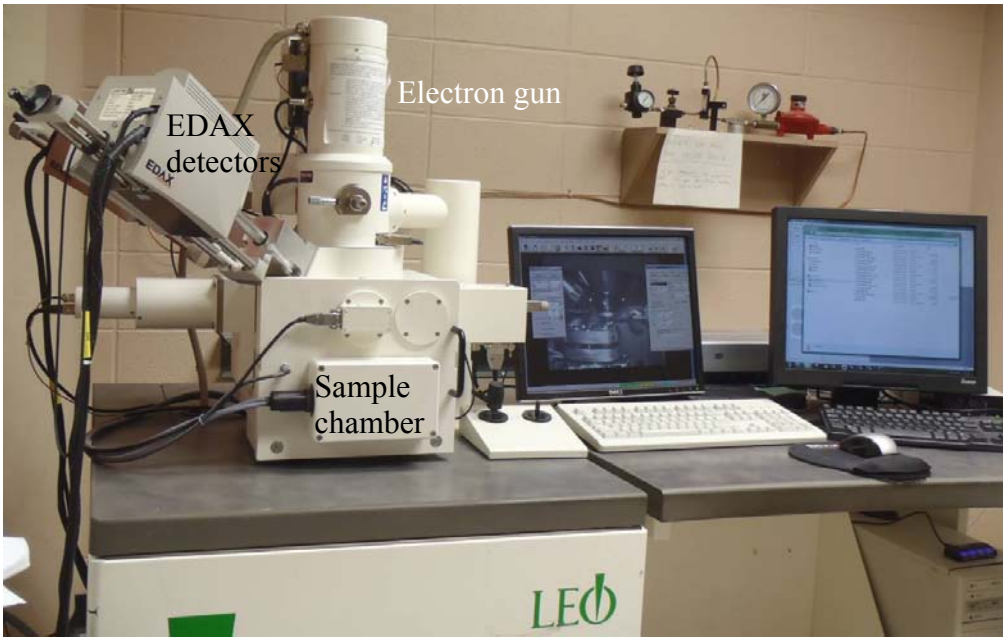

Figure 4: Scanning electron microscope at Montana Tech

2.7. EPMA

Electron probe microanalysis (EPMA) was completed on a single ore specimen from the Emery mine at Washington State University's GeoAnalytical Lab on a JEOL JXA-8500F. Quantitative analyses were obtained for a representative set of ore and gangue minerals using standardized WDS (wavelength dispersive spectrometry). Peak counting time for Sn, Zn, Cd, Pb, Fe, Cu, S, Sb, Ag, and Bi was 20 seconds while Au was 40 seconds and As was 120 seconds. Accelerating voltage was 20 kV with a beam current of 30 nA and a beam size of 1μm. Further details on the calibration procedures and operation conditions for EPMA analysis are presented in Table II.

Table II: EPMA calibration

Instrument	Intensity Correction	Accelerating Voltage (kV)	Beam Size (μm)
JEOL JXA-8500F, WSU GeoAnalytical Lab	ZAF (Armstrong-Love/Scott)	20	1

Element	**Peak Counting Time (s)**	**Low Background Counting Time (s)**	**High Background Counting Time (s)**	**Analyzing Crystal**	**Calibration Standard**
Sn	20	10	10	PETJ	Cassiterite #3 (C.M. Taylor)
Zn	20	10	10	LiFH	ZnS (C.M. Taylor)
Cd	20	10	10	PETJ	CdS (C.M. Taylor)
Pb	20	10	10	PETJ	PbS (C.M. Taylor)
Fe	20	10	10	LiFH	Hematite #2 (C.M. Taylor)
Cu	20	10	10	LiFH	Chalcopyrite #2 (C.M. Taylor)
S	20	10	10	PETJ	ZnS (C.M. Taylor)
As	120	60	60	TAP	Arsenopyrite
Sb	20	10	10	PETJ	Sb_2Te_3 (C.M. Taylor)
Ag	20	10	10	PETJ	Ag (C.M. Taylor)
Au	40	20	20	PETJ	Au (C.M. Taylor)
Bi	20	10	10	PETJ	$Bi_{12}GeO_{20}$ (C.M. Taylor)

2.8. microRaman

Raman spectroscopy was performed at Montana Tech on a Renishaw inVia Raman Microscope. Exposure time was 0.5 seconds at 32 accumulations with a 10 second photobleach to remove fluorescence from the quartz medium. Scans were completed using the 633 nm laser. Raman images were taken with a Renishaw CCD camera. The Raman was used to qualitatively discern the presence of CO_2 (l).

The program WiRE 4.1 identified peak positions of single scans. Raman spectra were reanalyzed by CrystalSleuth, part of the RRUFF Project created by Bob Downs and Tom Laestch from the Department of Geosciences at the University of Arizona.

2.9. TerraSpec Halo

Alteration assemblages were examined using a PANalytical TerraSpec Halo mineral analyzer. The TerraSpec Halo is a full-range near – infrared (NIR) spectrometer measuring wavelengths from 350 to 2500 nm. To minimize the effect of weathering, scans were completed on rough sawn surfaces. Terminology used includes: mineral, scalar, and stars. The TerraSpec displays a maximum of four minerals at a time. Certainty of the minerals displayed is indicated by the number of stars (1 to 3). Scalars are applied to help characterize the crystallinity of certain minerals, such as white micas and clays that can form over a wide range of conditions. The most important scalar for this study was ISM (Illite Spectral Maturity). The ISM scalar was only used qualitatively in the sense that ISM inversely relates to temperature, therefore, the higher ISM values (> 1) were related to low temperature alteration while the low numbers (< 0.9) represent high temperature alteration.

Some minerals have extra letters associated (Kaolinite WX/PX) that further describe the mineral. WX indicates a well crystalline mineral and PX indicates a poorly crystalline mineral. These separate the kaolinite into hypogene alteration (WX) and weathering (PX).

2.10. pXRF

A Niton XL3t portable X-ray fluorescence (pXRF) analyzer was used to identify areas of interest in vein and alteration samples by scanning for high concentrations of precious and base metals as well as other elements. Scan times were between 60 and 65 seconds. The scan spot size was 3 mm. The pXRF can detect the standard analytical range (25 elements from S – U) as well as Rare Earth Elements (REE) and Mg, Al, Si, and P.

3. Results

3.1. Paragenesis

Figure 5 shows the paragenesis of the Emery mining district as determined through thin and polished section petrography, SEM-EDX, and XRD. Overall, the vein mineralogy found in this study was similar to that reported in previous works. Dashed lines represent some uncertainty in deposition. For example, only one instance of meneghinite and bournonite was found during the study making timing of deposition uncertain. The early carbonate stage was the beginning of the paragenetic sequence with deposition of quartz and carbonates. Stage 1 was the start of metal deposition with Fe, As, and Au while Stage 2 had a wider range of elements (Pb, Zn, Sb, Fe, Cu, Ag, Au). The late carbonate stage was dominated by carbonate minerals with a possible trace of chalcopyrite. Quartz was deposited throughout the evolution of the system.

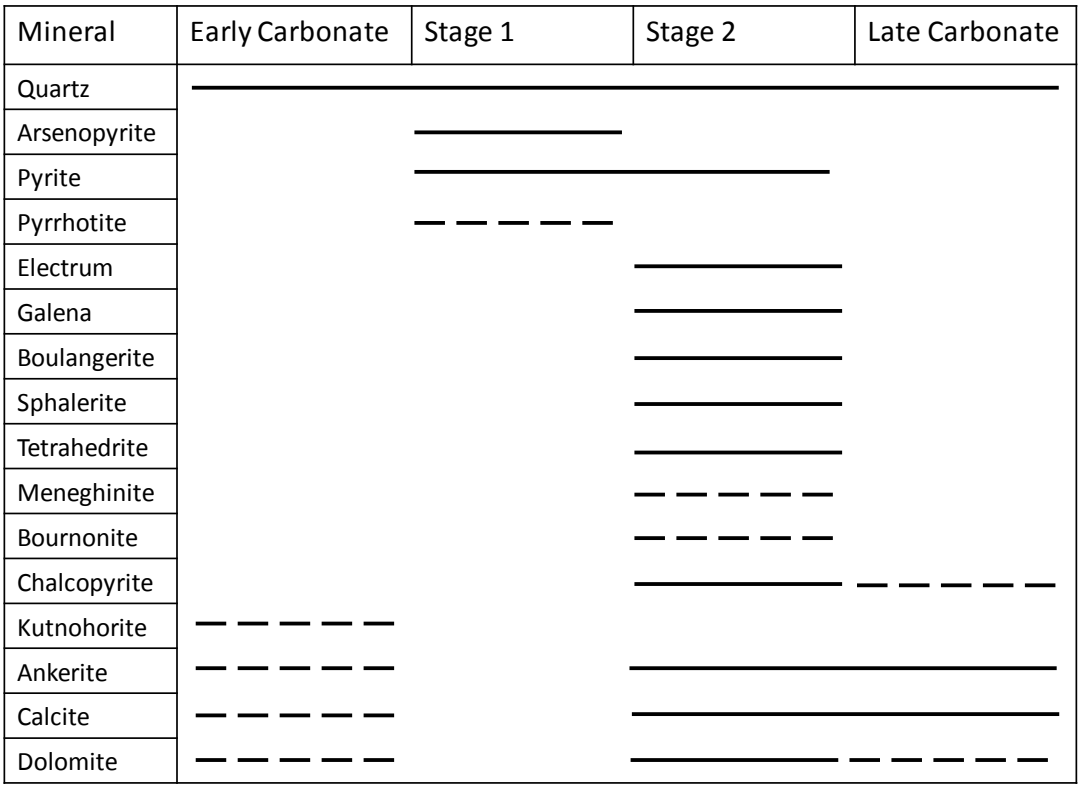

Figure 5: Paragenesis diagram. Solid lines represent certainty while dashed represent relative uncertainty due to replacement textures.

The early carbonate stage began with the introduction of CO_2-rich fluids (described by fluid inclusion types 2 through 4a, see Figure 13) and the deposition of quartz, kutnohorite ($Ca(Mn, Mg, Fe)(CO_3)_2$), ankerite ($Ca(Fe^{2+}, Mg)(CO_3)_2$), calcite, and dolomite. Many of the early carbonate minerals were replaced during Stages 1 and 2 creating uncertainty in the original mineralogy.

Stage 1 was the beginning of metal deposition. The minerals for Stage 1 are arsenopyrite, pyrite, and quartz. Some pyrrhotite was also found during thin section analysis as very small inclusions in pyrite. Pyrrhotite is assumed to be Stage 1 due to conditions (higher T and low sulfur fugacity) necessary for stabilization. Textures indicate open-space filling by euhedral comb quartz and euhedral arsenopyrite. Pyrite is also found disseminated in the wallrock from sulfidation of Fe-bearing minerals. EPMA analyses indicate that arsenopyrite locally contains considerable Au and fire assays completed by Elliott (1939) corroborate the finding and also indicate the existence of gold in pyrite. Because no discrete gold or electrum phases were found in pyrite or arsenopyrite host minerals, the Stage 1 gold is probably submicron in size.

Stage 2 is characterized by Pb-Zn-Sb-Cu-Ag-Au. The main ore minerals deposited during Stage 2 were galena, sphalerite, boulangerite, tetrahedrite, and chalcopyrite. Nearly all of the minerals can be found replacing or included in another making timing of deposition difficult to discern. Figures 6B and 6C illustrate how intergrown Stage 2 minerals can be. Figure 6B shows a euhedral crystal of arsenopyrite included in galena being replaced by bournonite ($CuPbSbS_3$) with a meneghinite ($CuPb_{13}Sb_7S_{24}$) intermediate phase. The adjacent quartz displays dissolution, most likely from the bournonite producing fluid. Figure 6C shows patches of galena intergrown with boulangerite. The large grain in the bottom shows two stages of

tetrahedrite (Ag-rich tetrahedrite and freibergite) with boulangerite. The two compositions of tetrahedrite are separated by their Ag content; the lighter color is freibergite and the darker color (also the larger portion) is Ag-rich tetrahedrite. The matrix is Fe-rich dolomite with boulangerite and galena.

Two grains of electrum found in the present study are presumed to be from Stage 2 since both grains are included in Ag-rich tetrahedrite. Figures 7B and 7C are backscatter electron images from EPMA of the electrum grains found during this study. Figure 7B shows an inclusion of electrum near the border of coarse grained sphalerite and Ag-rich tetrahedrite. The sphalerite has "chalcopyrite disease". Figure 7C shows an inclusion of electrum and sphalerite surrounded by Ag-rich tetrahedrite.

The closing stage of the hydrothermal system was nearly completely gangue minerals. During the late carbonate stage the relative ratio of quartz to carbonate (ankerite, dolomite, calcite) shifts from quartz as the most abundant gangue mineral to carbonate. There was one instance of a small chalcopyrite grain included in a late carbonate breccia, lending to the dashed line extending into the late carbonate stage (Figure 5).

3.2. Ore Minerals

Arsenopyrite (FeAsS) is found in Stage 1 and is associated with pyrite and quartz (Figure 9A). The arsenopyrite is usually found as euhedral crystals as shown in Figure 7D, however, it can occur as massive or individual subhedral crystals (Figures 9C and 9E). Arsenopyrite exhibits slight replacement with respect to most of the mineral assemblage, except boulangerite (Figure 9A). Figure 9A displays the earlier arsenopyrite and euhedral quartz surrounded and replaced by patches of anhedral boulangerite. The boulangerite is in turn being replaced by later carbonate minerals (Figure 9B). Figure 7D shows arsenopyrite surrounded by Ag-rich

tetrahedrite (light gray) with sphalerite (dark gray) in a matrix of quartz. Even though it is confined to one stage of the system, the amount of arsenopyrite is abundant compared to other sulfide minerals. Elliott (1939) found the arsenopyrite to be the main source of Au at 20.3 ppm. EPMA data (Table V) indicates the As concentrations of arsenopyrite vary between 29 and 30 atomic %. The arsenopyrite crystals have Au below detection of the EPMA instrument except for one scan which had 690 ppm Au, indicating that the arsenopyrite may contain gold as posited by Elliott (1939).

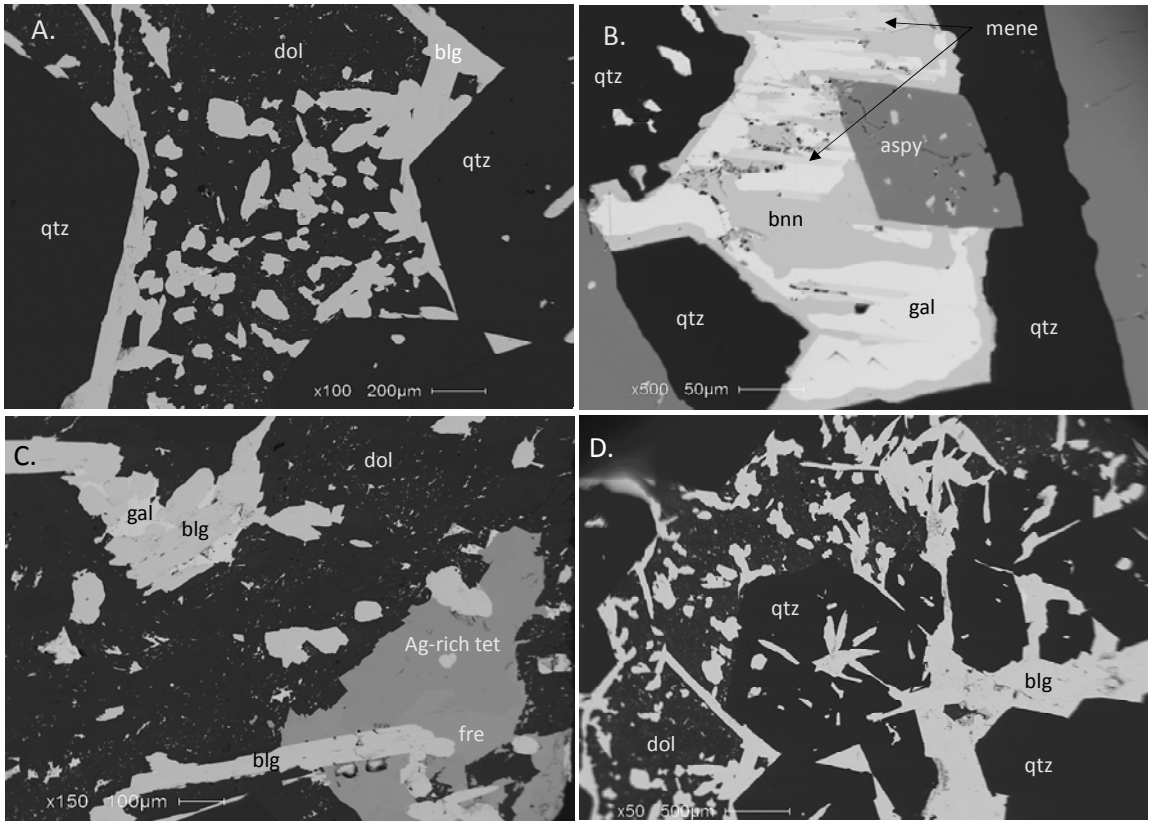

Figure 6: SEM-BSE images of ore minerals from the Emery mine. A) Boulangerite (blg) and dolomite (dol) filling space between euhedral quartz (qtz) crystals. B) Euhedral arsenopyrite (aspy) surrounded by galena (gal), bournonite (bnn) and meneghinite (mene). C) Patches of intergrown blg and gal, with a lath of blg included in Ag-rich tetrahedrite (Ag-rich tet) and freibergite (fre). D) Same as A.

Pyrite is a very common mineral in nearly every stage of the paragenesis. It is found from Stage 1 through late carbonate deposition and as an alteration product. Crystals of pyrite range from cubic structures to aggregate masses. In vertical veins the pyrite can be found in

brecciation seams and in low angle veins overpressure brecciation occurs. Slightly anisotropic crystals have been found but are uncommon. The anisotropy may be due to polishing. Pyrite in the deposit has been noted by Elliott (1939) to contain low level Au and Ag.

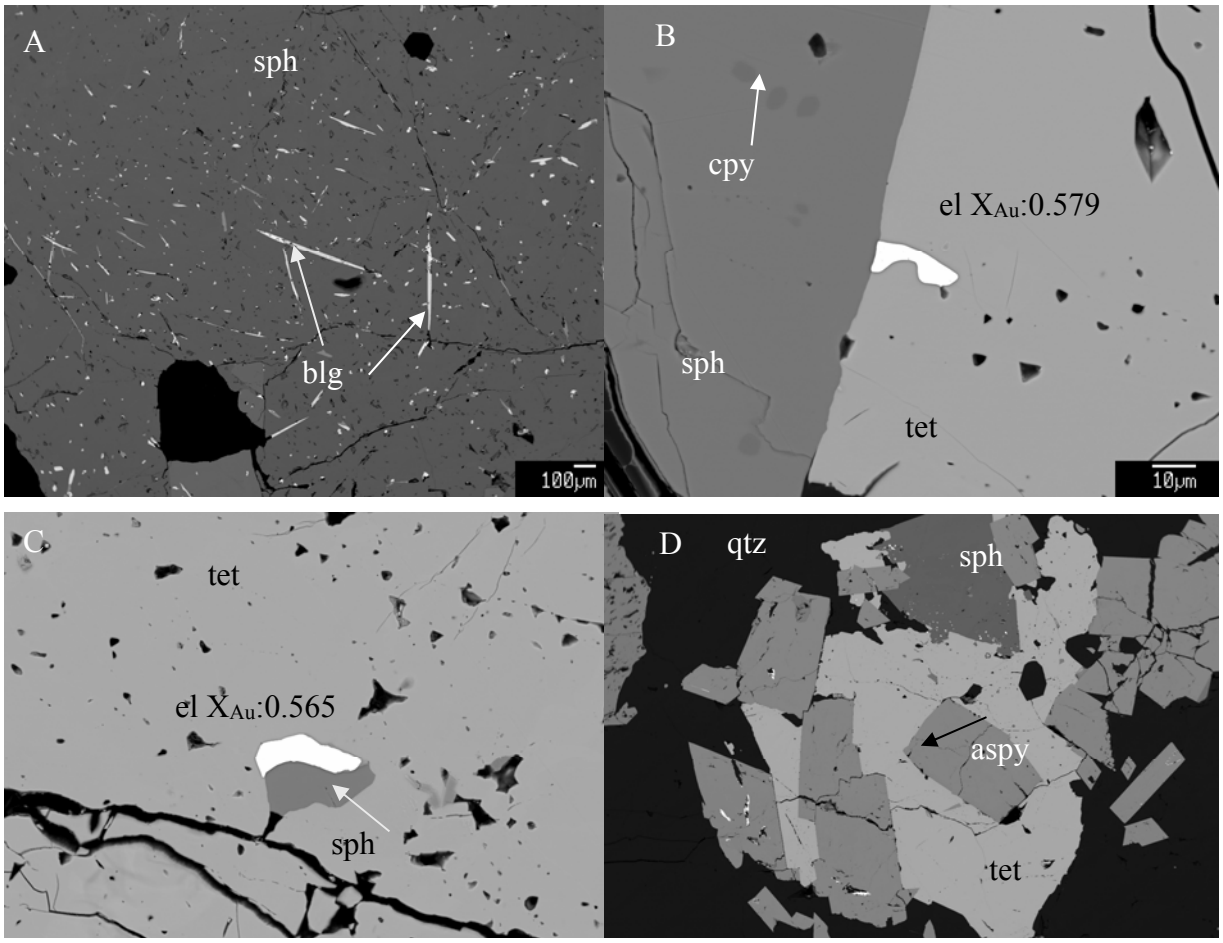

Figure 7: EPMA images of sphalerite, boulangerite, electrum, arsenopyrite from the Emery mine. A) Boulangerite (blg) needles included in sphalerite (sph). B) Grain of electrum (el) on the boundary between sph and Ag-rich tetrahedrite (tet). Note the four grains of chalcopyrite (cpy) in the sph. C) Grain of el next to sph in tet. D) Euhedral and subhedral aspy included in tet with a grain of sph in a groundmass of qtz. The bright spots in the aspy are needles of boulangerite.

Galena (PbS) occurs as irregular patches with characteristic triangular pits and islands in later Pb-sulfide/sulfosalt minerals and carbonate (Figure 9B). Galena shows deformation through curved cleavage planes and bent triangular pits. Due to preferential replacement, only a small grain of galena is left in Figure 9A. Sb and Ag are the only impurities indicated by SEM-EDX (Table IV). No galena grains were analyzed by EPMA. Elliott (1939) indicated that

galena may be a source of silver (1860 ppm). SEM-EDX data in the study showed two grains with Ag concentrations of 1500 ppm and 11900 ppm. The latter analysis may have had a small inclusion of an unknown Ag-bearing mineral.

Sphalerite ($Zn_{.94-.88}Fe_{.06-.12}S$) is found as irregular masses that are often included (Figure 9D and 9E). The sphalerites are very dark red-brown due to high Fe content (X_{FeS} = 0.06 to 0.12, n=6) according to EPMA and SEM data (Table III). Under transmitted light one sees patches of amber to deep red where rare fluid inclusions, too small to analyze, may occur. Cd ranges from 0.3 to 0.4 wt%. The sphalerites have "chalcopyrite disease" as well as included boulangerite, as seen in Figure 7B and 7A, respectively.

Table III: Analysis of sphalerite

Sample	Zn	Cd	Pb	Fe	Cu	S	Mn	Ideal Formula
EPMA								
Sphal	58.705	0.405	BDL	6.472	0.025	32.875		$(Zn_{.88}Fe_{.11})S$
Sphal	58.812	0.416	0.067	6.528	BDL	33.537		$(Zn_{.88}Fe_{.12})S$
Sphal2	60.765	0.414	BDL	3.048	0.613	32.859		$(Zn_{.93}Fe_{.05})S$
Sphal3	59.027	0.336	BDL	5.189	0.190	33.300		$(Zn_{.90}Fe_{.09})S$
Sphal3	61.246	0.402	BDL	3.325	0.275	33.140		$(Zn_{.93}Fe_{.06})S$
SEM								
Sphal	62.110			5.980		31.040	0.87	$(Zn_{.89}Fe_{.10}Mn_{.01})S$
Sphal2	59.480			6.500		33.050		$(Zn_{.89}Fe_{.11})S$
Sphal3	64.700			3.150		32.130	0.02	$(Zn_{.95}Fe_{.05})S$

Values in wt%

Chalcopyrite ($CuFeS_2$) can be found as "chalcopyrite disease" in sphalerite, interstitial grains in coarse comb structure quartz, minor crystals in veinlets, and one occurrence in a carbonate breccia as a rounded bleb. Figure 7B shows a sphalerite (dark gray) with "chalcopyrite disease," notice the slightly darker regions within the sphalerite. The chalcopyrite is nearly always anhedral, as displayed in Figure 9C. Al-Khirbash (1982) noted the minute amount of chalcopyrite, and described it as intergrown with pyrrhotite as well as with quartz in

the final stage of metal deposition. However, the only pyrrhotite found in the present study was found as small inclusions in pyrite, and is interpreted to be early in the vein paragenesis.

Tetrahedrite has been found to be the primary Ag-bearing mineral. It occurs as irregular masses. Table V indicates Ag ranges from 3.8 to 4.4 atoms per formula unit, indicating that some of the tetrahedrite is freibergite ($((Cu_{.56}Ag_{.44})_{10}(Fe_{.63}Zn_{.37})_2(Sb_{.97}As_{.03})S_{13}$) and some is Ag-rich tetrahedrite. The two phases of tetrahedrite are separated by their Ag content. The freibergite has 4.4 atoms per formula unit (a.p.f.u.) while the Ag-rich tetrahedrite has 3.8 a.p.f.u. According to Moëlo et al. (2008) the separation between Ag-rich tetrahedrite and freibergite is 4 a.p.f.u. (Moëlo et al., 2008). Table IV also indicates the analyzed tetrahedrites are rich in Fe and Sb with minimal amounts of As. Freibergite displays similar trends with respect to Sb/As ratio, but has higher Zn than Fe concentrations.

Table IV: SEM-EDX data for ore minerals from Emery mine

	S	Ag	Sb	Pb	Fe	Cu	Zn	Au	Mn	As
Blg	55.77	0	18.75	25.48						
Blg	56.19	0	18.39	25.42						
Blg	56.48	0	18.41	25.11						
Blg	55.33	0	18.13	24.94	0.50	0.79	0.31			
Blg	55.33	0.13	18.52	25.41	0.37	0.25	0			
gal	53.94	1.19	1.31	43.55						
gal	52.97	0	0.96	46.07						
gal	52.58	0	0.55	46.88						
gal	52.97	0.15		46.89						
gal	49.40	0		50.60						
Tet	42.86	12.12	13.30		4.90	24.29	2.53			
Tet	42.12	15.92	13.98		2.78	20.67	4.53			
Tet	42.30	10.14	13.47		4.91	26.52	2.67			
Tet	42.66	9.70	13.05		4.92	27.01	2.66			
Tet	42.10	9.88	13.02		5.16	26.96	2.88			
Sph	47.43				5.24		46.55		0.78	
Sph	48.92				2.75		48.31		0.02	
Sph	49.36				5.57		43.57			
el		39.10						60.90		
el2		38.42						61.58		
Aspy	36.25				33.47					30.29
Aspy	33.38				30.85	0.84	5.03			29.90
Mene	missing	32.25	61.71			5.94				
Bnn	missing		32.44	35.74		31.82				

Values in atomic %

Aspy = arsenopyrite, blg = boulangerite, bnn = bournonite, el = electrum, gal = galena, mene = meneghinite, tet = Ag-rich tetrahedrite, sph = sphalerite

Table V: EPMA data

Sample Name	Sn	Zn	Cd	Pb	Fe	Cu	S	As	Sb	Ag	Au	Bi	Total
tet	BDL	2.192	0.053	BDL	4.341	26.301	23.692	0.925	25.680	16.338	BDL	BDL	99.521
tet	0.053	2.198	0.069	BDL	4.371	26.434	23.676	1.204	25.242	16.204	BDL	BDL	99.450
tet	0.032	2.437	0.058	BDL	4.173	26.267	23.635	0.882	25.726	16.218	BDL	BDL	99.428
tet	0.051	2.427	0.035	BDL	4.187	26.618	23.807	0.981	25.431	15.951	BDL	BDL	99.488
fre	0.030	2.420	0.055	BDL	4.121	24.366	23.491	0.792	25.535	18.769	BDL	BDL	99.579
fre	0.034	2.559	0.063	BDL	4.012	24.316	23.486	0.832	25.402	18.836	BDL	BDL	99.539
Sph	BDL	58.548	0.400	BDL	6.633	0.032	33.548	BDL	BDL	BDL	BDL	BDL	99.160
Spl	BDL	58.705	0.405	BDL	6.472	0.025	32.875	BDL	BDL	BDL	BDL	BDL	98.483
Sph	BDL	58.812	0.416	0.067	6.528	BDL	33.537	BDL	BDL	BDL	BDL	BDL	99.359
Sph2	BDL	60.765	0.414	BDL	3.048	0.613	32.859	BDL	0.078	0.055	BDL	BDL	97.830
Sph3	0.167	59.027	0.336	BDL	5.189	0.190	33.300	BDL	BDL	BDL	BDL	BDL	98.209
Sph3	0.215	61.246	0.402	BDL	3.325	0.275	33.140	BDL	BDL	BDL	BDL	BDL	98.603
El	BDL	1.758	0.047	BDL	1.808	10.750	13.155	0.358	10.438	19.358	37.476	BDL	95.148
El	BDL	3.907	BDL	BDL	0.275	1.095	BDL	BDL	0.063	29.637	74.349	BDL	109.326
El2	BDL	1.020	BDL	BDL	0.049	0.467	BDL	BDL	BDL	29.439	71.834	BDL	102.809
El2	BDL	1.272	BDL	BDL	0.067	0.870	BDL	BDL	BDL	29.651	70.289	0.135	102.283
aspy	BDL	0.179	BDL	0.044	35.940	BDL	22.879	41.860	BDL	BDL	0.069	BDL	100.971
aspy	BDL	0.166	BDL	BDL	35.902	BDL	22.724	42.032	BDL	BDL	BDL	BDL	100.825
aspy	BDL	0.171	BDL	BDL	35.716	BDL	22.376	42.560	0.073	BDL	BDL	BDL	100.895
Aspy2	BDL	0.188	0.023	BDL	36.013	BDL	22.418	42.409	BDL	BDL	BDL	BDL	101.051
Aspy2	BDL	0.177	BDL	BDL	35.578	0.017	22.279	42.932	BDL	BDL	BDL	BDL	100.983
blg	0.107	BDL	BDL	54.101	0.141	0.102	18.786	0.911	24.267	BDL	BDL	BDL	98.415
blg	0.117	BDL	BDL	54.602	0.130	0.046	18.582	0.704	24.761	BDL	BDL	0.056	98.997
blg	0.071	BDL	BDL	55.940	0.199	0.083	18.473	0.691	24.243	BDL	BDL	BDL	99.700
blg	0.122	BDL	BDL	55.447	0.146	0.077	18.833	0.634	24.756	BDL	BDL	BDL	100.015

All data in wt%

aspy = arsenopyrite, blg = boulangerite, el = electrum, fre = freibergite, tet = Ag-rich tetrahedrite, sph = sphalerite

Boulangerite ($(Pb_{.98}Fe_{.01}Cu_{.01})_5(Sb_{.96}As_{.04})_4S_{11}$) is nearly as plentiful as arsenopyrite. It occurs as elongated prisms with blunted tips and irregular masses filling space between quartz and arsenopyrite (Figure 7A, 7C, and 7D). Figures 9A, 9B, and 9D show boulangerite replacing Stage 1 minerals (quartz, arsenopyrite, pyrite) as well as intergrown with other Pb-bearing minerals (galena). Notice the dissolution of earlier euhedral quartz in Figures 9A and 9D as well as Figure 9A. Figure 7A shows boulangerite (white) needles included in sphalerite (dark gray) with some chalcopyrite. Note the euhedral quartz grain in the sphalerite. Table IV indicates the boulangerite is nearly pure with very little Fe and As with minor amounts of Cu.

Two grains of electrum 40 μm and 20 μm in diameter were found with X_{Au} of 0.579 and 0.565, from EPMA (Table V). The electrum was found included in Ag-rich tetrahedrite. Figure 7B and 7C are EPMA images of the electrum. Table V shows the analyses from the EPMA, note the total column for the electrum grains. Due to the size of the grains and drift of the instrument the results may be slightly skewed but the computed Au:Ag ratios are considered valid. Only the first analysis was discarded due to low X_{Au} and noted excess drift.

During SEM-EDX analysis additional minerals such as meneghinite and bournonite were found. Figure 8B shows the intergrowth of these minerals. Galena was replaced by bournonite ($PbCuSbS_3$) with patches of meneghinite ($CuPb_{13}Sb_7S_{24}$) at the interface between galena and bournonite. The meneghinite grain was analyzed twice by SEM-EDX. However, in the first scan Cu was left off the element list while in the second attempt S was inadvertently left off the list. Figure 8 shows the SEM-EDX spectrum of this phase: the small Cu peak compared to the larger Pb and Sb peaks indicates meneghinite is likely the proper identification. The meneghinite in Figure 8B occurs between bournonite and galena, and this texture is consistent with the bulk composition of meneghinite, which is intermediate between bournonite and galena.

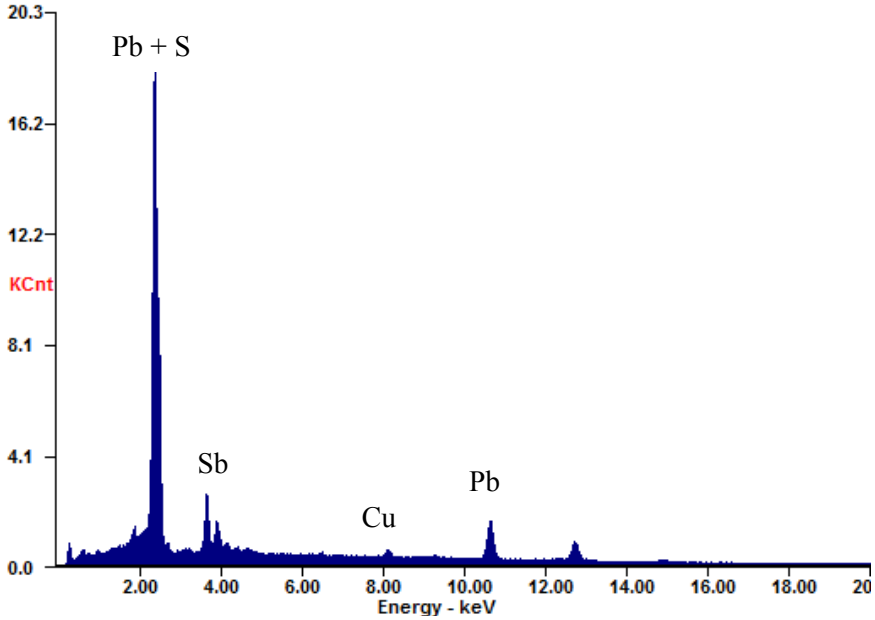

Figure 8: SEM-EDX spectrum for meneghinite

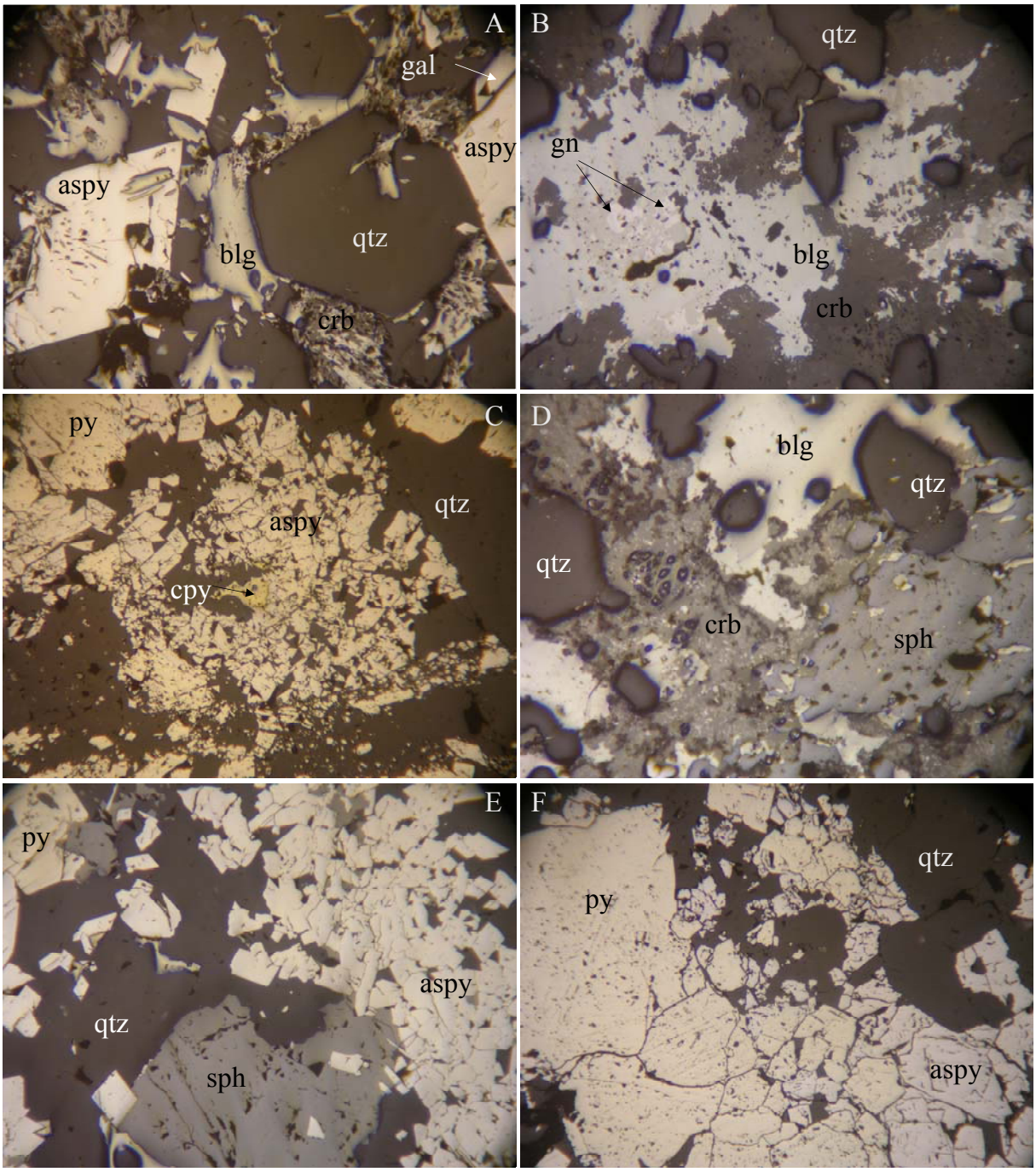

Figure 9: Reflected light photomicrographs. A) Euhedral arsenopyrite (aspy) and quartz (qtz) are replaced by later boulangerite (blg) and galena (gal) which is replaced by carbonate. Stage 2 minerals infill the open space between the Stage 1 minerals. B) Small patches of gn included in blg replaced by carbonate. Euhedral qtz indicates some open-space filling occurred. C) Pyrite (py) and aspy intergrown as euhedral to subhedral crystals with a grain of anhedral chalcopyrite (cpy). D) Blg next to and included in sphalerite (sph). Euhedral qtz show dissolution when included by blg. Blg is preferentially replaced by crb while sph only shows slight dissolution. E) Massive aspy with py and sph in qtz gangue. Note aspy shows little dissolution when included in sph. F) Py and aspy intergrown in qtz. Field of view in each panel is 2mm.

3.3. Gangue Minerals

Quartz was deposited throughout the entire evolution of the system. When in amygdules, quartz is found as concentric or colloform layers of chalcedony, occasionally filling the entire amygdule. Chalcedony-filled amygdules display a mosaic texture under XPL. Mosaic texture is thought to represent insipient crystallization of what was initially an amorphous silica gel (Dong et al., 1995). When in a vein, quartz is found as comb, massive, and zoned structures. Zoned quartz has alternating zones of clear and milky quartz within individual crystals. Massive varieties vary from milky to clear-gray. Milky quartz has a high number of fluid inclusions too small to analyze while clear-gray quartz tends to have fewer fluid inclusions that are larger and more easily analyzed. Even though quartz is present in every stage of paragenesis it can be delineated by sulfide assemblages and fluid inclusion populations. The earliest quartz has type 2 thru 4a fluid inclusions (see Figure 15) while Stage 1 quartz (see paragenesis Figure 5) can be associated with arsenopyrite and pyrite and Stage 2 quartz is associated with Pb-sulfide/sulfosalts. The latest quartz has fluid inclusions with low Th values (below 180°C) and a greater ratio of carbonate to quartz in the veins.

Ankerite is found intergrown with vein material as well as patches in carbonate replacement. Textural and isotopic evidence suggests ankerite was deposited throughout the sulfide stages. Dolomite (SEM-EDX analyses in Table VI) was deposited from the end of Stage 1 and through to the closing stages of mineralization and is often “peppered” with fine grained sulfides. The dolomite, under XPL, in carbonate breccia appears to be “saddle dolomite” with undulatory extinction. Table VI displays the composition of dolomite as determined by SEM-EDX. Calcite was one of the last hypogene minerals to be deposited. It can be found as matrix material in the carbonate breccia as well as in late-stage cross-cutting carbonate veins. Calcite is also found quite commonly in volcanlabradoriteic amygdules when precipitation would most

likely precede mineralization. Kutnohorite was deposited during the early carbonate stage and possibly into Stage 1. It is found in carbonate-rich veinlets running next to sulfide bearing veins and is a deeper shade of pink than ankerite. Cerussite is a weathering product of galena with occasional boulangerite replacement. Figure 9A shows the preferential weathering. The galena still shows triangular pitting and extensive replacement while the pyrite and arsenopyrite only display minor replacement.

Table VI: SEM-EDX analysis of carbonates

		OK	*MgK*	*CaK*	*MnK*	*FeK*	
Dolomite	***Wt%***	40.07	16.24	34.5	2.03	7.16	$CaMg_{.40}Fe_{.15}Mn_{.04}(CO_3)_2$
	At%	59.66	15.91	20.5	0.88	3.05	
Dolomite	***Wt%***	38.59	15.22	35.64	4.43		$CaMg_{.89}Mn_{.11}(CO_3)_2$
	At%	58.58	15.2	21.6	1.96		

3.4. Alteration Styles

Due to extensive alteration of the bedrock in the district, unaltered samples had to be collected from the same volcanic flow just to the south. The least altered samples were collected by K. Scarberry during mapping of the Sugarloaf Mountain quadrangle. K. Scarberry (2015, 2016) was able to delineate the various volcanic deposits through trace element analysis. These samples (KCS-13-22 and KCS-13-24) contain relatively unaltered plagioclase. Compositions determined by the Michel-Lévy method fall between labradorite and bytownite, the same compositions as found by previous workers (Stejer, 1948; Joyce, 1951; Robertson, 1953). Pyroxene in the samples has been altered, but previous workers describe it as augite (Stejer, 1948; Joyce, 1951; Roberston, 1953).

3.4.1. Silicic

Silicic alteration occurs as replacement of the wall rock by microcrystalline silica or quartz. Figure 10B shows extensive silicic alteration of the wall rock fragment with some higher

birefringent minerals preserved in the clast. If the alteration is strong the wall rock can be completely replaced leaving a gray groundmass with amygdules and pyrite throughout. In thin section ghosts of plagioclase can be found. According to Stejer (1948) silicic alteration occurs closest to the veins before grading into sericitic alteration. The TerraSpec Halo was not able to aid in delineating this stage of alteration due to the lack of phyllosilicate minerals.

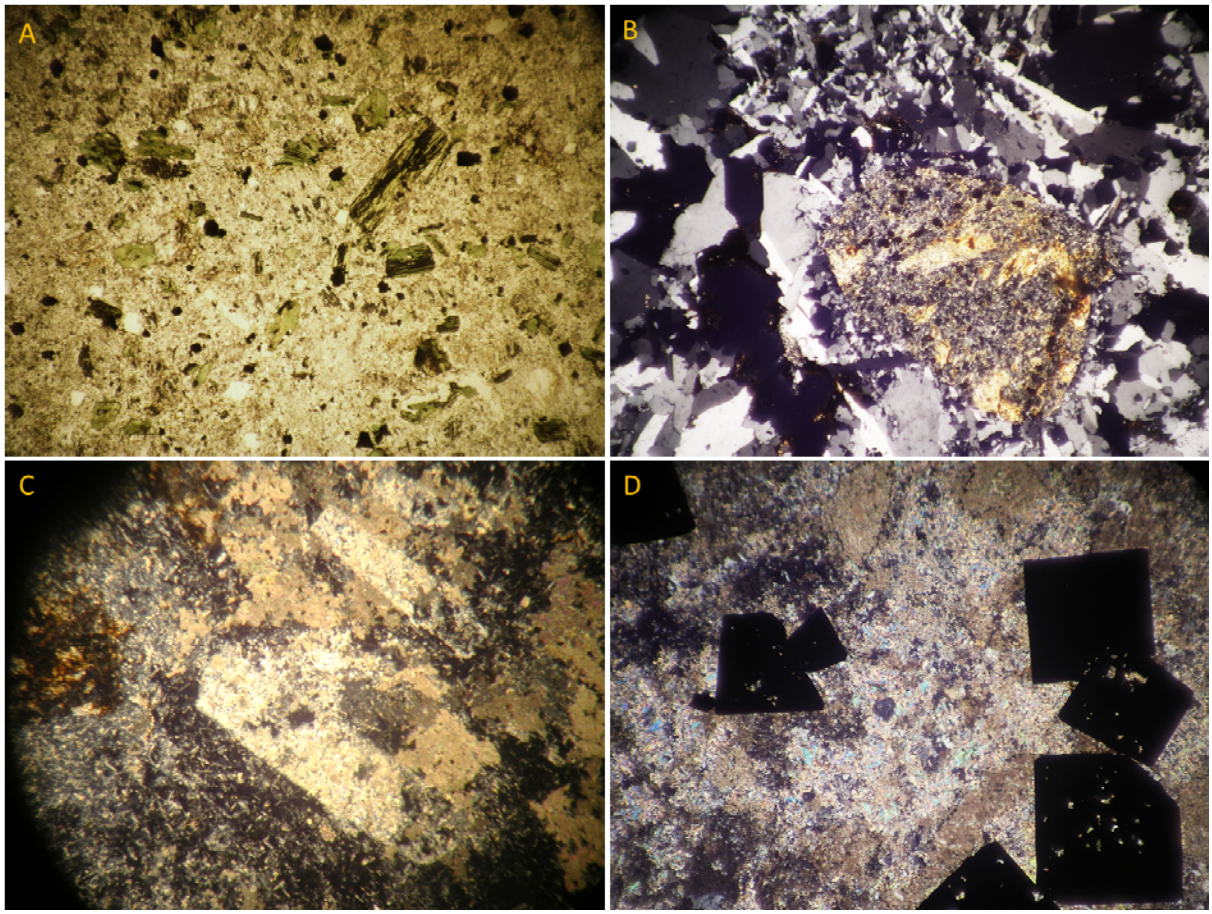

Figure 10: Alteration styles in thin section. A) Propylitic alteration in PPL. Plagioclase altered to chlorite with fine quartz in the matrix. B) Silicic alteration with some sericite still present in the clast. Image in XPL. C) Carbonate alteration of the groundmass and plagioclase. Image in XPL. D) Sericitic alteration with minor carbonate. Groundmass is altered to fine grained sericite and quartz. Fe-bearing minerals are altered to pyrite. Image in XPL. All images captured under 40X.

3.4.2. Sericitic

Based on TerraSpec Halo and thin section analysis the sericitic alteration assemblage contains muscovite, phengite ($K(Al,Mg)_2(OH)_2(Si,Al)_4O_{10}$), pyrophyllite ($Al_2Si_4O_{10}(OH)_2$), K-

illite, quartz, and pyrite. TerraSpec analysis indicates that sericitic alteration can be identified by low ISM (Illite Spectural Maturity) scalar values (0.612 to 0.873). The low ISM scalars indicate a higher temperature of crystallization (Shankar, 2015). Although pyrophyllite is normally associated with advanced argillic alteration it is included here because only one scan registered pyrophyllite and it is therefore assumed to be uncommon. In thin section (Figure 10D) sericitic alteration is noticeable by the high birefringence of muscovite. The groundmass is replaced by fine-grained quartz and muscovite while the pyroxene and plagioclase have been converted to muscovite and K-illite with the excess Fe incorporated into subhedral to euhedral pyrite cubes and pyritohedra. Sericitic alteration is found as an envelope around the vein and silicic alteration.

In hand sample, the typical sericitically altered rock has a light color with many mica surfaces reflecting light. Ideal samples are buff or cream colored and are quite hard due to the quartz content.

3.4.3. Propylitic

Most of the rocks distal to mineralized veins in the Emery district are propylitically altered. TerraSpec analysis indicates the mineral assemblage to be epidote, clinozoisite/zoisite, Fe-Mg chlorite, Mg-illite, calcite, siderite, kaolinite, and pyrite. TerraSpec ISM scalar values range from 0.913 to 1.298 for propylitically altered samples. These higher ISM values indicate a lower temperature of formation. Kaolinite WX (well crystallized) can also be found in the assemblage.

Unlike some of the more intense alteration styles, original crystal shapes are still well preserved in propylitic alteration from phenocrysts down to small plagioclase laths in the groundmass. Plagioclase has been altered to Mg-illite, calcite, quartz. Pyroxenes may still retain

original textures (crystal shape, fractures) but are replaced by Fe-Mg chlorite, epidote, clinozoisite/zoisite, and pyrite (Figure 10A).

In hand sample the appearance of propylitically altered rock ranges from an unaltered black to various shades of green-black to pistachio green. Figure 11 shows the various intensity of propylitic alteration. Figure 11A (Em-38) displays the typical pistachio green color of epidote for the majority of the groundmass. Some amygdules are replaced by Fe-Mg chlorite and carbonate material. Figure 11B (Em-23) is a darker green color with replaced plagioclase visible. Fe-Mg chlorite and hydrobiotite appear to be the main constituents of the groundmass while the plagioclase appears to have been altered to Mg-illite. Figure 11C is a black-green color on a cut surface when wet. Most of the groundmass is biotite and hornblende. The plagioclase and pyroxene have been altered and replaced by pyrite and chlorite. Figure 11D (P-7) is weathered but still exhibits propylitic assemblages. The groundmass is green with a tinge of limonite brown discoloration. Fe chlorite, vermiculite and ferrihydrite were found. Ferrihydrite and vermiculite are most likely recent weathering products of Fe-bearing minerals and biotite, respectively. Pyroxene phenocrysts have been altered to Fe chlorite. Any pyrite present has been weathered to ferrihydrite.

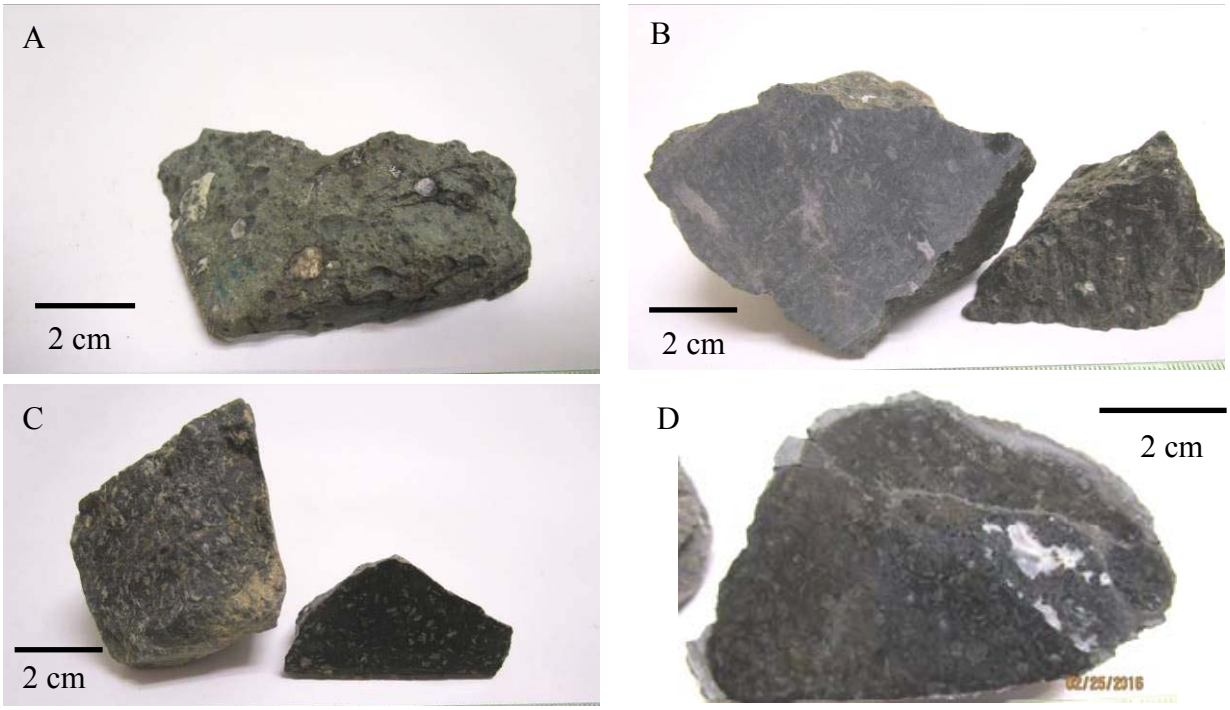

Figure 11: Propylitic alteration in hand sample. A) Em-38: Amygdaloidal basaltic andesite propylitically altered. Groundmass is pale green. Amygdules are dark green (chlorite) to white (filled with chalcedony/carbonate). B) Em-23 Amygdaloidal basaltic andesite with altered plagioclase. Mafic minerals in the groundmass altered to chlorite with reddish carbonate material. C) HHand 4: Porphyritic feldspar basaltic andesite. Plagioclase and pyroxene are altered. Matrix is black-green with disseminated pyrite. D) Em-30: Porphyritic feldspar-pyroxene basaltic andesite. Slightly propylitically altered, visible in pyroxenes. Area near amygdule high in carbonate.

3.4.4. Carbonate

In hand sample the weathered surface may appear reddish-brown (Figure 12C) or similar to the other alteration styles since carbonate alteration can be subtle. If the alteration is intense the rock may show carbonate crystals and when broken the coloration will be lighter than expected with patches of pink (Figure 12B). Less intense alteration is only visible under a microscope as irregular masses of carbonate minerals replacing groundmass, plagioclase, and pyroxene as in Figure 10C. When near carbonate breccias or carbonate-rich veins the volcanic rock can be replaced by carbonate minerals. It is seen most easily in carbonate breccias where clasts are replaced so heavily that there are occasional amygdules completely enclosed by

carbonate minerals (Figure 12D). Figure 12C and 12A are from the Argus and Paymaster mines and show extensive replacement of the wall rock by carbonate minerals (likely dolomite and ankerite). The banding present in Figure 12A shows the growth between the carbonates and sulfides. Above the pyrite vein the volcanic wall rock has been replaced by the carbonates.

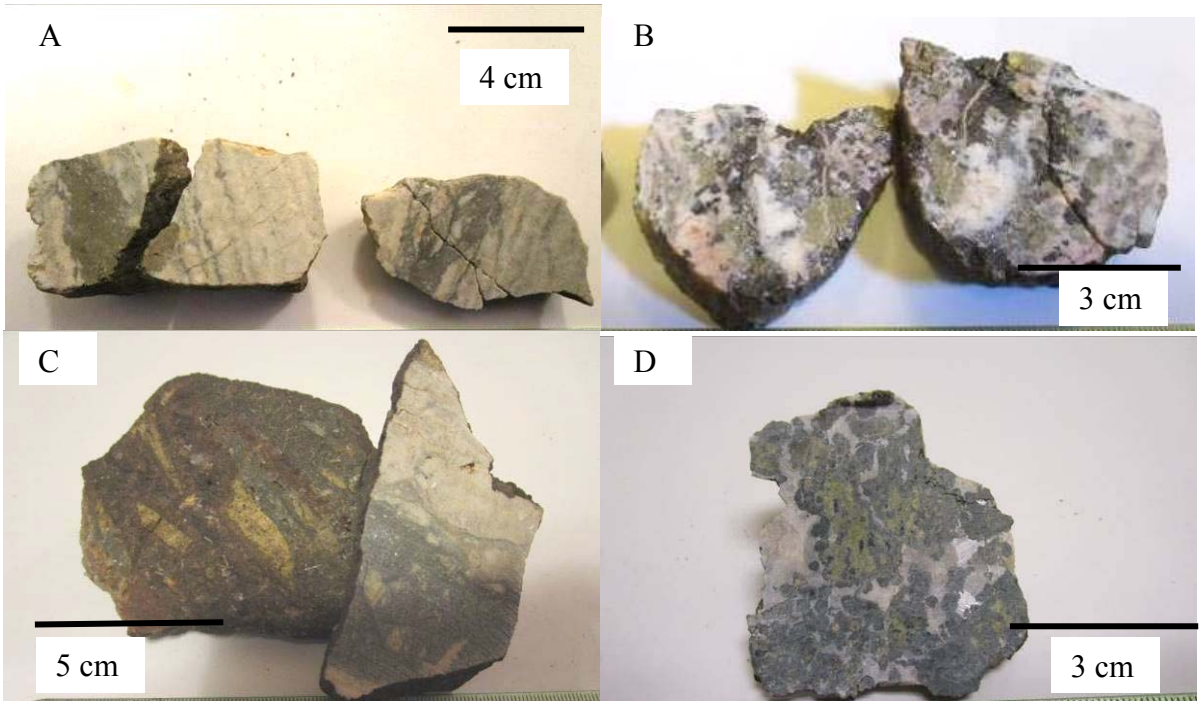

Figure 12: Carbonate alteration in hand sample. A) P-6: Banded quartz-carbonate with veinlet of pyrite and fine-grained sphalerite and galena. B) P-4: Pyrite with sphalerite and galena in a matrix of vein quartz with carbonate. Veinlets of carbonate cut sulfides. C) A-5: Carbonate breccia cemented by sulfides. D) Em-39: Carbonate breccia. Clasts altered by carbonate-rich fluids. Clasts formerly amygdaloidal basaltic andesite.

Based on TerraSpec Halo analysis, the carbonate breccia samples have a matrix of calcite with some palygorskite ($(Mg,Al)_5(Si,Al)_8O_{20}(OH)_2 \cdot 8H_2O$), an alteration product of Mg-silicates, and beidellite ($(Na,Ca_{0.5})_{0.3}Al_2((Si,Al)_4O_{10})(OH)_2 \cdot nH_2O$), an Al-rich variety of montmorillonite. These minerals were found along the rims of breccia clasts and may represent the alteration of Mg-illite and chlorite. Due to the nature of carbonate alteration (lack of white micas) no ISM scalar values could be obtained for this assemblage.

3.4.5. Argillic

The argillic alteration assemblage contains K-illite, montmorillonite, sepiolite and quartz. Coloration in hand sample is buff to cream. Argillic alteration samples also contain ferrihydrite which may be a product of recent weathering. The groundmass is extensively replaced by intergrowths of K-illite and quartz with patches of carbonate, dolomite and ankerite. The abundance of carbonates suggests that argillic and carbonate alteration overlap in time and space. Goethite and ferrihydrite are common where pyrite and Fe-bearing minerals were weathered/replaced. Argillic alteration was found in nearly all of the samples analyzed by the TerraSpec. ISM scalar values range from 0.742 to 1.048. Note that argillic ISM values are intermediate between those of sericitic and propylitic alteration.

3.4.6. Summary of TerraSpec Results

Table VII indicates the averages and ranges for the various TerraSpec Halo scalars according to the alteration style. Sericitic alteration has a distinct low ISM average (below 1) while propylitic alteration has high ISM values (above 1). Argillic alteration displays an ISM range that broadly overlaps with sericitic, propylitic, and carbonate alteration therefore another scalar should be used to delineate the alteration styles. Using the AlOH scalar average, propylitic alteration has the lowest value (2196), however, the range encompasses all of the alteration styles. The MgOH scalar averages show carbonate alteration with the lowest value (2340) grading through propylitic and argillic to sericitic with the highest value (2347.3). Figure 13 shows alteration minerals that can be identified by the TerraSpec Halo. This figure was based on the review paper by Corbet and Leach (1997). Figure 14 shows the alteration assemblage as indicated by the TerraSpec Halo. Note the cluster of data from the upper mesothermal range to deep epithermal conditions. The points at the top of the figure likely represent weathering.

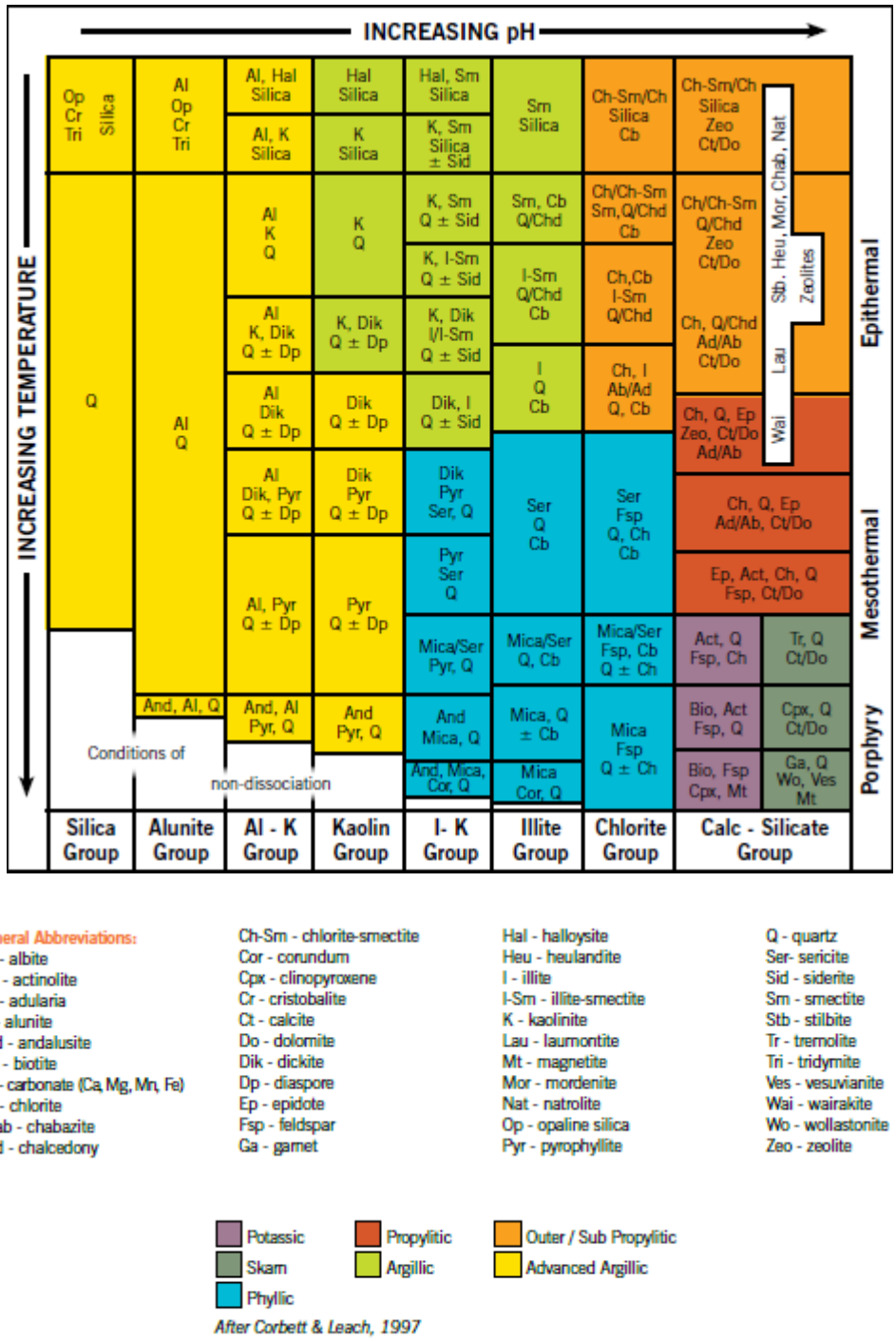

Mineral Abbreviations:

Ab - albite
Act - actinolite
Ad - adularia
Al - alunite
And - andalusite
Bio - biotite
Cb - carbonate (Ca, Mg, Mn, Fe)
Ch - chlorite
Chab - chabazite
Chd - chalcedony
Ch-Sm - chlorite-smectite
Cor - corundum
Cpx - clinopyroxene
Cr - cristobalite
Ct - calcite
Do - dolomite
Dik - dickite
Dp - diaspore
Ep - epidote
Fsp - feldspar
Ga - garnet
Hal - halloysite
Heu - heulandite
I - illite
I-Sm - illite-smectite
K - kaolinite
Lau - laumontite
Mt - magnetite
Mor - mordenite
Nat - natrolite
Op - opaline silica
Pyr - pyrophyllite
Q - quartz
Ser- sericite
Sid - siderite
Sm - smectite
Stb - stilbite
Tr - tremolite
Tri - tridymite
Ves - vesuvianite
Wai - wairakite
Wo - wollastonite
Zeo - zeolite

Potassic
Propylitic
Outer / Sub Propylitic
Skarn
Argillic
Advanced Argillic
Phyllic

After Corbett & Leach, 1997

Figure 13: Summary of common hydrothermal alteration minerals that can be identified using the TerraSpec Halo mineral analyzer. (ASD, 2016)

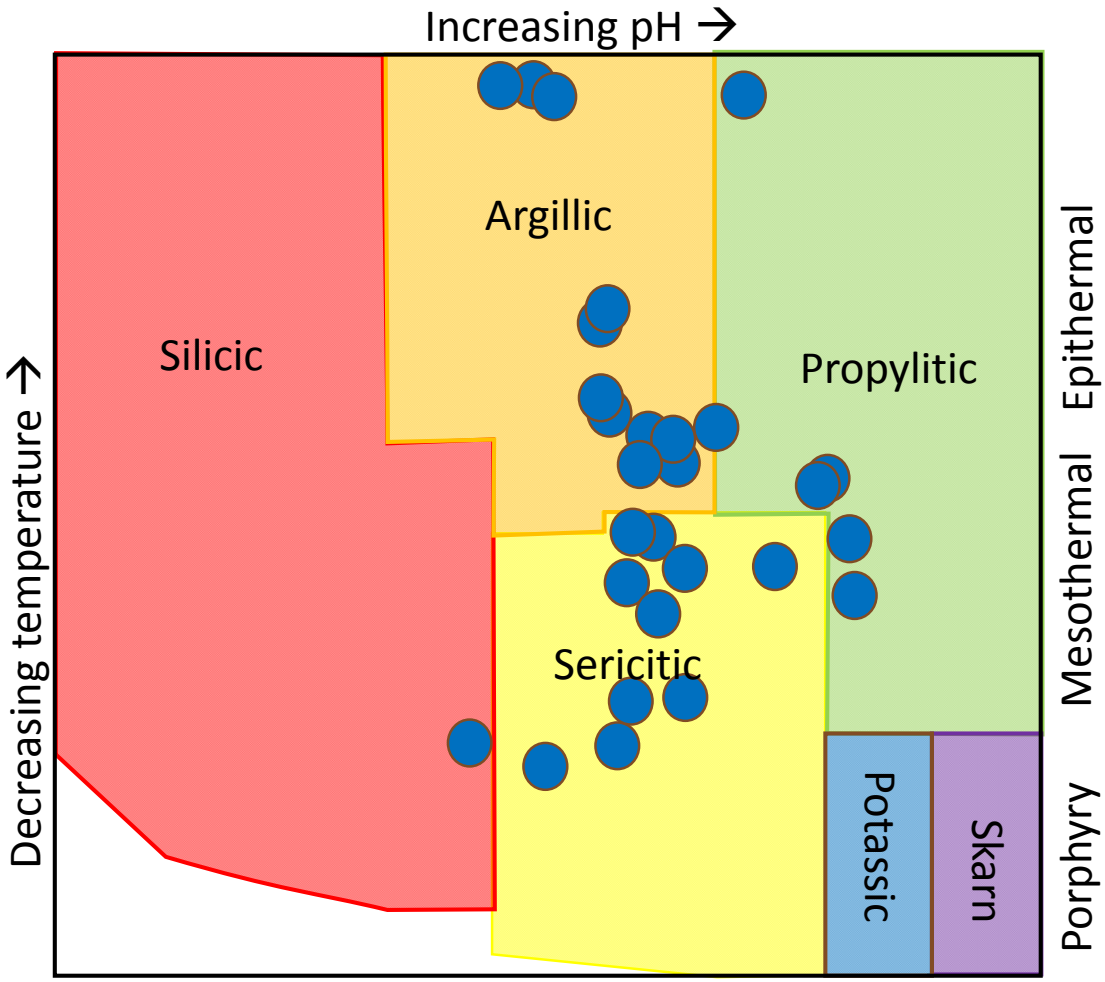

Figure 14: Alteration assemblage as indicated by the TerrraSpec Halo. Image modified after ASD (2016)

Table VII: Results of TerraSpec Halo analysis of different alteration styles

	Minerals	ISM (Average)	Range	Kx (Average)	Range	AlOH (Average)	Range	MgOH (Average)	Range
Carbonate	Dolomite, calcite, kutnohorite, ankerite	0.957	0.844-1.159	1.054	1.041-1.067	2206.8	2200.9-2213.3	2340	2333.3-2347.8
Silicic	Quartz, microcrystalline silica	---	---	---	---	---	---	---	---
Sericitic	Muscovite, phengite	0.756	0.624-0.994	---	---	2206.2	2203-2209	2347.3	2344.9-2348.7
Propylitic	Epidote/ clinozoisite, zoisite, chlorite, kaolinite	1.005	0.87-1.298	1.022	0.999-1.044	2196.8	2009.4-2215.1	2342.6	2330.8-2350.4
Argillic	Montmorillonite, K-illite	0.791	0.612-1.085	---	---	2202.7	2007.2-2209.5	2346.2	2333.3-2350.4

3.5. Fluid Inclusions

Samples for fluid inclusion analysis were collected from the Emery, Hidden Hand, Blue-eyed Maggie, Paymaster, Elizabeth, and Argus mine dumps. The analyzed inclusions were from low-angle veins (Raw data can be found in Table A-1). Fluid inclusions from steep veins, while abundant, were small, ragged and not conducive to analysis. Low-angle veins had larger inclusions as well as populations of primary inclusions. All fluid inclusions were hosted by quartz. Sphalerite was examined but inclusions found were too small for analysis or the chip was too brittle to withstand analysis.

A total of 162 inclusions were analyzed and separated into two distinct groups; aqueous and CO_2-rich (Table A-1). The presence of CO_2 was confirmed by laser microRaman. As can be seen from Figure 15, 4 types of inclusions were identified with subcategories to include the presence or absence of daughter minerals. Aqueous inclusions can be divided into type 1, 1a (halite daughter mineral), and 1b (dawsonite daughter mineral). Most of the aqueous inclusions were type 1 with few examples for type 1a and 1b. Type 1 are the simplest inclusions with a brine and vapor phase homogenizing to brine. Type 1a have a soluble daughter mineral, halite, and homogenize to the brine phase. Type 1b have an insoluble daughter (dawsonite) homogenize to the liquid phase. CO_2-rich inclusions can be divided into type 2, type 3, type 4, and type 4a. Type 2 inclusions had the highest amount of CO_2 based on volume and Th_{CO2} to CO_2 (l) and the Th to CO_2 (l). Type 3 inclusions show Th_{CO2} to CO_2 (l) and Th to brine. Type 4 inclusions show Th_{CO2} to CO_2 (v) and Th to brine. Type 4a inclusions show Th_{CO2} to CO_2 (v) and Th to brine but have insoluble daughter minerals such as dawsonite. The majority of CO_2-rich inclusions were type 4a or type 3 with an equal number of types 2 and 4. Inclusions listed as "no type" had insufficient data to classify.

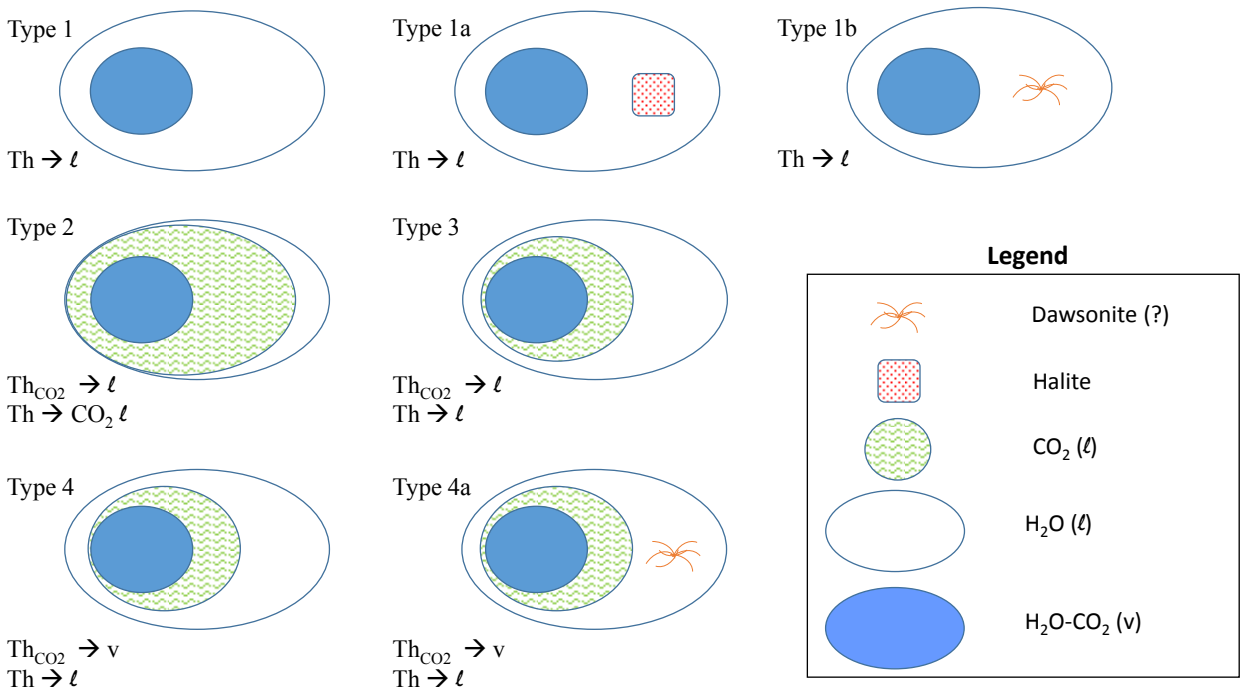

Figure 15: Fluid inclusion types. Type 1, 1a, 1b are all aqueous. Type 1a has a halite daughter mineral. Type 1b has a dawsonite daughter mineral. Types 2 through 4a are CO_2-rich inclusions. Type 4a may be the CO_2-rich equivalent of type 1b. Note the final Th phase for each inclusion as it further delineates the types.

Figure 16 shows the total breakdown of fluid inclusion Th data based on type. Figure 16A shows the total homogenization for inclusions while Figure 16B shows the homogenization of the carbonic phase. In Figure 16A, three peaks are visible around 190, 280, and 310 °C. These peaks represent the temperatures from the early carbonate stage through the late carbonate stage. The black boxes on Figure 16A indicate the temperature ranges for Stages 1 and 2. Notice the overlap around 280 °C. The overlap is present because Stage 1 temperatures (280 to 340 °C) appear to follow a fairly regular bell-shaped distribution as well as Stage 2 (220 to 280°C) except for the peak at 280 °C. The lower temperature range (120 to 210 °C) appears to indicate the late carbonate stage. Figure 16B shows the range in Th_{CO2} separated by type. The range is 18 to 30 °C with the biggest peak at 28 °C. Type 2 appears to be centered around 28 °C while type 3 bookends the data set and type 4a has a range from 24 to 28 °C. The data could be

misleading due to the smaller sample size and decrepitation that commonly occurs due to higher pressures needed for coexisting liquid and vapor CO_2.

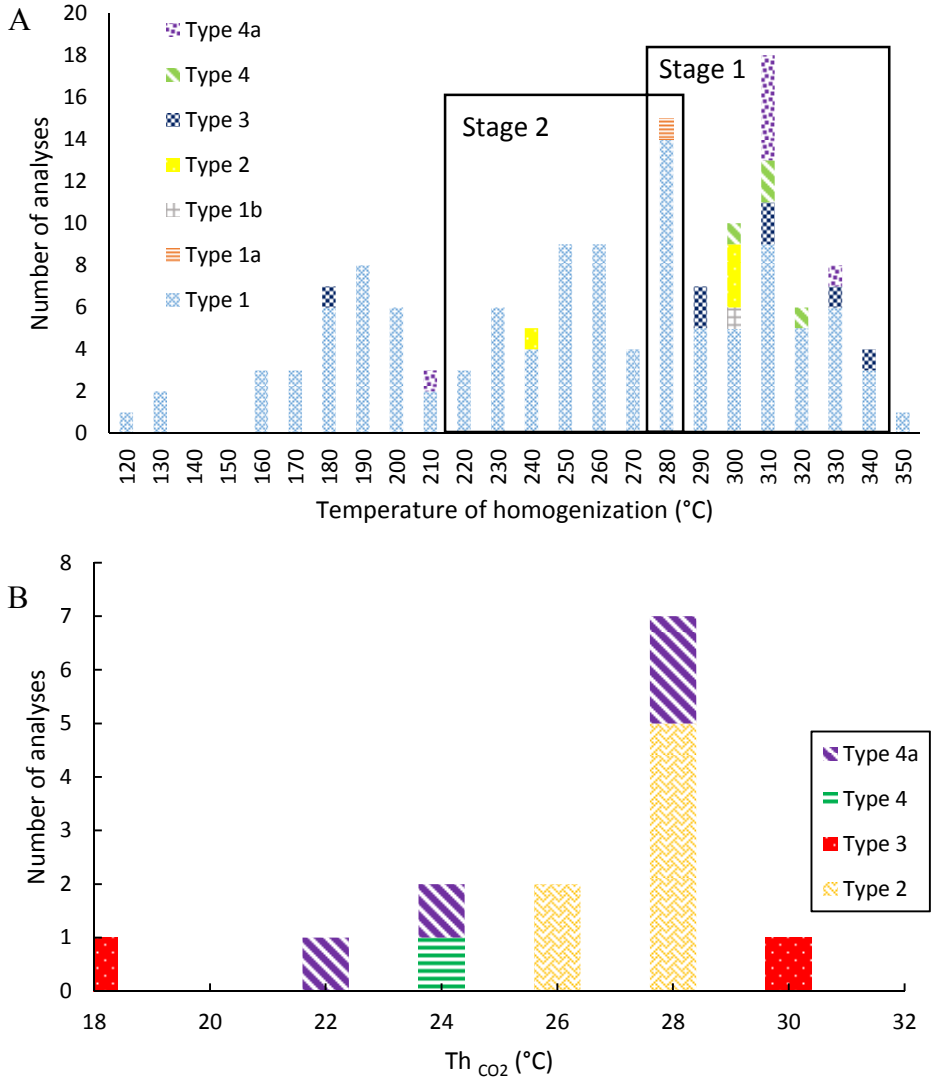

Figure 16: Histograms based on temperature of homogenization and temperature of homogenization of the carbonic phase. A) Temperature of total homogenization for both aqueous and CO_2-rich inclusions. The black boxes represent the estimated temperature ranges for Stage 1 and 2. The unboxed portion of the data represents the late carbonate stage. B) Temperature of homogenization for CO_2-rich inclusions.

Two salinity equations were used due to some inclusions having Tm_{ice} and others with Tm_{clath}.

$$Ws = 0.00 + 1.76958 * T - 4.2384*10^{-2} * T^2 + 5.2778*10^{-4} * T^3 \ (\pm 0.028) \quad (1)$$

In Equation 1 Ws is salinity in wt% $NaCl_{eq}$, T is the absolute value of Tm_{ice}, and has an accuracy of ± 0.028 wt% $NaCl_{eq}$. The equation is from Roedder, 1984.

$$W = +0.00098241(10 - T) * (T^2 + 45.385T + 1588.75) \ (\pm 1\%) \quad (2)$$

In Equation 2 W is salinity in wt% $NaCl_{eq}$ and T is Tm_{clath}. For the equation to be true Tm_{clath} must be between -10 °C and +10 °C and clathrate melting must occur in the presence of CO_2 liquid and vapor as well as brine. Error is slightly greater in this equation (± 1%). The equation is from Darling, 1991.

Salinity from Equation 1 is shown in Figure 17A and salinity from Equation 2 is shown in Figure 17B. Aqueous salinity (Figure 17A) is mainly concentrated between 4.5 and 8.5 wt% $NaCl_{eq}$ with outliers at 0, 0.5, and 10.5 wt% $NaCl_{eq}$. CO_2-rich inclusions were included in the histogram if Tm_{ice} was noted. It should be noted that salinity from such an inclusion may not show the true salinity due to the non-stoichiometric structure of clathrate, meaning, differing amounts of solutes and water can be trapped by the clathrate yielding a variable salinity. Figure 17B shows salinity from clathrate melting. The majority of the CO_2-rich analyses had a negative salinity possibly due to the presence of an unusual solute. Analyses with negative salinities had a Tm_{clath} above +10 °C. The measurements of Tm_{clath} were done carefully and shall have yielded reliable data. Perhaps Raman spectroscopy of the carbonic phase will show the presence of CH_4. CO_2-rich inclusions with positive salinity are clustered around 0 to 1.5 and 9 to 12 wt% $NaCl_{eq}$ with outliers at 4 and 14 wt% $NaCl_{eq}$. There does not appear to be a correlation between fluid

inclusion type and salinity. It is interesting to note that aqueous fluid inclusion salinities fall in the gap between the CO2-rich fluid inclusion salinities, however, it may just be a coincidence.

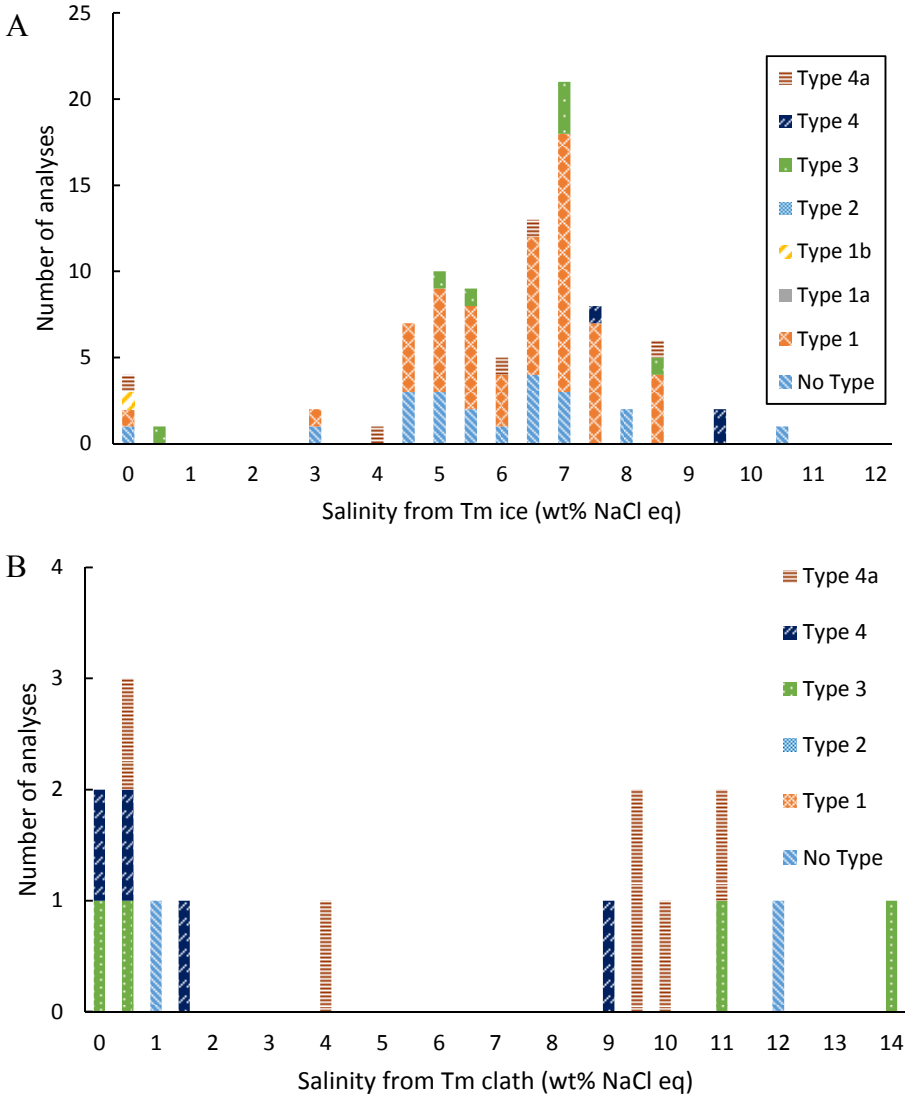

Figure 17: Histograms of salinity with values from Tm_{ice} and Tm_{clath}. A) Aqueous fluid salinity values calculated from Equation 3. The data is clustered between 4.5 and 8.5 wt% $NaCl_{eq}$. B) Salinity calculated from Equation 4 using Tm_{clath}.

Salinity ranges from 0 to 11.2 wt% $NaCl_{eq}$ over a Th range of 127.4 to 353.7 °C. As shown in Figure 18, type 1 inclusions form a band between 4 and 8 wt% $NaCl_{eq}$ (average 6.4 ± 1.4 wt% $NaCl_{eq}$). The type 1 outlier is visually similar to other type 1 inclusions and its vapor phase comprised 40% of the inclusion. The amount of vapor is on the high end of the trend but

not unusual. Salinity from Tm_{clath} in CO_2-rich inclusions range from 0 to 12.8 wt% $NaCl_{eq}$ and are clustered around Th of 310 °C with outliers at 209 °C and 245 °C. There is an anomalously high salinity type 3 at 14.2 wt% $NaCl_{eq}$. The inclusion has a small CO_2(l) (5%) bubble. It should be noted that salinity from Tm_{ice} was 8.8 wt% $NaCl_{eq}$ and Tm_{clath} salinity was 14.2 wt% $NaCl_{eq}$. The discrepancy has not been accounted for.

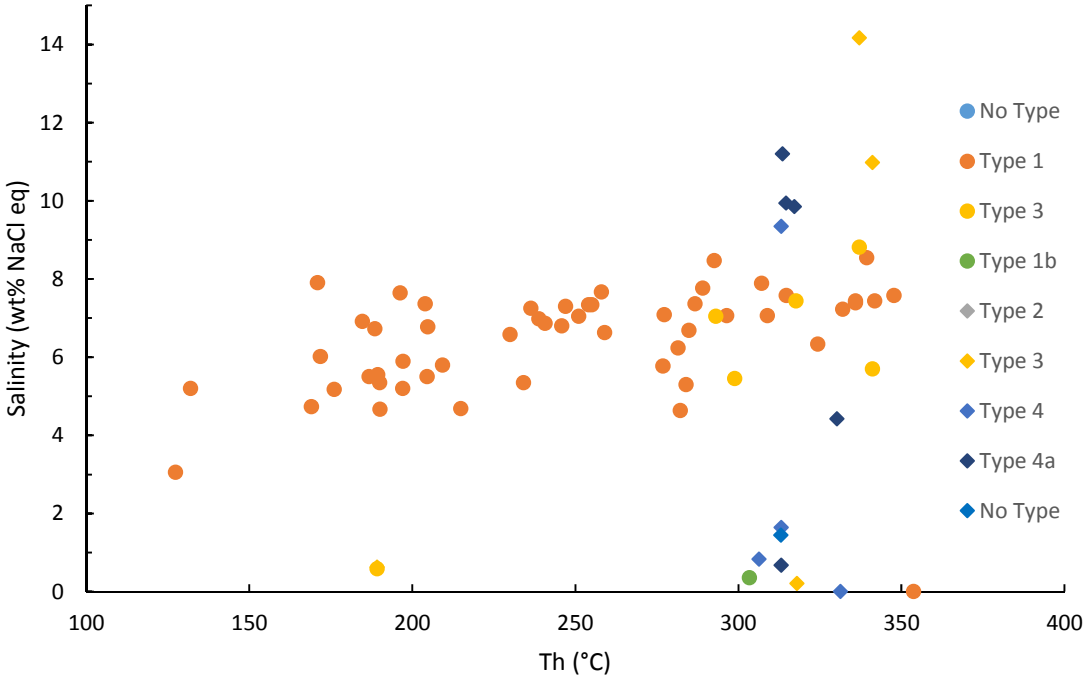

Figure 18: Salinity vs. total homogenization temperature. Circles are salinity from Tm_{ice}. Diamonds are salinity from Tm_{clath}.

It is possible that the "negative salinity" values are due to the presence of mixed CO_2-CH_4 clathrates. Using the computer programs of Bakker (1997), it would be possible to determine correct salinities based on clathrate melting temperatures in the presence of CH_4, but this would require analysis of the CO_2/CH_4 ratio in each fluid inclusion, which was outside the scope of this study. In this thesis, salinities from carbonic inclusions based on Tm_{clath} should be taken as minimum estimates of the true fluid salinity.

Density of aqueous inclusions, using Equation 3 for salinity, is shown in Figure 19. The density contours correspond to the density (in g/cm^3) of a vapor-saturated system. Contours were generated from equation-of-state using the Flincor computer system (Wilkinson, 2001). When density contours are overlain on the salinity chart, there appears to be increasing density with decreasing temperature and a small decrease with decreasing salinity.

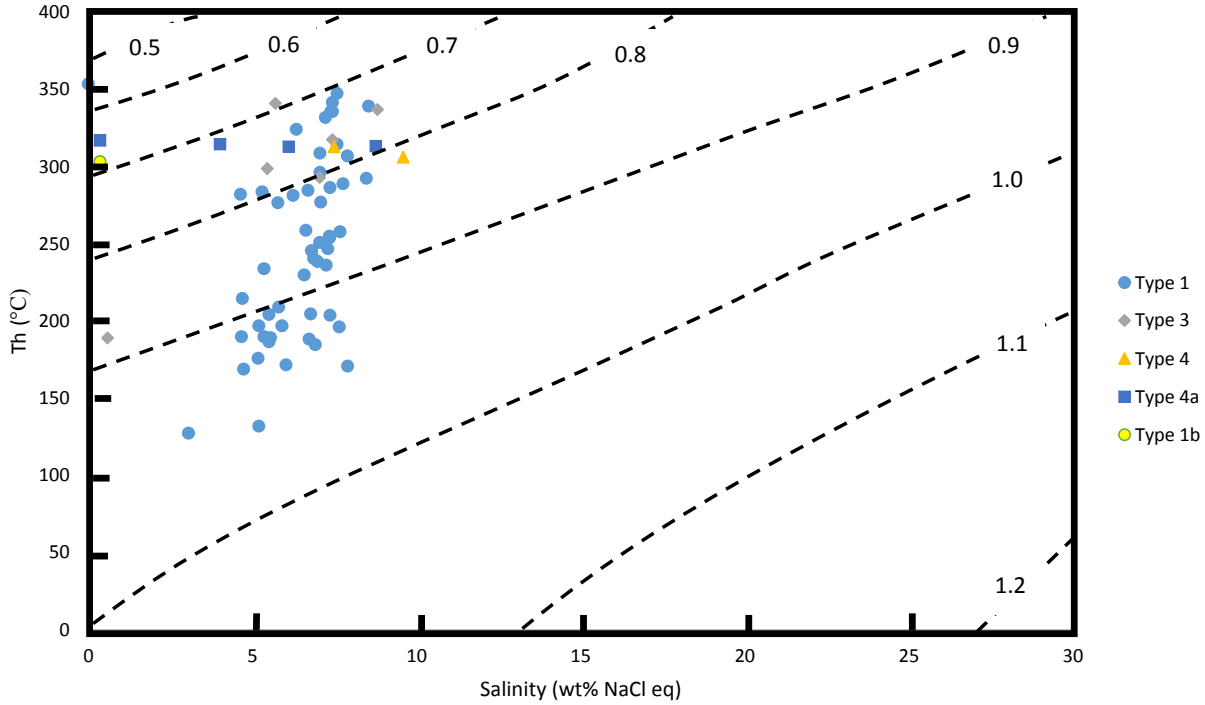

Figure 19: Fluid inclusion homogenization temperature vs. salinity for aqueous fluid inclusions. The dashed lines are contours of bulk density in g/cm^3. Adapted from Wilkinson, 2001.

Typical vapor phase volume estimations are presented in Figure 20. Overall vapor volume falls between 10 and 50 % with outliers at 0 and 70 %. The smallest vapor estimation was 5 %. This inclusion also had a dawsonite daughter mineral. Type 1 inclusions were constrained between 10 and 50 % with outliers at 70 %. Type 2 inclusions had vapor volumes from 10 to 30 %. Types 3 through 4a were focused between 10 and 40 %. "No type" inclusions form a flat bell curve from 10 to 50 % centered around 30 %.

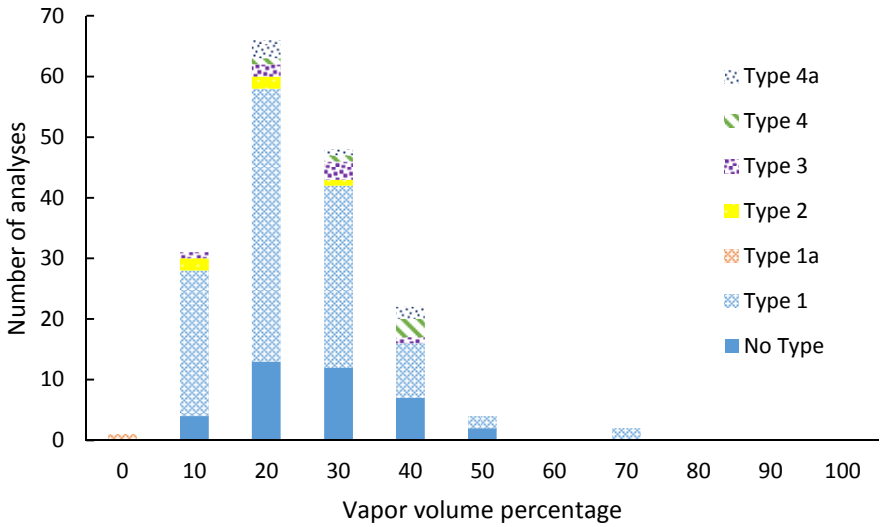

Figure 20: Histogram of vapor volume estimation. Volume was estimated by visual comparison to estimation charts from Roedder, 1984.

Table VIII shows volume estimations of liquid CO_2 and coexisting vapor phase. The first column displays the estimated volume of liquid CO_2 and the second displays the estimated vapor volume. "No type" inclusions are missing a Th indicator (Th_{CO2} or Th). Type 2 inclusions have the highest percentage of liquid CO_2 (40 to 80%) and vapor volumes from 10 to 30%. The only type 3 inclusion noted had roughly equal proportions of liquid CO_2 (30%) and vapor (20%). Types 4 and 4a display similar trends in both liquid CO_2 and vapor volumes. Liquid CO_2 volume estimations range from 5 to 40% and vapor volume estimations range from 20 to 40% for both types 4 and 4a. When the percent of CO_2 (l) was greater, the percent vapor was lower.

Table VIII: Volume percentages of CO_2 (l) and vapor in carbonic inclusions

"No Type"		Type 2		Type 3		Type 4		Type 4a	
CO_2 (l)	vapor	CO_2 (l)	vapor	CO_2 (l)	vapor	CO_2 (l)	vapor	CO_2 (l)	vapor
60	10	70	10	30	20	5	20	40	20
60	20	40	10			40	30	5	20
70	20	50	20			10	40	10	20
60	20	80	20			10	40	5	30
40	20	80	30				40	10	40
10	20							10	40
80	20								
80	20								
80	30								
60	30								
60	30								

While examining a population of type 2 inclusions, several type 1 were found as well. Th for the type 2 inclusions in the chip (Hidden Hand) ranged from 245 to 302 °C and the Th for type 1 ranged from 245 to 247 °C. There is a possibility that the correlation between the Th for type 1 and type 2 is an indicator of effervescence of the CO_2 phase around 245 to 247 °C.

Table IX shows the data from the Hidden Hand fluid inclusion assemblage. Overall there is not a wide distribution in the data. Tm_{CO2} ranged from -56.4 to -58.7°C. Tm_{ice} was recorded from two aqueous inclusions. Salinity from Tm_{ice} ranged from 6.7 to 7.3 wt% $NaCl_{eq}$. Tm_{clath} exceeded the upper range for acceptable values (averaging 11 °C) giving negative salinity calculations (most likely due to the presence of mixed CO_2-CH_4 clathrates). Th_{CO2} ranged from 27.1 to 29.4°C. No daughter minerals were found in the fluid inclusion population.

Figure 21 shows the population with Th for analyzed inclusions. Numbers 8 and 11 are the coexisting aqueous (type 1) inclusions with type 2 comprising the CO_2-rich inclusions.

Table IX: Hidden Hand fluid inclusion population data

Hidden Hand	Type	Tm_{CO2}	Tm_{ice}		Tm_{clath}	Th_{CO2} ($\rightarrow$ l)			Th	Td
1	2	-56.4			11.2	27.5	27.4		245	
2					10.9	29.8				
3	2				10.3	28.4				283.8
4	2	-56.4			10.9	28.2	27.9	28.2	301.9	
5					11	29.4				
6	2	-58.7			11.2	28.2			301.9	
7	2				11.2	28.2	28.3		301.9	
8	1		-4.3	-4.2					245.8	
9					11.2	27.8	27.7			
10					11.2	27.1				
11	1		-4.6						247	

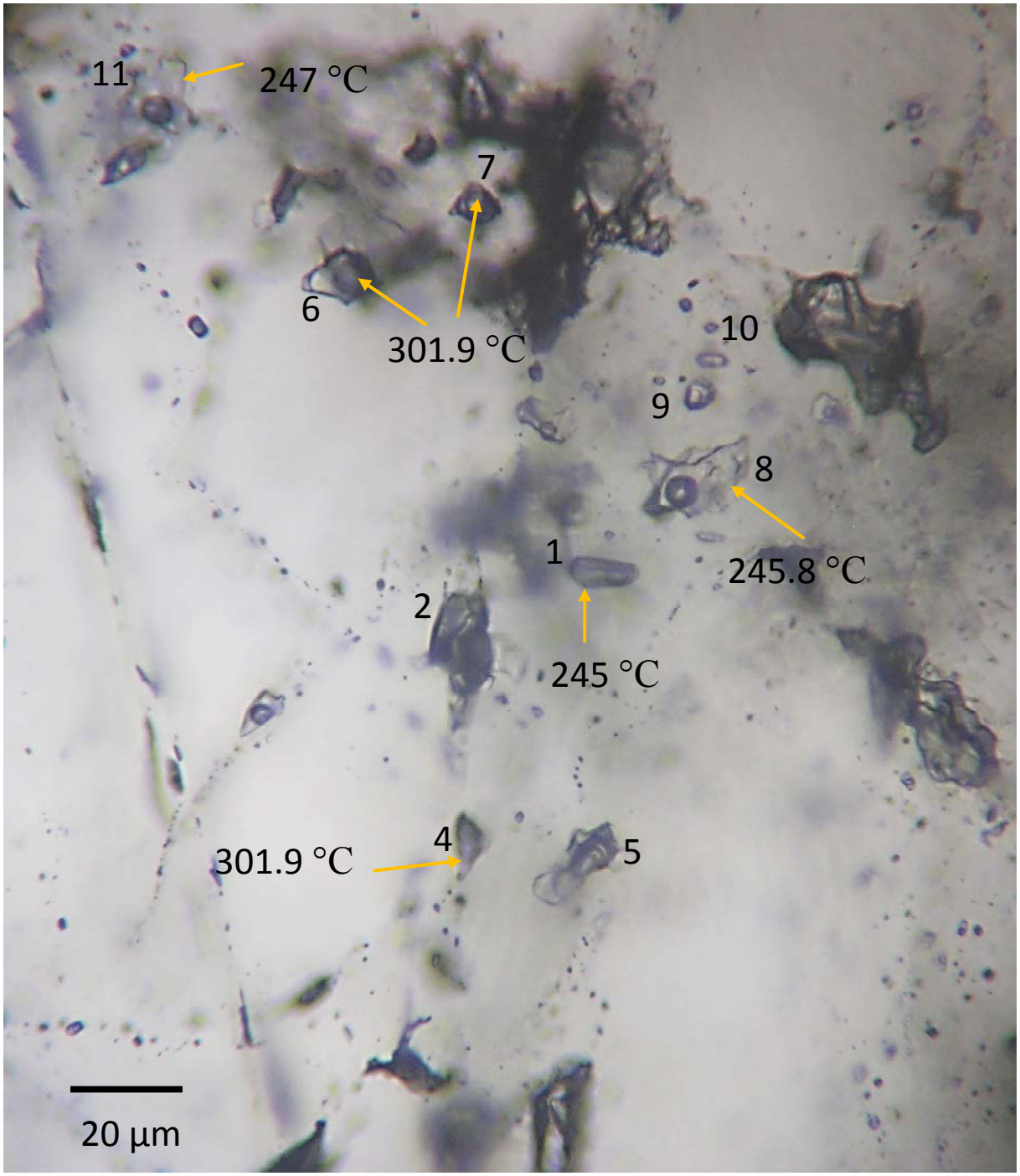

Figure 21: Thin section photograph of Hidden Hand fluid inclusion population. Salinity from Tm_{clath} is negative but Tm_{ice} gives regular salinity values (7 wt% $NaCl_{eq}$). Each of the CO_2-rich inclusions had Th_{CO2} to liquid and Th to CO_2 liquid while the two-phase aqueous inclusion homogenized to H_2O liquid.

Two daughter minerals were found during the study. Only one halite daughter mineral was found. Th for the inclusion was 284 °C and the dissolution of the halite was 284 °C. Salinity was calculated from Equation 3

$$S = 26.242 + 0.4928\Psi + 1.42\,\Psi^2 - 0.223\,\Psi^3 + 0.04129\,\Psi^4 + 6.295*10^{-3}\,\Psi^5 - 1.967*10^{-3}\,\Psi^6 + 1.1112*10^{-4}\,\Psi^7 \quad (3)$$

where Ψ is Tm_{halite} °C/100 and S is salinity. Calculated salinity for the inclusion was 37.0 wt% $NaCl_{eq}$. The equation is from Bodnar and Vityk, 1994. The only other daughter mineral found was dawsonite ($NaAlCO_3(OH)_2$). Attempts were made to identify the daughter minerals by laser microRaman but were unable to verify the mineralogy. Unlike the halite many dawsonite daughter minerals were found. Inclusions with dawsonite range in Th from 303.4 to 330.2 °C. Figure 22 displays a typical assemblage where dawsonite can be found. Figure 22A shows a type 1b, low salinity (0.3 wt% $NaCl_{eq}$) inclusion with a large dawsonite daughter mineral. Under PPL the dawsonite looks like tumbleweeds ranging from transparent to light brown (Figure 22B). Figure 22D is same image as Figure 22C in XPL, note the high birefringence of the solids, consistent with dawsonite.

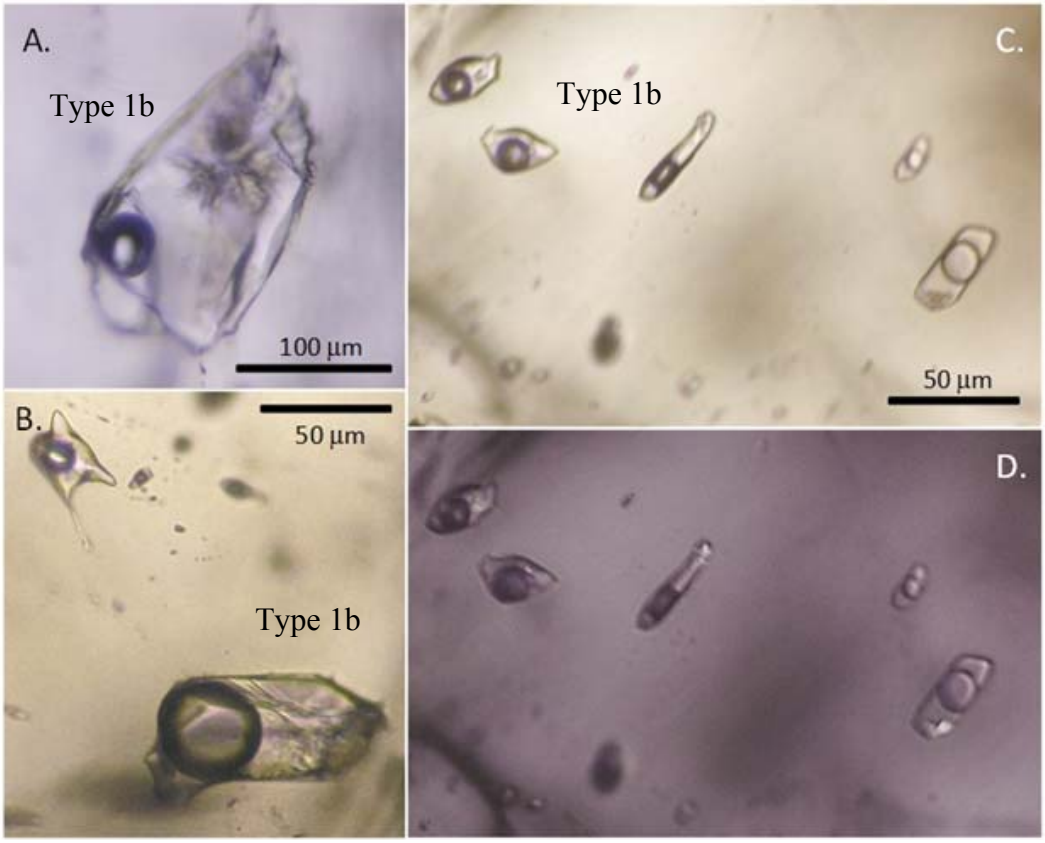

Figure 22: Microphotographs of fluid inclusions from the Bonanza mine that contain dawsonite (?) daughter minerals: A, B, C are in plane-polarized light. D is same image as C with crossed polars. Note the high birefringence of the solids, consistent with dawsonite.

3.6. Bulk Leachate

Two vein quartz sections and 3 amygdules were crushed for leachate testing. Table X shows the results from ICP-OES. Quartz samples were taken from the upper and lower Hidden Hand mines. These mines were chosen due to higher concentrations of fluid inclusions. JZ-HH (upper Hidden Hand) was yellow, perhaps stained by limonite, and JZ-HH-L (lower Hidden Hand) may have had minor disseminated sulfides. Samples JZ-A1 through JZ-A3 were amygdules. The amygdules were chosen due because of location in the alteration zone; JZ-A1 was in the sericitic alteration, JZ-A2 in the argillic alteration, and JZ-A3 in propylitic alteration. JZ-6 was the blank. The blank was prepared by adding 10 drops of HNO_3 to deionized water with no analytes to test the laboratory calibration standards. The units in Table X are of little

importance because the empirically derived equation (Equation 4) only relies on relative ratios of the solutes (Na/K) and (Ca/Na).

Table X: Bulk leachate results

Field ID	Ca	K	Mg	Na
JZ-A1	4.68	0.554	0.588	0.574
JZ-A2	3.54	0.492	0.265	0.518
JZ-A3	0.208	0.122	0.0128	0.416
JZ-HH	1.78	0.591	0.387	2.26
JZ-HH-L	2.29	0.322	0.462	1.89
JZ-6	<0.00748	<0.0542	<0.0128	<0.260

Units in mg/L

Since all samples contained Na-K-Ca-Mg, Equation 4 was used to determine temperature.

$$T = 1647/((\log (Na/K) + \beta*(\log\sqrt{(Ca)/Na}) + 2.47) - 273.15 \quad (4)$$

T is temperature in °C and $\beta = 1/3$. The value of β was chosen because $\log\sqrt{(Ca/Na)}$ is a positive number and yields a temperature greater than 100°C (Fournier and Truesdell, 1973). Calculated temperatures are 330°C, 263°C, 231°C, 344°C, and 341°C for samples JZ-A1 through JZ-HH-L, respectively. These temperatures overlap with Th values from the same veins. The Mg correction of Fournier and Potter (1979) was examined and deemed unnecessary because ΔT_{Mg} is a negative value, indicating Mg concentrations do not have a significant influence on the temperature.

3.7. Stable Isotopes

3.7.1. Sulfur

Approximately 100 samples were analyzed for sulfur isotopic composition and the raw data can be found in the Appendix (Table A-3). Figure 23 displays the range of $\delta^{34}S$ (VCDT) from pyrite, sphalerite, galena and arsenopyrite. Pyrite $\delta^{34}S$ values range from 4 ‰ to 8.8 ‰ and can be separated into Stage 1, pyrite associated with arsenopyrite, and Stage 2 pyrite associated

sphalerite and galena. Stage 1 pyrite are confined to analyses between 7 ‰ and 9 ‰. Stage 2 pyrite have a range from 4 ‰ to 7 ‰. Arsenopyrite displays a wider range of $\delta^{34}S$ from 2 ‰ to 7 ‰. Sphalerite has a $\delta^{34}S$ range of 3 ‰ to 8 ‰ and the highest number of analyses between 3 ‰ and 4 ‰. Galena $\delta^{34}S$ has a range of 1 ‰ to 5 ‰ with the greatest number of analyses around 1 ‰. The implications of the S-isotope data are discussed in the next chapter.

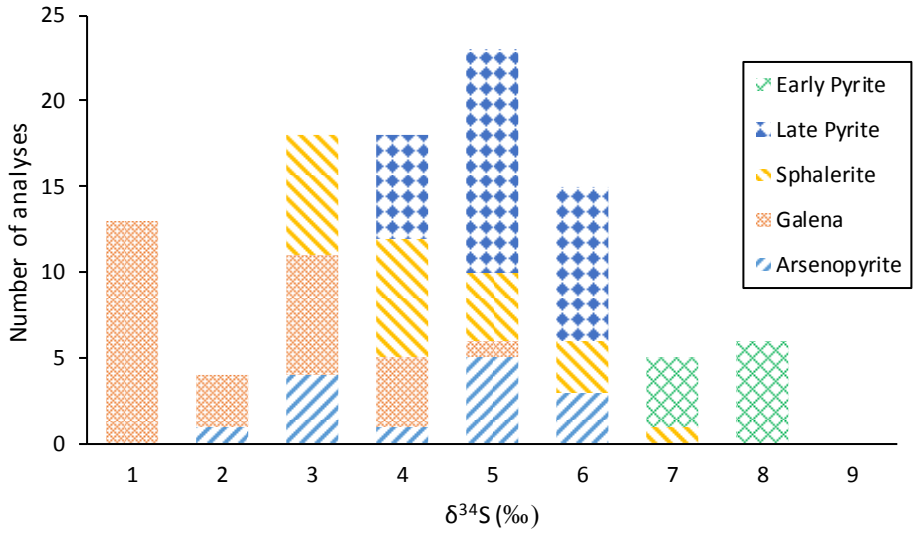

Figure 23: Sulfur isotope data. Pyrite is divided into early (Stage 1) and late (Stage 2).

3.7.1. Carbon-oxygen isotopes

C- and O-isotopic analyses were completed on 25 carbonate mineral samples representing various mines and mineralizing stages. The $\delta^{13}C$ ranged from -7.2 ‰ to -1.0 ‰ (VPDB) and $\delta^{18}O$ from 3.2 ‰ to 16.9 ‰ (VSMOW). Raw data can be found in Appendix (Table A-4). As can be seen from Figure 24, the $\delta^{13}C$ of carbonate minerals tends to increase with decreasing $\delta^{18}O$. Few definite trends can be seen between the various carbonate minerals, although kutnohorite and dolomite tend to plot in the lower right of Figure 24 (higher $\delta^{18}O$, lower $\delta^{13}C$) and ankerite and calcite in the middle or upper left (lower $\delta^{18}O$, higher $\delta^{13}C$). More robust trends between minerals may have been found if all of the samples were analyzed by

XRD to confirm the mineralogy. In this thesis, only the carbonate samples sent to the University of Nevada-Reno were identified by XRD.

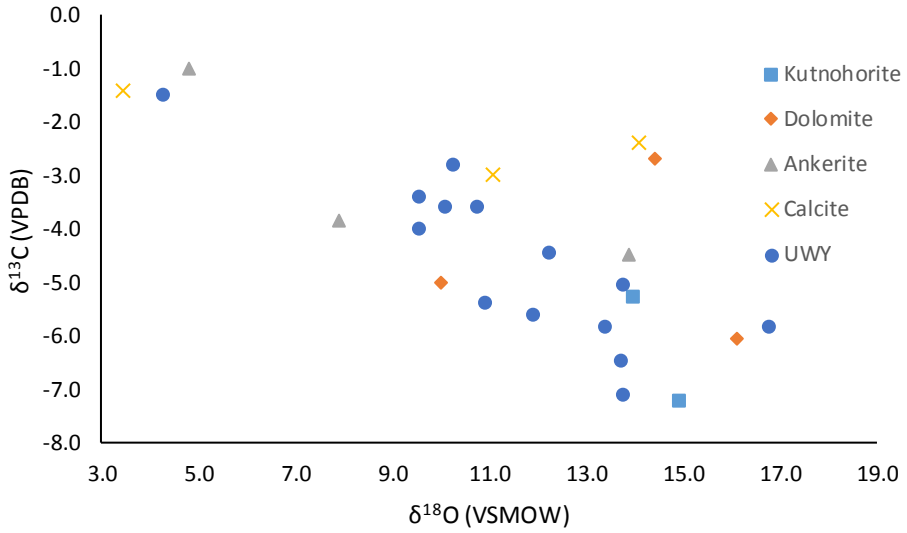

Figure 24: Carbon-oxygen isotopes from carbonates. Samples analyzed at University of Nevada – Reno were identified using XRD but samples analyzed at University of Wyoming (UWY) were not identified.

Implications of the carbonate isotope results, including possible reasons for the negative correlation between $\delta^{18}O$ and $\delta^{13}C$, are given in the next chapter.

4. Discussion

4.1. Temperature and Pressure of vein formation

Fluid inclusion data indicate the temperature for the system ranged from 127 to 353 °C. The upper range (280 to 340 °C) is dominated by CO_2-rich fluid inclusions while aqueous fluid inclusions were found across the entire temperature range. CO_2-rich inclusions (types 2 to 4a) are clustered around the 310 °C spike while type 3 inclusions indicate the early CO_2-rich fluid began decreasing in CO_2 concentrations and mixing with a denser brine.

An independent estimate for temperature was calculated using sph-gal S-isotope pairs.

$$1000\ln \alpha_{sph\text{-}gn} = 0.74 * 10^6 * T^{-2} + 0.08 - 273.15 \qquad (5)$$

Equation 5 is from Ding et al. (2003) and is valid between 300 and 600 °C. 14 sphalerite -galena pairs collected from the Emery District gave temperatures from 220 to 449°C with an average of 323 ± 73°C (Table XI). The average temperature of Stage 2 sulfide minerals based on S-isotope geothermometry is 62˚C higher than the average value of fluid inclusion homogenization temperatures from Stage 2 quartz. The difference between these two estimates is attributed to the fact that no evidence of boiling was found in Stage 2 fluid inclusions, and therefore a pressure correction needs to be applied to the Th data to estimate the true temperature of trapping (see below).

Pyrite – sphalerite and pyrite – galena pairs were also considered for geothermometry. The calculated temperature for pyrite – sphalerite averaged 243 ± 166 ˚C and pyrite – galena temperatures ranged 341 ± 92 ˚C. While the sphalerite and galena appear to have crystallized at approximately the same time, pyrite may have crystallized before and/or after both sphalerite and galena. Therefore, the numbers were not used in temperature estimations.

Although a pressure correction is needed to bring the results into agreement for Stage 2 fluid inclusions and S-isotope geothermometry of Stage 2 sulfide minerals, it is not obvious if the same pressure correction is needed for fluid inclusions from Stage 1, which precipitated pyrite and arsenopyrite. No S-isotope geothermometry data are available for Stage 1 with which to compare to the fluid inclusion data. However, evidence presented below suggests that the CO_2-rich Stage 1 inclusions were trapped at pressures similar to or greater than Stage 2. Applying the 62 °C pressure correction to the Stage 1 fluid inclusions (Th range of 280 to 340 °C averaging 303 ± 48 °C) yields a range of inferred trapping temperatures from 342 to 402 °C averaging 365°C.

Table XI: Sphalerite-galena (sph-gal) S-isotope pairs and respective temperature. Samples E-28 and E-37 were not used to calculate average temperature.

Sample	Mineral	Location	$\delta^{34}S$	Temp. (°C)
E-5-1GL	galena	Emma Darling mine	4.1	
E-5-1SP	sphalerite	Emma Darling mine	5.5	475.6
E-14-1GL	galena	Hidden Hand mine	1.7	
E-14-1SP	sphalerite	Hidden Hand mine	3.6	364.5
E-21-1GL	galena	Argus no. 6 adit	3.5	
E-21-1SP	sphalerite	Argus no. 6 adit	5.6	332.1
E-24-1GL	galena	Elizabeth mine	3.8	
E-24-1SP	sphalerite	Elizabeth mine	5.6	382.8
E-27-1GL	galena	Elizabeth mine	1.9	
E-27-1SP	sphalerite	Elizabeth mine	3.9	347.7
E-28-1GL	galena	Bonanza mine	3.9	
E-28-1SP	sphalerite	Bonanza mine	4.3	(1247.5)
E-31-2GL	galena	Bonanza mine	1.3	
E-31-2SP	sphalerite	Bonanza mine	3.5	317.7
E-32-1Gl	galena	Emery west shaft	1.1	
E-32-1SP	sphalerite	Emery west shaft	4.1	230.3
E-32-2GL	galena	Emery west shaft	1.9	
E-32-2SP	sphalerite	Emery west shaft	3.4	448.7
E-37-3GL	galena	Emery main shaft	2.2	
E-37-3SP	sphalerite	Emery main shaft	6.4	(150.7)
E-40-1GL	galena	Emery east shaft	2.1	
E-40-1SP	sphalerite	Emery east shaft	4.3	317.7
E-42-1GL	galena	Emery east shaft	1.8	
E-42-1SP	sphalerite	Emery east shaft	4.7	239.1
E-44-1GL	galena	Sterret mine	3.3	
E-44-1SP	sphalerite	Sterret mine	6.1	248.4
E-46-1GL	galena	Monday mine	4.1	
E-46-1SP	sphalerite	Monday mine	6.4	304.2
E-55-2GL	galena	Paymaster mine	1	
E-55-2SP	sphalerite	Paymaster mine	3.4	291.6
E-62-2GL	galena	Paymaster mine	2.3	
E-62-2SP	sphalerite	Paymaster mine	3.8	448.7

Geothermometry based on Na/K ratios in bulk fluid inclusion leachate samples indicates a temperature range from 231°C to 344°C (Table X) with an average of 302 ± 52°C. Bulk fluid inclusion leachates from vein quartz had temperatures of 341 and 344 °C while the amygdules had temperatures of 231, 263, and 330 °C. This result is in reasonable agreement with the fluid

inclusion and stable isotope data. It should be noted that bulk leachate results include all fluid inclusions in the quartz sample, and calculated temperatures may be skewed to lower temperatures if a large number of late, secondary fluid inclusions are present.

Assuming the Emery lodes are located near the bottom of the Elkhorn Mountain Volcanics (EMV), which are approximately 4.6 km thick (Smedes, 1966), the lithostatic pressure would have been approximately 1.3 kbars. This assumes a typical geobaric gradient of 3.5 km per kbar. This pressure estimate is shown as horizontal lines (labeled "EMV") on Figures 25 and 26.

An on-line calculator was used to estimate the density of the CO_2 phase at T = Th_{CO2} (Wischnewski, B http://www.peacesoftware.de/einigewerte/co2_e.html, accessed April 4, 2016). The majority of the CO_2–rich inclusions had Th_{CO2} to liquid CO_2, and had ρCO_2 near 0.6 g/cm^3 with one outlier at 0.8 g/cm^3. Inclusions with Th_{CO2} to vapor had a lower CO_2 density, from 0.1 to 0.3 g/cm^3. Additional information from the carbonic fluid inclusions are plotted on Figure 25 (modified after Brown and Lamb, 1989). This figure assumes a ρCO_2 of 0.6 g/cm^3 and a salinity of 0 wt% $NaCl_{eq}$, consistent with the fluid inclusion data. The thin black lines represent the estimated volume of the CO_2 phase at T = Th_{CO2}. The carbonic fluid inclusions occupied roughly 40 to 70% of the total fluid inclusion volume at T = Th_{CO2}. The x-axis in Figure 25 is the temperature of final homogenization of the carbonic fluid inclusions. The blue square was drawn using the range of final homogenization temperature (245 to 341°C) and ±1 standard deviation for the volume of the carbonic phase at room temperature (62.5 ± 18%). The circle represents the average Th (311 ± 20°C) and ± 1 standard deviation for volume of the carbonic phase at room temperature. The red circle shows the most representative range in trapping pressure for the carbonic fluid inclusions at Emery. Estimated trapping pressures (thin blue

lines) are 1.2 to 1.7 kbars and straddle the pressure estimated based on the thickness of the EMV. Fluid pressures greater than lithostatic pressure could explain the formation of the low-angle veins, which would require lifting of the overlying rock.

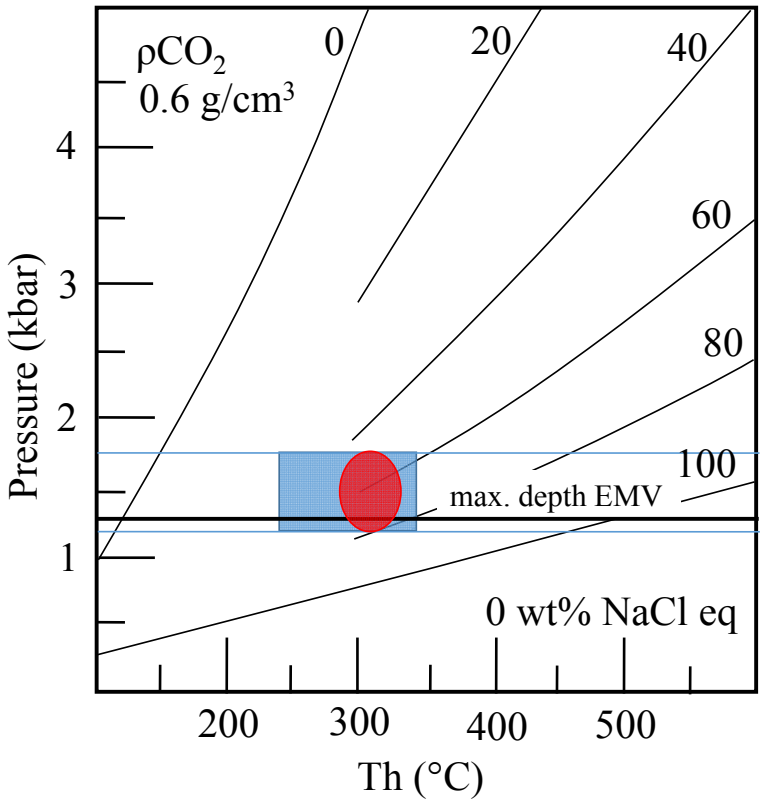

Figure 25: P-Th diagram for CO_2-rich fluid inclusion. The thin black lines correspond to the volume percent of CO_2 phase at Th_{CO2}. The CO_2 density (ρCO_2) is 0.6 g/cm^3 with 0 wt% $NaCl_{eq}$. The thick black line corresponds to the maximum depth of the EMV. The bounding temperatures are Th = 245 °C and 341 °C. The thin blue lines represent the pressure range for CO_2-rich inclusions (1.2 to 1.7 kbar). Modified after Brown and Lamb, 1989.

Since most of the fluid inclusion data came from aqueous fluid inclusions another pressure estimation was calculated. Figure 26 shows the estimated pressure for the aqueous fluid inclusions where the thin lines represent isochores for liquid-rich fluid inclusions that homogenize to the temperatures of the labels. The shaded region corresponds to the range in temperature and pressure of the ore-forming fluids at the Emery District. The upper pressure

limit is set to 1.3 kbars, corresponding to the total thickness of the EMV (Smedes, 1966). The left and right limits are set by ± 1 standard deviation for the Th (± 53 ˚C) of all aqueous fluid inclusions in this study. The red circle shows the most likely temperature and pressure conditions based on the average Th value (264 ˚C) and the average temperature given by S-isotope geothermometry of sphalerite - galena pairs (323 ˚C). This value corresponds to a pressure of 1.1 to 1.2 kbars, and is close to the estimated lithostatic pressure based on the total thickness of the EMV.

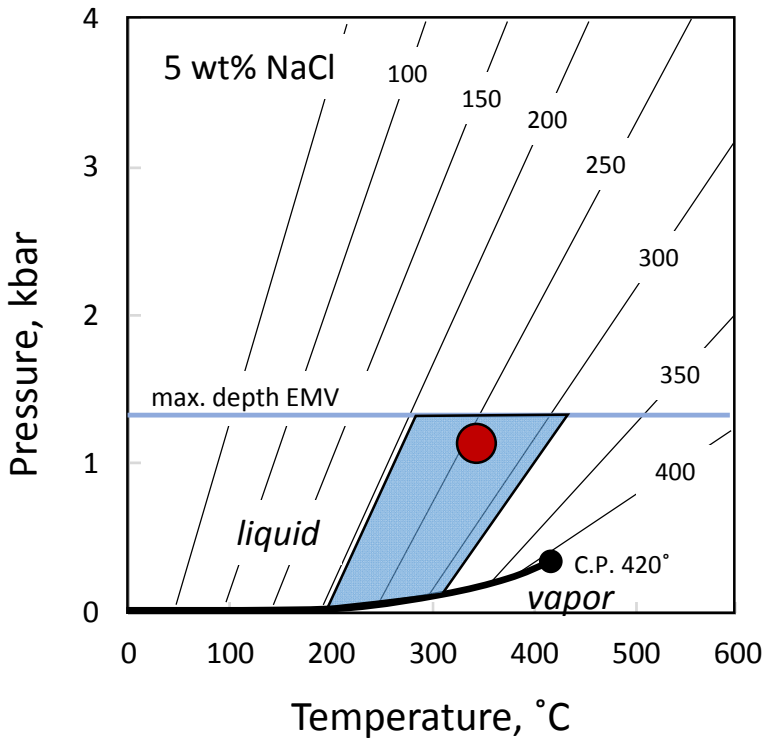

Figure 26: P-T diagram for 5 wt% $NaCl_{eq}$. The thin black lines correspond to Th for the fluid inclusion. The thick black line represents the L-V curve with a black dot representing the critical point (C.P.) at 420°C. The thick blue line shows lithostatic pressure based on maximum depth of EMV. The shaded region corresponds to ±1 standard deviation for Th after S-isotope geothermometry correction. The red circle indicates the probable P-T conditions based on average Th (264 °C) and average S-isotope geothermometry (340 °C). Image modified after van den Kerkhof, 2011.

CO_2-rich inclusions appear to indicate the maximum pressure of the EMV was exceeded and average aqueous fluid inclusion Th and S-isotope geothermometry indicate pressure very close to that of the max EMV. Once the maximum EMV pressure was exceeded the rock brecciated and/or lifted creating low angle veins. This appears to be plausible as the most productive veins in the Emery District were low-angle veins. Due to the apparent depth of formation (>4 km) the veins are presumed to be deep epithermal to mesothermal.

4.2. Mineral Chemistry

Combining the range of atomic % As in arsenopyrite (29 % to 30 %) from EPMA results (Table V) with the mineral assemblage arsenopyrite (aspy) and pyrite (py), a temperature range can be estimated using Figure 27. The dashed lines represent the atomic % of As in arsenopyrite and solid lines represent changes in mineralogy. Sharp et al. (1985) found that pressure does not have a large effect on the position of the arsenopyrite compositional contours. The red region is the probable range of arsenopyrite formation based on a composition of 29 to 30 atomic % As. It is bounded by the fugacity of S_2 of $10^{-10.5}$ to $10^{-7.8}$ and a temperature range of 300°C to 360°C. It is worth noting arsenopyrite may be stable at temperatures lower than 300°C, beyond the scale of the figure. However, the shaded range of 300 to 360˚C is in reasonable agreement with the various geothermometers discussed above.

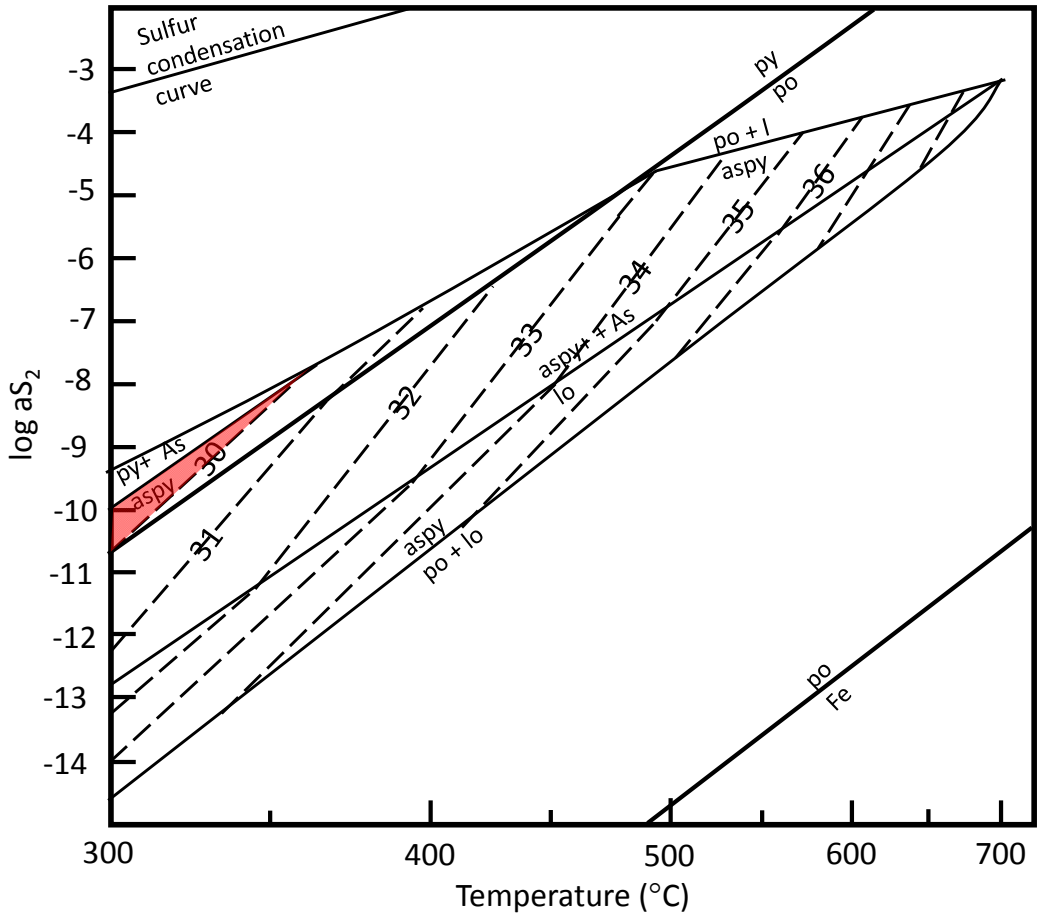

Figure 27: Arsenopyrite geothermometry. Solid lines correspond to phase changes while dashed lines correspond to atomic% As in arsenopyrite. The red region shows the probable range of formation for Emery arsenopyrites. Abbreviations used Fe (native Fe), po (pyrrhotite), lo (löllingite). Modified after Kretschmar and Scott, 1976.

In the Emery lode, sphalerite can be used as a fugacity of S_2 indicator. Using Equation 6 (Barton and Skinner, 1979)

$$\log X_{(py)} = 7.16 - 7730 * T^{-1} - .5 \log aS_2 \qquad (6)$$

where $X_{(py)}$ is the X_{FeS} in sphalerite (X_{FeS} = 0.06 and 0.12) from EPMA data (Table III), T is in Kelvin, and aS_2 is equivalent to the fugacity of S_2. Using the temperature range for Stage 2 (282 to 342 °C, after 62 °C pressure correction) a fugacity of S_2 was calculated between $10^{-11.7}$ and $10^{-8.4}$. The pyrite equation was chosen because very little pyrrhotite was found during the study and petrographic evidence suggests sphalerite crystallized with pyrite.

Electrum composition in combination with X_{FeS} in sphalerite can be used to find temperature (Gammons and Williams-Jones, 1995). Figure 28 displays the X_{Au} in electrum and X_{FeS} in sphalerite against S_2 fugacity buffers such as py-po, py-hm-mt, and bn-py-cpy with dashed lines representing X_{FeS} in sphalerite. The red region is restricted by X_{Au} (0.565 and 0.579) in electrum and X_{FeS} (0.06 to 0.12) in sphalerite. The region indicates a temperature range of 340 to 380 °C. Petrographic evidence (Figure 7B and 7C) indicates the electrum found in this study formed during Stage 2.

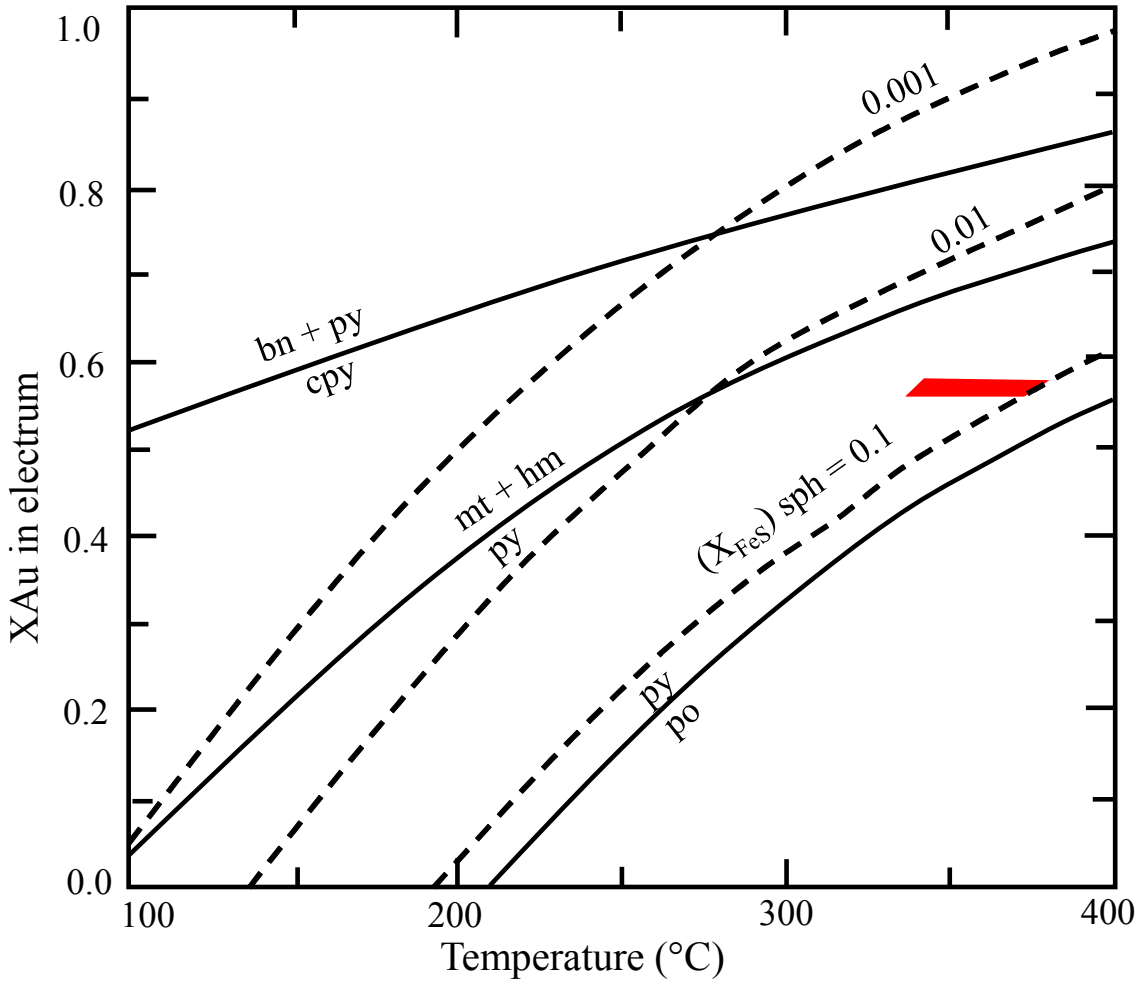

Figure 28: X_{Au} in electrum and temperature of formation. Solid lines correspond to fugacity of S_2 buffers. Abbrev. for the lines are py (pyrite), po (pyrrhotite), hm (hematite), mt (magnetite), bn (bornite), and cpy (chalcopyrite). Dashed lines represent X_{FeS} in sphalerite (sph). The red box represents the X_{FeS} range (0.06-0.12) and X_{Au} (0.565 and 0.579). Estimated temperature from the figure is 340°C to 380°C. Modified from Gammons and Williams-Jones, 1995.

Figures 27 and 28 are in relatively good agreement. The estimated temperature for electrum (340 to 380 °C) is slightly higher than the estimated temperature for arsenopyrite (300 to 360 °C) but they do overlap. The figures may imply electrum deposition occurred prior to arsenopyrite, but textural evidence suggests it occurred after arsenopyrite. EPMA data (Table V) indicates there may be submicron Au in the arsenopyrite (690 ppm from 1 analysis) and may indicate at least some simultaneous deposition of gold and/or electrum with Stage 1 sulfides. The fugacity of S_2 estimated from Figure 27 ranged from $10^{-10.5}$ to $10^{-7.8}$ and the fugacity of S_2 estimated using Equation 6 ranged from $10^{-11.7}$ and $10^{-8.4}$ possibly indicating decreasing fugacity of S_2 from Stage 1 to Stage 2.

4.3. Fluid-Rock Interaction and Metal Deposition

Fluid inclusion data for aqueous fluid inclusions indicate that salinity did not vary much throughout the system during Stage 2 mineralization, although there is a slight trend of decreasing salinity with decreasing temperature (Figure 18). It is also plausible that the ore minerals may have been precipitating at approximately the same time giving intergrowths, especially during Stage 2.

Fluid inclusion evidence suggests the early CO_2-rich fluid did not have much salinity and was not the carrier of metals but created favorable conditions for vein genesis. As the CO_2-charged fluid reacted with labradorite and bytownite in the wall rock, CO_2 was converted to HCO_3^- as in Equation 7.

$$2CO_2 + 2Na_{.5}Ca_{.5}Al_{1.5}Si_{2.5}O_{8(s)} + 5H_2O \rightarrow Na^+ + 3Al(OH)_{3(aq)} + HCO_3^- + CaCO_{3(s)} + 5SiO_{2(s)} \quad (7)$$

The solutes on the right side of Equation 7, although soluble at the temperature of the hydrothermal fluids, precipitated out as dawsonite daughter minerals during cooling of the primary fluid inclusions. The majority of fluid inclusions containing dawsonite had a Th above

300 °C, the exception is one type 1b with a Th of 214 °C. The dawsonite-bearing fluid inclusions (types 1b and 4a) generally have little to no salinity. Coveney and Kelly (1971) indicate dawsonite formation needs stable, basic conditions for crystallization. Conditions within a fluid inclusion are stable and representative of the hydrothermal fluid, which, according to Equation 7, was becoming more basic during wallrock alteration as CO_2 was converted to HCO_3^-. Equation 8 shows the solutes needed for dawsonite formation.

$$Na^+ + Al(OH)_{3(aq)} + HCO_3^- \rightarrow NaAlCO_3(OH)_2 + H_2O \quad (8)$$

Notice, all of the solutes necessary for dawsonite formation are released in Equation 7. Equation 8 offers an explanation for why type 1b and 4a fluid inclusions have little to no salinity and little to no liquid CO_2. Precipitation of dawsonite would have decreased the concentrations of dissolved solutes, such as Na^+ and HCO_3^-, thereby decreasing the salinity of the remaining fluid.

During analysis of a chip from the Hidden Hand mine, coexisting aqueous and CO_2-rich inclusions were found with similar Th. The population appears to indicate effervescence of the CO_2 phase around 245 to 247 °C. This trend appears to be consistent, as only one CO_2-rich inclusion was found below Th of 245 °C.

Reaction with wallrock and effervescence of the CO_2 phase drove carbonate precipitation and increased the pH, simultaneously driving sulfidation of Fe-bearing carbonates (ankerite and ferroan dolomite) to pyrite (Equation 9) and arsenopyrite as well as precipitating Au (Equation 10).

$$CaFe(CO_3)_2 + 2H_2S + 2H^+ \rightarrow FeS_2 + 2H_2O + 2CO_2 + Ca^{2+} + H_2(g) \quad (9)$$

Equation 9 shows the sulfidation of ankerite to pyrite and a similar reaction can be used for arsenopyrite. The sulfidation reaction consumes two moles of acid increasing the pH. Production of H_2 (aq) and consumption of H_2S through sulfidation drives the destabilization of

$Au(HS)_2^-$ or Au(HS)(aq), depending on initial pH (Gammons and Williams-Jones, 1995), as evidenced by Equations 10 and 11. Gammons and Williams-Jones (1995) indicate dissolved Au is more stable in most hydrothermal systems as $Au(HS)_2^-$ and may form a richer deposit over $AuCl_2^-$.

$$Au(HS)_2^- + 1/2H_2 + H^+ \leftrightarrow Au + 2H_2S \quad (10)$$

$$Au(HS)(aq) + ½H_2 \leftrightarrow Au + H_2S \quad (11)$$

Destabilization of $Au(HS)_2^-$ consumes 1 mole H^+ and ½ mole $H_2(g)$ as well as precipitating gold and creating H_2S. Under the above conditions metal-chloride complexes (such as that for the base metals and Ag) would not be effected. The base metals (Pb, Zn, Cu, Fe, Mn) and Ag were most likely transported as chloride complexes and therefore were unaffected by the initial sulfidation of wallrock and precipitation of gold from Equations 9 and 10.

The moderate salinity values obtained from fluid inclusion analyses indicates that the base metals were most likely transported as chloride complexes. Reed and Paladrini (2006) indicate that the simple sulfides from Stage 2 (galena, sphalerite, chalcopyrite) are stable in near-neutral to basic conditions around 300°C. Under more acidic conditions, base metals (Pb, Zn, Cu, Fe, Mn) and Ag dissolve as metal-chloride compounds. Chloride compounds can be destabilized through increasing pH or decreasing temperature. As CO_2 effervesces the pH is expected to rise and acid (H^+) is also consumed in Equations 9 and 10, fitting one of the two ways to destabilize chloride complexes. Also, as the fluid moves away from its heat source it begins to cool and further destabilizes chloride complexes.

Deposition of silica from H_4SiO_4 at higher temperatures (above 200 °C) promotes quartz growth over amorphous silica gels (Gunnarsson and Arnórsson, 2000). In the vein sections in the Emery District this can be seen from the euhedral quartz in Stage 1 and into Stage 2.

Thermodynamic calculations indicate H_3AsO_3 is the dominant aqueous arsenic species in acid to neutral hydrothermal fluids (Heinrich and Eadington, 1986). Also, at mildly acidic and Cl-rich conditions, dissolved Fe is probably transported as a chloride complex, such as $FeCl^+(aq)$ (Palmer and Hyde, 1993). The following reaction shows how simple precipitation of arsenopyrite from a hydrothermal fluid is a redox reaction dependent on the activity of O_2 (see also Heinrich and Eadington, 1986):

$$H_3AsO_3(aq) + FeCl^+(aq) + H_2S(aq) = FeAsS(s) + 3/2H_2O + Cl^- + 2H^+ + 3/2O_2 \quad (12)$$

However, the following reaction shows that when pyrite and arsenopyrite are precipitated together, the reaction is independent of the activity of O_2:

$$2H_3AsO_3(aq) + 5FeCl^+(aq) + 8H_2S(aq) = 2FeAsS(s) + 3FeS_2(s) + 6H_2O + 5H^+ + 10Cl^- \quad (13)$$

Thus, a simple drop in the activity of H^+ (increase in pH) could precipitate both pyrite and arsenopyrite, with no need for any separate redox reactions. Cooling would also tend to precipitate the sulfide minerals, although Heinrich and Eadington (1986) suggested that cooling is relatively less important for arsenopyrite deposition compared to other mechanisms.

The hydrothermal geochemistry of antimony is very complex, and is best summarized in the papers of Pokrovski et al. (2006) and Obolensky et al. (2007). According to Pokrovski et al. (2006), antimony most likely dissolves into mildly acidic hydrothermal fluids in the trivalent (Sb^{+3}) redox state as complexes such as $Sb(OH)_3(aq)$, $SbCl_4^-$, or mixed hydroxy-chloride complexes (e.g., $SbCl_3OH^-$), depending on pH and salinity. At higher pH and H_2S concentrations, sulfide complexes, such as SbS_2^-, become important (Obolensky et al., 2007). Given the close association of Sb as boulangerite along with the other common base metal sulfides (sphalerite, galena) at Emery, it is logical to assume that dissolved Sb was transported as a chloride complex and precipitated at the same time as Pb, Zn, Cu due to cooling, dilution,

and/or pH increase. The following reaction shows one possible way to precipitate boulangerite from a hydrothermal brine:

$$5PbCl_3^- + 4SbCl_4^- + 11H_2S = Pb_5Sb_4S_{11} + 31Cl^- + 22H^+ \quad (14)$$

4.4. Sources of ore-forming constituents

The original fluid appears to be magmatically derived due to the presence of early, three phase CO_2-rich fluid inclusions (types 2 through 4a), and later aqueous brines with moderate salinity between 5 and 8 wt% $NaCl_{eq}$. Th indicate a cluster of type 2 to 4a fluid inclusion analyses (Figure 16A) between 350 and 400 °C, after a 62 °C pressure correction. As the fluid reacted with the wall rock (Equation 7) the fluid inclusion types shifted from type 4a to type 2. Metals could have easily been transported as chloride complexes from a magmatically derived fluid. Other ore-forming constituents, such as sulfur and carbon, were probably also magmatically derived, but possibly from a magma that was enriched in S and C by assimilation of crustal rocks, including the Belt-Purcell Supergroup metasediments.

Figure 29 (modified from Field et al., 2005) summarizes the S-isotope composition of selected hydrothermal mineral deposits and S-rich sedimentary rocks in the area that is underlain by the Belt-Purcell basin. The Newland Fm. of the lower Belt Supergroup contains extensive deposits of sedimentary pyrite and barite, the former ranging from -9 to +37 ‰ and the latter from +13.6 to +18.3‰ (see Field et al., 2005 for a list of references). Higher in the Belt stratigraphy, stratabound pyrite and Cu-sulfide minerals in the Revett Fm. are also isotopically heavy (+3 to +23 ‰). Thus, on average, sulfur in the Belt metasediments is likely to be isotopically much heavier than magmatic S sourced from the mantle (0 ‰, Ohmoto, 1972). Field et al. (2005) argued that magmatic assimilation of S from the Belt metasediments provides the best explanation for the heavy $\delta^{34}S$ value of bulk S (including both sulfide and sulfate

minerals, i.e., anhydrite) in the magmatic-hydrothermal deposits of Butte. Assimilation of Belt sulfur by magmas that eventually released the same S as hydrothermal fluids could also explain the range of $\delta^{34}S$ for pyrite in the Emery veins and lodes (+1 to +8.8 ‰).

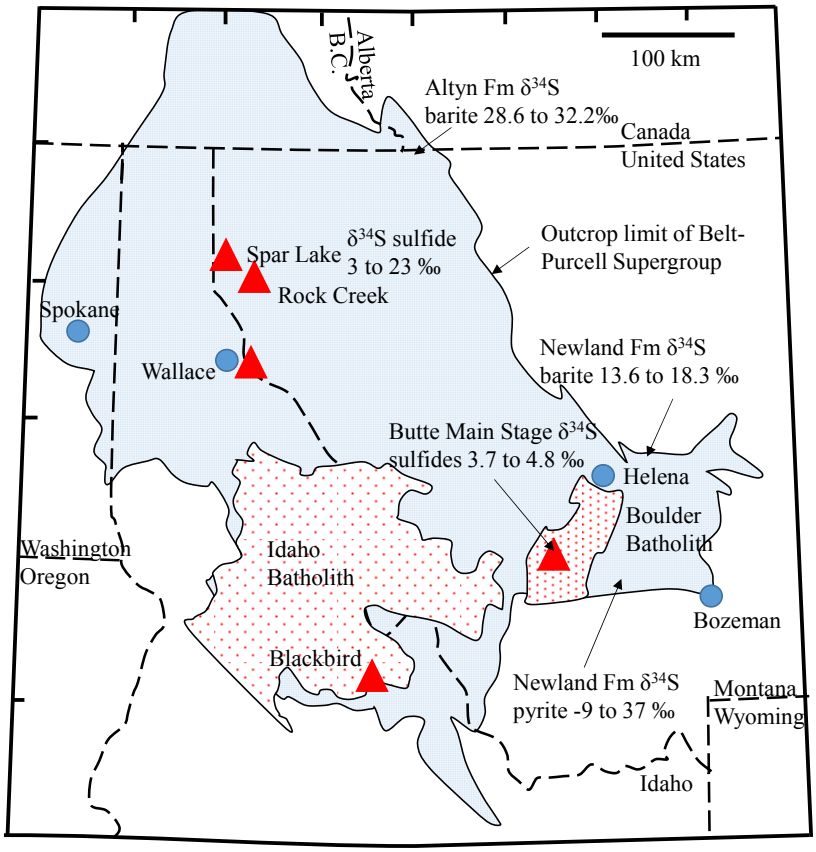

Figure 29: Sulfur isotope ranges from various mines associated with the Belt-Purcell Supergroup. The pale blue region delineates the outcrop limit of the Belt-Purcell Supergroup. The textured bodies correspond to the Boulder and Idaho batholiths. Major cities are shown by blue circles. Red triangles represent mines. Modified after Field et al., 2005.

Since sulfur isotopes indicate a possible influence from the Belt-Purcell Supergroup, it is not outlandish to examine the possibility that a similar trend exists with C-isotopes. Hall and Veizer (1996) found $\delta^{13}C$ from the Lower and Middle Belt limestones and dolomites fall between +1 and +2.5‰ (VPDB), after correcting for alteration. The numbers are similar to other Mesoproterozoic marine carbonates. Meanwhile, magmatically derived CO_2 is generally considered to have a $\delta^{13}C$ of approximately -5‰ (VPDB) (Ohmoto and Rye, 1979). In

comparison, C isotopes at Emery range from -7.2 to -1 ‰ (VPDB). The data from Emery overlaps with "magmatic CO_2", extending to heavier values, possibly due to assimilation of Belt carbonate rock.

To explain the negative correlation between $\delta^{13}C$ and $\delta^{18}O$ in the carbonate minerals of Emery (Figure 24), it is necessary to first discuss the range of $\delta^{18}O$ in different types of hydrothermal fluids. The $\delta^{18}O$ of a magmatically derived water at approximately 300°C should fall between +6 and +9‰ (VSMOW) with an average near +7.5 ‰ (e.g., Taylor, 1979). In contrast, heated groundwater derived from the atmosphere (meteoric water) has much lighter $\delta^{18}O$ values, typically between -5 and -20 ‰, depending on paleoclimate, paleolatitude, and other variables. Another factor that needs to be considered is the isotopic fractionation that takes place between H_2O and carbonate minerals, and the fact that this fractionation is strongly temperature dependent. At T > 200˚C, carbonate minerals such as calcite have lower values of $\delta^{18}O$ compared to the water from which they precipitate. At T < 200˚C, this relationship reverses (e.g., Ohmoto and Rye, 1979).

Two scenarios are considered to explain the negative correlation between $\delta^{13}C$ and $\delta^{18}O$ in the carbonate gangue minerals at Emery: (1) a single magmatic fluid that cools, and (2) mixing of hotter magmatic water rich in CO_2 with cooler meteoric water poor in CO_2. If the effect is simply due to cooling of a single magmatic CO_2 source with a $\delta^{13}C$ of -5‰ (VPDB), then a calcite that formed at 350 °C would be 2.4‰ *lighter* (-7.4‰), which is close to the lower end in the spread of $\delta^{13}C$ data from the Emery veins (Figure 24). If calcite forms at a cooler temperature such as 200 °C, the $\delta^{13}C$ signature of the carbonate mineral would be *similar* to that of the CO_2 (-5‰). If the calcite formed at 100 °C the $\delta^{13}C$ would be 4‰ *heavier* (-1‰) (Beaudoin, G & Therrien, P., 2009), which is close to the maximum value of $\delta^{13}C$ in the Emery

carbonate minerals (Figure 24). In other words, the more negative $\delta^{13}C$ carbonates could have formed at higher temperature and the more positive $\delta^{13}C$ carbonates at a lower temperature.

If we assume a 100% magmatic fluid with an initial $\delta^{18}O$ of +7.5‰ (VSMOW), a calcite that formed from the fluid at 350 °C would be 4.6‰ heavier in $\delta^{18}O$ (+12.1‰). The difference becomes more pronounced at lower temperatures. If the $\delta^{18}O$ value of the water is kept at +7.5‰, at 200 °C a calcite will be 9.8‰ heavier than the water and at 100 °C a calcite would be +18‰ heavier. This means a magmatic fluid with $\delta^{18}O$ = +7.5‰ would form a calcite with a $\delta^{18}O$ of +12.1‰ at 350˚C, +17.3 at 200˚C, and +25.5‰ at 100°C (Beaudoin, G & Therrien, P., 2009). The preceding paragraph showed that simple cooling would produce carbonate minerals that become increasingly enriched in $\delta^{13}C$. Thus, the expected trend if carbonate minerals continuously precipitated from a single magmatic fluid that cooled from 350°C to 100°C would be a positive relation between $\delta^{18}O$ and $\delta^{13}C$, which is not what is seen at the Emery District. This idea is illustrated conceptually as Path "A" of Figure 30, below.

If there was a combination of fluid mixing and cooling, it would likely be between a hotter CO_2-rich magmatic fluid and a cooler CO_2-poor meteoric water. If, as in the first possibility, the upper left endmember on Figures 24 and Figure 30 formed at a lower temperature (100 °C) with a $\delta^{18}O$ of +3.4‰ then the water it formed from would have to be 18‰ lighter (-14.6‰ VSMOW), which is a typical value for meteoric water. Therefore, the trend in the data shown in Figure 24 could possibly be explained by mixing of a hot, CO_2-rich magmatic fluid with a cool, CO_2-poor meteoric fluid. This idea is shown by Path "B" in Figure 30.

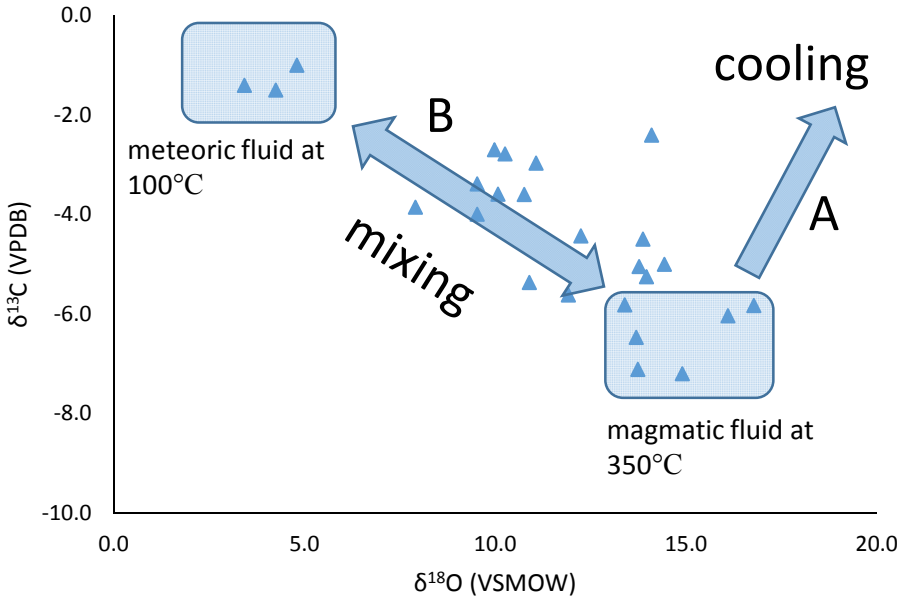

Figure 30: Isotope cross plot for carbonate minerals at Emery showing possible fluid end-embers and processes discussed in the text

4.5. Comparison to other mining districts

Polymetallic veins are found throughout the Boulder Batholith. Total metal production from two of the bigger mines (Alta and Comet) and the Emery District are displayed on Figure 31. Together the three mines cover the east (Alta), west (Emery) and middle (Comet) of the Boulder Batholith. The Comet mine is hosted by the Butte Granite near the roof of the batholith and is approximately 8 km long with 45.7 m of mineralization and strikes roughly N 80° W with nearly vertical dip (Becraft et al., 1963). Ore mineralogy for the lode was sphalerite, galena, and pyrite with some arsenopyrite, chalcopyrite, and tetrahedrite. Gangue mineralogy was quartz, carbonate minerals and, altered wallrock. The lode is locally overlain by the EMV and Eocene Lowland Creek Volcanics (Becraft et al., 1963). The Alta mine is hosted by the EMV, within 1 km of the inferred contact with the Boulder Batholith, in an east-trending shear zone. The vein strikes N 80° W and dips 65° N. Vein mineralogy was quartz, pyrite, sphalerite, arsenopyrite, galena and some chalcopyrite (Becraft et al., 1963).

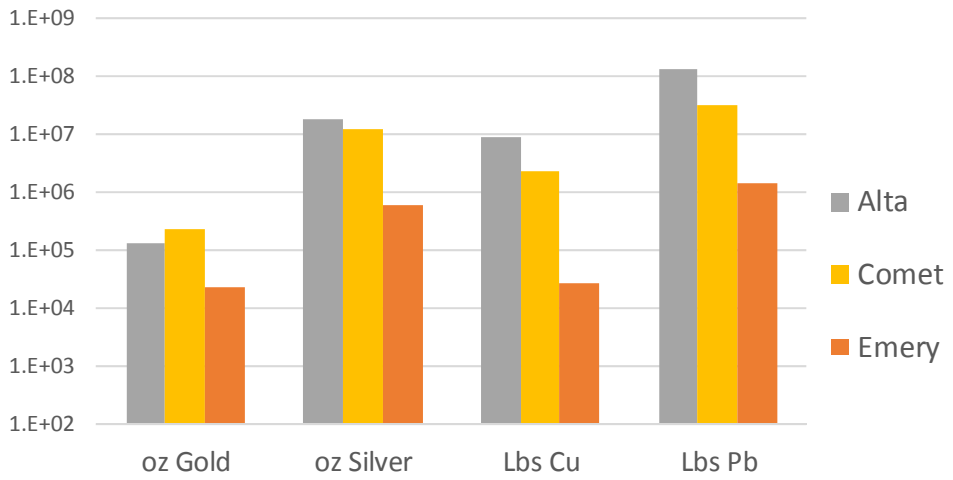

Figure 31: District production from Alta, Comet, and Emery mining districts. Information from Becraft et al., 1963.

The Alta and Comet lodes occupied steeply dipping, east-west trending structures, similar to most of the more productive mines from the Boulder Batholith (Becraft et al, 1963), including the "Anaconda" set of veins and lodes at Butte. Emery, conversely, was most productive from low angle (10° to 40° NW) "bedding plane" fissures. Although metal production from Emery was less than Alta and Comet, most of the veins at Emery were less than a foot thick (Robertson, 1953) whereas the Comet and Alta lodes were much more extensive. Vein mineralogy is quite similar at each mine, with the exception of boulangerite in the Emery District.

Boulangerite, while an uncommon mineral, is still found in several mines associated with the Boulder Batholith. Of all the mining activity across the Boulder Batholith only the Aurora mine (Basin District), Little Sampson mine (Rimini District), and Charter Oak mine (Elliston District), in addition to the Blue-Eyed Maggie, Ding Bat, and Emery mines in the Emery District contain boulangerite (mindat.org, 2016). These mines all bound the north western edge of the Boulder Batholith. The Black Pine mine (Philipsburg District), west of the Boulder Batholith, contains boulangerite and similar style low-angle veins to the Emery District, although the Black

Pine mine is hosted by Belt metasediments. Farther west in the Superior District and Coeur d'Alene District in the eastern Idaho panhandle, boulangerite is a common ore mineral.

Sphalerite and pyrite isotopes were compared between the Emery and Butte Districts. Sphalerite and pyrite from Butte range from - 2 to + 3.2 ‰(VCDT) and - 1.8 to + 3.9 ‰ (VCDT), respectively (Field et al., 2005), and Emery range from + 3 to + 8 ‰ (VCDT) and + 4 to + 9.8 ‰ (VCDT), respectively. The Emery lodes appear to be slightly enriched in $\delta^{34}S$ over Butte. This may imply some input of country rock (Belt-Purcell Supergroup metasediments) because magmatically derived $\delta^{34}S$ should be approximately 0‰ to slightly negative (Field et al., 2005), however, the isotopic signature could have been derived from assimilation of another package of country rock.

Carbon-oxygen isotopes from carbonate minerals at Emery are similar to those from siderite and ankerite from the Coeur d'Alene district in Idaho. Figure 32 displays average $\delta^{13}C$ and $\delta^{18}O$ from Eaton et al. (1995) and Rosenberg and Larson (2000). Emery $\delta^{13}C$ ranges from - 7.2 to - 1 ‰ (VPDB) and appears to correlate with an area from Bullion, Mt to White Cap, Mt and possibly including the Sunshine mine in Kellogg, Id. The $\delta^{18}O$ values on Figure 32 have a large range and only appear to cluster by average. Emery $\delta^{18}O$ become depleted as $\delta^{13}C$ are enriched. Oxygen isotopes display wider variation due to the style of deposit (orogenic/metamorphic at Coeur d'Alene, porphyry-Cu at Butte, and hydrothermal at Emery). Oxygen isotopes are also frequently reset by interaction with groundwater, as may be the case at the Emery District. Due to the differences in water-rock reactions between the metamorphosed deposits in the Coeur d'Alene District and the hydrothermal deposit at Emery, $\delta^{18}O$ are not considered.

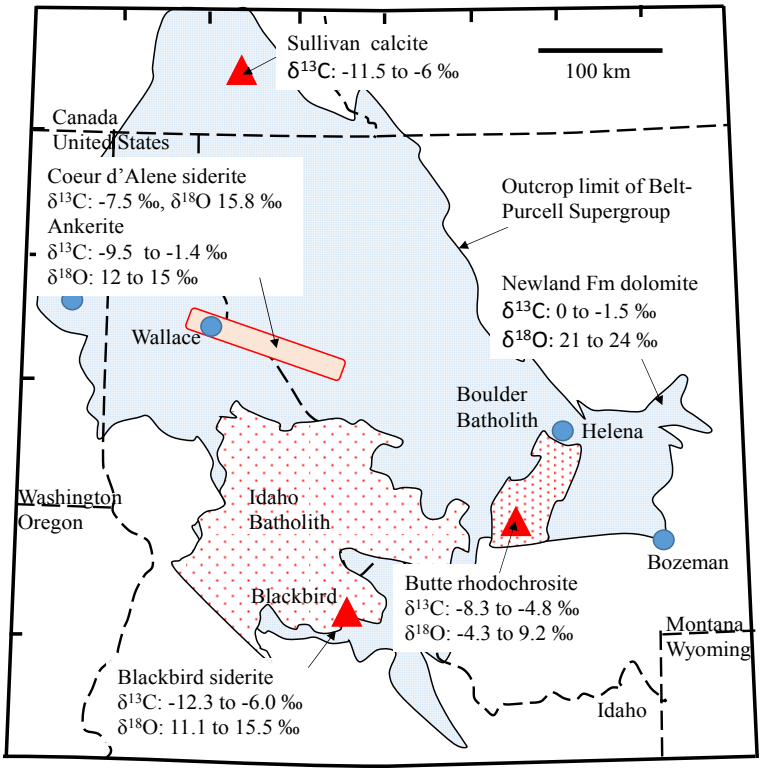

Figure 32: Carbon-oxygen isotope range from the Sullivan mine, Coeur d'Alene mining district, Newland Fm, Blackbird mine, and Butte Cu-porphyry. The pale blue region delineates the outcrop limit of the Belt-Purcell Supergroup. The textured bodies correspond to the Boulder and Idaho batholiths. Major cities are shown by blue circles. Red triangles represent mines, and in the case of Butte, the district. Data for Newland Fm. dolomite are from White (2012); Butte rhodochrosite from Stevenson (2015); Blackbird siderite from Johnson et al. (2012); Sullivan calcite from Taylor (2004).

5. Conclusions and Recommendations

5.1. Conclusions

- The mineralized veins at Emery were emplaced in the lower, basaltic andesite member of the late Cretaceous Elkhorn Mountain Volcanics, at an estimated depth of roughly 4 km, in low-angle "bedding plane" and near-vertical, east-west trending veins.
- Sulfide minerals in the Emery district include pyrite, arsenopyrite, galena, boulangerite, sphalerite (X_{FeS} = 0.06 to 0.12), chalcopyrite, Ag-rich tetrahedrite, and electrum (X_{Au} = 0.56 to 0.58). Pyrite and arsenopyrite are the most abundant, and precipitated early (Stage 1). The other ore minerals formed at essentially the same time (Stage 2). Electron microprobe data, combined with previous work, suggests that some of the early pyrite and arsenopyrite contains significant amounts of gold.
- Gangue minerals in the mineralized veins are mostly quartz and carbonate minerals (calcite, Fe-bearing dolomite, kutnohorite, ankerite).
- There are five styles of alteration in the Emery district: silicic, sericitic, propylitic, argillic, and carbonate. Silicification is found closest to the veins and grades outwards to sericitic alteration, characterized by muscovite, phengite, quartz, and pyrite. Propylitic alteration is pervasive throughout the entire mining district and includes alteration of volcanic phenocrysts to epidote/clinozoisite, zoisite, chlorite, and kaolinite. Argillic alteration is intermediate between sericitic and propylitic alteration and is characterized by montmorillonite and K-illite. Carbonate alteration ranges from small patches of carbonate minerals in the groundmass to large carbonate bodies or breccias. The alteration mineral assemblages indicate the altering fluid began slightly acidic and became increasingly more neutral with distance away from the veins.

- Fluid inclusions fell into carbonic (CO_2-rich) or aqueous (H_2O-rich) categories. The carbonic inclusions are interpreted to belong to Stage 1, and homogenized at 280 to 353°C. Stage 2 and Stage 3 aqueous inclusions homogenized between 220 to 280°C, and 127 to 220°C, respectively.
- Stage 1 carbonic fluid inclusions had relatively low salinity based on clathrate melting temperatures, although the salinity values should be considered minimum estimates due to the possible presence of mixed CO_2-CH_4 clathrates. Many carbonic inclusions contained dawsonite daughter minerals. Stage 2 aqueous fluid inclusions had salinities that clustered between 5 and 8 wt% $NaCl_{eq}$. Based on the abundance of CO_2-rich inclusions and moderate salinity values, the ore-forming fluid was most likely of magmatic origin.
- Thermodynamic calculations based on CO_2-phase behavior suggest that Stage 1 carbonic inclusions were trapped at pressures of 1.2 to 1.7 kbars. The higher range of these estimates exceeds the maximum lithostatic pressure based on the total thickness of the Elkhorn Mountain Volcanics (1.3 kbar). A fluid pressure greater than lithostatic pressure helps to explain opening of low-angle, dilational veins.
- S-isotope geothermometry based on $\delta^{34}S$ of coexisting sphalerite and galena gives temperature estimates (323 ± 73 °C) that are slightly higher but overlap with the Stage 2 fluid inclusion homogenization temperatures. After applying a pressure correction of 1.3 kbar to the fluid inclusion data, the two sets of temperature estimates are in very good agreement.

- Temperature estimates based on compositions of arsenopyrite, sphalerite, and electrum, as well as Na/K ratios of bulk fluid inclusion leachate samples, are in good agreement with the fluid inclusion and S-isotope temperature estimates.
- The $\delta^{34}S$ values of sulfide minerals from Emery range from +1.0 to +8.8 ‰ (VDCT). It is possible that the hydrothermal fluid became enriched in ^{34}S by assimilation of Belt metasediments into the parent magma, as has been proposed for the polymetallic veins of Butte.
- The $\delta^{13}C$ values of carbonate minerals from Emery range from -7.2 ‰ to -1 ‰ (VPDB). These values are slightly enriched in ^{13}C compared to typical "magmatic CO_2" values. One possible reason would be assimilation of Belt carbonate sediments which have $\delta^{13}C$ of +1 to +2 ‰.
- Carbonate minerals from Emery have a wide O-isotope range of + 3.2 to +16.8 ‰ (VSMOW). Furthermore, a negative correlation is shown when $\delta^{13}C$ is plotted vs. $\delta^{18}O$ of the carbonates. One possible explanation for the negative trend would be mixing of a hot, CO_2-rich magmatic water with a cool, CO_2-poor meteoric water. It is also possible that some of the O-isotopes of the carbonates were reset by circulation of late groundwaters.
- The veins of the Emery district most likely formed from magmatic fluids sourced from a deep-seated intrusion, possibly the same or similar age as the Boulder Batholith. The veins formed at considerable depth (> 4 km) and therefore are deep epithermal or mesothermal in origin.

5.2. Recommendations

Exploration in the district should use a combination of modern handheld NIR and XRF technology. Using the PANalytical TerraSpec Halo, trends in ISM scalar values may help delineate transitions from lower to higher temperature hydrothermal alteration. The Niton pXRF allows for quick analysis of metal concentrations in the veins and altered wallrock.

More fluid inclusion work could be done on the CO_2-rich fluid inclusions to understand the negative salinity based on clathrate melting temperatures. It is probable that these inclusions contain a mixture of CO_2 and CH_4. It may be possible to constrain CO_2/CH_4 ratios in the fluid inclusions using Raman spectroscopy. Knowing the CO_2/CH_4 ratios, it would then be possible to estimate the true salinity of the carbonic inclusions based on published thermodynamic data for mixed CO_2-CH_4 clathrates.

To further elucidate the origin of the ore-forming fluids at Emery, it might be useful to obtain $\delta^{18}O$ values from vein quartz, as well as δD values of fluid inclusions in quartz. Also, Pb-isotopes could be used to help understand the source of Pb in the deposit.

LA-ICP-MS studies could be used to obtain more accurate estimates of trace metal (e.g., gold) compositions in the various ore minerals. LA-ICP-MS could also provide data on solute composition of the fluid inclusions to understand fluid chemistry at discrete timings throughout the paragenesis.

6. References Cited

Al-Khirbash, S. (1982). Geology and mineral deposits of the Emery Mining District, Powell County, Montana. M.S. Thesis. Missoula, Montana: University of Montana. 78 p.

ASD (2016) http://www.asdi.com/ASDSite/files/ba/ba7ada5b-15f2-42de-872a-8c354cc5941c.pdf

Bakker, R.J. (1997) Clathrates: Computer programs to calculate fluid inclusion V-X properties using clathrate melting temperatures. *Computers and Geosciences*, v. 23, 1-18.

Barton Jr., P. B. and Skinner, B. J. (1979). Sulfide Mineral Stabilities *in* Geochemistry of Hydrothermal Ore Deposits (2nd ed.). Barnes, H. L. (Ed.). New York: John Wiley & Sons, Inc. 278-403.

Beaudoin, G & Therrien, P. (2009) The updated web stable isotope fractionation calculator. *In*: Handbook of stable isotope analytical techniques, Volume-II. De Groot, P.A. (ed.). Elsevier: 1120-1122.

Becraft, G. E., Pinckney, D. M., and Rosenblum, S. (1963). Geology and mineral deposits of the Jefferson City Quadrangle, Jefferson and Lewis and Clark Counties, Montana. *U.S. Geological Survey Professional Paper 428*, p. 70, 84.

Berger, B. R., Hildenbrand, T.G., O'Neill, J. M. (2011). Control of Precambrian basement deformation zones on emplacement of the Laramide Boulder Batholith and Butte mining district, Montana, United States: U.S. Geological Survey Scientific Investigations Report 2011-5016, 29 p.

Bodnar, R. J. and Vityk, M. O. (1994). Interpretation of microthermometric data for H_2O-NaCl fluid inclusions, *in* Fluid Inclusions in Minerals, Methods and Applications, B. De Vivo and M. L. Frezzotti, eds., Virginia Tech, Blacksburg, Virginia, 117-130.

Brown, P. E. and Lamb, W. M. (1989). P-V-T properties of fluids in the H_2O-CO_2-NaCl: New graphical presentation and implications for fluid inclusion studies. *Geochimica et Cosmochimica Acta*, v. 53, 1209-1221.

Callaway, H. M. (1950). Mineralization of the Bonanza Mine. M.S. Thesis, Montana Tech, Butte, Montana.

Corbett G., Leach T. (1997) Southwest Pacific Rim gold-copper systems: Structure, alteration and mineralization. Short Course Manual.

Coveney, R.M., and Kelly, W. C. (1971). Dawsonite as a daughter mineral in hydrothermal fluid inclusions. *Contr. Mineral. and Petrol*.,v. 32, 334-342.

CPI Inflation Calculator. (2016). Retrieved January 14, 2016, from U.S. Bureau of Labor Statistics: http://www.bls.gov/data/inflation_calculator.htm.

du Bray, E. A., Aleinikoff, J. N., Lund, K. (2012). Synthesis of petrographic, geochemical, and isotopic data for the Boulder Batholith, southwest Montana. U.S. Geological Survey Professional Paper 1793. 39 p.

Darling, R. S. (1991). An extended equation to calculate NaCl contents from final clathrate melting temperatures in H_2O-CO_2-NaCl fluid inclusions: Implications for P-T isochore locations. *Geochimica et Cosmochimica Acta*, v. 55, 3869-3871.

Ding, T., Zhang, C., Wan, D., Liu, Z. and Zhang, G. (2003). An experimental calibration on the sphalerite-galena sulfur isotope geothermometer. *Acta Geologica Sinica*, v 77, no 4, 519-521.

Dong, G., Morrison, G., and Jaireth, S. (1995). Quartz textures in epithermal veins, Queensland-Classification, origin, and implication. *Economic Geology*, v. 90, 1841-1856.

Eaton, G. F., Criss, R. E., Fleck, R. J., Bond, W. D., Cleland, R. W., Wavra, C. S. (1995). Oxygen, carbon, and strontium isotope geochemistry of Coeur d'Alene mining district, Idaho. *Economic Geology*, v. 90, 2274-2286.

Elliott, H. C. (1939). The Emery Mine, Powell County, Montana. M.S. Thesis, Montana Tech, Butte, Montana, 45 p.

Field, C. W., Zhang, L., Dilles, J. H., Rye, R. O., and Reed, M. H. (2005). Sulfur and oxygen isotopic record in sulfate and sulfide minerals of early, deep, pre-Main Stage porphyry Cu-Mo and late Main Stage base-metal mineral deposits, Butte district, Montana. *Chemical Geology*. v. 215, 61-93.

Fournier, R. O. and Truesdell, A. H. (1973). An empirical Na-K-Ca geothermometer for natural waters. *Geochimica et Cosmochimica Acta*, v. 37, 1255-1275.

Fournier, R. O. and Potter II, R. W. (1979). Magnesium correction to the Na-K-Ca chemical geothermometer. *Geochimica et Cosmochimica Acta*, v. 43, 1543-1550.

Gammons, C. H. and Williams-Jones, A. E. (1995). Hydrothermal geochemistry of electrum: Thermodynamic constraints. *Economic Geology*, v. 90, 420-432.

Gunnarsson, I. and Arnórsson, S. (2000). Amorphous silica and the thermodynamic properties of $H_4SiO_4°$ in the range of 0°C to 350 °C at P_{sat}. *Geochimica et Cosmochimica Acta*, v. 64, 2295-2307.

Hall, S. M. and Veizer, J. (1996) Geochemistry of Precambrian carbonates: VII. Belt Supergroup, Montana and Idaho, USA. *Geochimica et Cosmochimica Acta*, v. 60, 667-677.

Heinrich, C. A and Eadington, P. J. (1986). Thermodynamic predictions of the hydrothermal chemistry of arsenic, and their significance for the paragenetic sequence of some cassiterite-arsenopyrite-base metal sulfide deposits. *Economic Geology*, v. 81, no. 3, 511-529.

Mindat.org. (2016) Boulangerite: Hudson Institute of Mineralogy: http://www.mindat.org/min-738.html (May 2016).

Johnson C.A., Bookstrom A.A., Slack J.F. (2012) Sulfur, carbon, hydrogen, and oxygen isotope geochemistry of the Idaho Cobalt Belt. *Economic Geology*, v. 107, 1207-1221.

Joyce, J. P. (1951). A microscopic study of the ore minerals of the northern part of the Zosell (Emery) mining district. B.S. Thesis. Butte, Montana: Montana Tech. 35 p.

Korzeb, S., Scarberry, K., Zimmerman, J. L., Gammons, C. (2015). New interpretation of vein genesis for the Emery mining district, Powell County, Montana. *Geological Society of America, Abstracts with Programs*, v. 47(7), p. 244.

Korzeb, S., Scarberry, K.C., Zimmerman, J.L., Gammons, C., 2016, New models of exploration potential within the Boulder Batholith, southwest, Montana: *SME Annual Meeting*, Phoenix, AZ, 2016.

Kretschmar, U. and Scott, S. D. (1976). Phase relations involving arsenopyrite in the system Fe-As-S and their application. *Canadian Mineralogist*, v. 14, 364-384.

McCrea, J. M. (1950). On the isotopic chemistry of carbonates and a paleotemperature scale. *The Journal of Chemical Physics*, v. 18, no. 6, 849-857.

Moëlo, Y., Makovicky, E., Mozgova, N. N., Jambor, J. L., Cook, N., Pring, A., Paar, W., Nickel, E. H., Graeser, S., Karup-Møller, S., Balic-Žunic, T., Mumme, W. G., Vurro, F., Topa, D., Bindi, L., Bente, K., and Shimizu, M. (2008). Sulfosalt systematics: a review. Report of the sulfosalt sub-committee of the IMA Commission on Ore Mineralogy. *European Journal of Mineralogy*, v. 20, 7-46.

Obolensky, A. A., Gushchina, L. V., Borisenko, A. S., Borovikov, A. A., and Pavlova, G. G. (2007). Antimony in hydrothermal processes: solubility, conditions of transfer, and metal-bearing capacity of solutions. *Russian Geology and Geophysics*, *48*(12), 992-1001.

Ohmoto, H. (1972). Systematics of sulfur and carbon isotopes in hydrothermal ore deposits. *Economic Geology*, v. 67, 551-578.

Ohmoto, H., and Rye, R.O. (1979) Isotopes of sulfur and carbon. Chapter 10 in Barnes, H.L. ed. Geochemistry of Hydrothermal Ore Deposits, 2nd ed., Wiley Intersciences, 509-567.

Palmer, D. A., Hyde, K. E. (1993). An experimental determination of ferrous chloride and acetate complexation in aqueous solutions to 300C. *Geochimica et Cosmochimica Acta*, v. 57, 1393-1408.

Pokrovski, G. S., Borisova, A. Y., Roux, J., Hazemann, J. L., Petdang, A., Tella, M., and Testemale, D. (2006). Antimony speciation in saline hydrothermal fluids: A combined X-ray absorption fine structure spectroscopy and solubility study. *Geochimica et Cosmochimica Acta*, *70*, 4196-4214.

Reed, M. H., and Palandri, J. (2006). Sulfide mineral precipitation from hydrothermal fluids. *Reviews in Mineralogy and Geochemistry*, v. 61, 609-631.

Robertson, F. (1953). Geology and mineral deposits of the Zosell (Emery) Mining District, Powell County, Montana. (Memoir 34), 29. Butte, Montana: Montana Bureau of Mines and Geology. 35 p.

Roedder, E. (1984). Interpreataion and utilization of inclusion measurements: Compositional data on liquid and gas inclusions *in* Fluid Inclusions. Reviews in Mineralogy, v. 12. Ribbe, P. H. (Ed.). BookCrafters, Inc. Chelsea, MI. 222-250.

Rosenberg, P. E. and Larson, P. B. (2000). Isotope geochemistry of ankerite-bearing veins associated with the Coeur d'Alene mining district, Idaho. *Economic Geology*, v. 95, 1689-1699.

Scarberry, K.C., 2015, Vent deposits within the Late Cretaceous Elkhorn Mountains Volcanics of southwestern Montana, in Inaugural Mining and Mineral Symposium, Butte, Montana: Montana Bureau of Mines and Geology Open-File Report 669.

Shankar, V. (2015) Field characterization by near infrared (NIR) mineral identifiers – A new prospecting approach. *Procedia Earth and Planetary Science*, v. 11, 198-203.

Sharp, Z. D., Essene, E. J., & Kelly, W. C. (1985) A re-examination of the arsenopyrite geothermometer: pressure considerations and applications to natural assemblages. *Canadian Mineralogist*, v. 23, 517-534.

Smedes, H.W. (1966). Geology and igneous petrology of the Northern Elkhorn Mountains Jefferson and Broadwater Counties, Montana. U.S. Geological Survey Bulletin 510, 82 p, 1:48,000-scale map.

Stejer, F. A. (1948). The geology and ore deposition of the Bonanza Mine, Emery (Zosel) Mining District, Powell County, Montana. M.S. Thesis. Butte, Montana: Montana Tech. 39 p.

Stevenson, R. (2015). Stable isotopes of hydrothermal carbonate minerals in the Butte porphyry-lode deposits, Montana. M.S. Thesis. Montana Tech, Butte, MT, 84 p.

Taylor, B.E. (2004). Biogenic and thermogenic sulfate reduction in the Sullivan Pb-Zn-Ag deposit, British Columbia (Canada): Evidence from micro-isotopic analysis of carbonate and sulfide in bedded ores. *Chemical Geology*, v 204, 215-236.

Taylor, H.P. Jr. (1979) Oxygen and hydrogen isotope relationships in hydrothermal mineral deposits. Chapter 6 in Barnes, H.L. ed. Geochemistry of Hydrothermal Ore Deposits, 2nd ed., Wiley Intersciences, 236-277.

van den Kerkhof, A. M. (2011). Fluid inclusions: Petrography and genetic interpretation of fluid inclusions. Geowissenschaftliches Zentrum der Universität, short course, http://www.uni-goettingen.de/de/26174.html (February 2015).

Watson, S.M. (1986). The Boulder Batholith as a source for the Elkhorn Mountains Volcanics, southeast quarter of the Deer Lodge 15' quadrangle, southwestern Montana: Missoula, University of Montana, M.S. Thesis, 100 p., 1:24,000-scale map

White, J. (2012). Paragenesis of cobalt and nickel at the Black Butte copper project, Meagher County, Montana. M.S. Thesis. Montana Tech, Butte, Montana, 73 p.

Wilkinson, J. J (2001). Fluid inclusions in hydrothermal ore deposits. *Lithos*, v 55, 229-272.

Wischnewski, B. Calculation of thermodynamic state variables of carbon dioxide at saturation state, boiling curve. peace software: http://www.peacesoftware.de/einigewerte/co2_e.html (April 2016).

Appendix A: Tables

Sample No. (collected by author)	Sample No. (collected by S. Korzeb)	Mine
Em, C 14, E	E-1, 32-38, 40-42	Upper Emery
	E-70-72	Lower Emery
A	E-15-21, 23	Argus
P, C9	E-54-65	Paymaster
ED	E-2, 4-6, 8-10	Emma Darling
HHand	E-22, 66-69	Upper Hidden Hand
	E-12-14	Lower Hidden Hand
B	E-28-31	Bonanza
	E-3, 7, 45	Blue Eyed Maggie
	E-11, 44	Sterret
	E-24, 27	Elizabeth
	E-39	St. Mary's
	E-43	Bull Moose
	E-46-50	Monday
	E-51-53	Wednesday
	E-25-26	granodiorite

Table A 1: Fluid inclusion data. Note all temperature in (°C). Highlighted temperatures may be unreliable and were not used in calculations.

E70H2a Emery			Tm_{ice}			V vol	Type	Th	
1	-4.7	-4.7	-4.5			30	1	255	
2	-4.4	-4.5	-4.4						
3	-4.3	-4.2	-4.7	-4.5		30	1	251	
4	-4.9	-4.8	-4.9			10	1	258	
5		-4.6	-4.5	-4.8		10	1	254	
6	-4.3	-4.4	-4.4						
7		-2.6	-5.2	-5.2	-5.3				
8	-5.6	-5.4	-5.2			50			
9		-4.0	-4.2	-4.2		10	1	259	
10						20	1	262	dark
11						20	1	278	dark
12						20	1	263	
13						20	1	238	dark
14						20	1	262	
15						20	1	260	
16						20	1	239	
17						30	1	261	
18						20	1	257	
19						20	1	254	
20						50			
21						30	1	285	dark
22						20	1	283	
23						10	1	164	
24						30	1	261	
25						20	1	264	
26						20	1	230	
27						30	1	264	
28						20	1	241	

	29					10		1	261	
	30					30		1	261	
chip 2										
	1					40				
	2	-3	-2.8	-3.5	-3.3	10		1	176	
		couldn't see ice crystals								
	3	melt				30		1	288	
	4	-3.3	-3.3	-3.2		20		1	190	
	5	missed	-4.9	-4.9	-5	30		1	289	
	6	-6.1	-3.1	-3.2	-3.2	10		1	197	
	7	missed	-3.9	-4.4	-4	20		1	230	
	8	-3.2	-3	-2.6	-2.8	20				
	9					70		1	292	lightened at 230
	10	-2.6	-2.8	-3.1		30				dark on freezing
	11	-3	-2.4	-3	-2.7	20				
	12					20		1	290	
	13					20		1	283	
	14					20		1	237	
	15					20		1	196	
	16					10		1	137	no return bubble
	17					10		1	194	
	18					50	1a		284	and Tmhalite
	19					10		1	190	
	20					20		1	290	anealed fracture
	21					20		1	298	
	22					20		1	288	

Hidden Hand	$Th_{CO2 \rightarrow l}$				$Tm_{CO2 \rightarrow l}$		Tm_{clath}	Tm_{ice}				Type	
1	28.83	28.6	29	28.9	-58.5	-55.8	11.5						
2	29.50	29.5			-56.7		11.2						
3	28.03	27.5	28.3	28.3	-56.1		11.2						
4	28.53	28.5	28.6	28.5			11.6						
5	28.37	28.4	28.4	28.3	-56.1		11.2						
6								-4.5	-4.1	-3.9	-4.2	1	284.8
7								-3	-4.1	-2.4	-3	1	282.2
8								-4.7	-4.7	-4.7		1	335.9
9								-4.7	-4.7	-4.6		1	335.9
10								-4.8	-4.7	-4.1	-4.6	1	332
11								-5.5				1	339.3
11b								-4.8				1	347.7
12												1	342.5
13							7.4	-3.5				3	341.1
14							2.3	-5.7				3	337.1
15												1	327.5
15b							5.4	-4					
16								-4.7				1	341.8
17a-c	27.5												

Hidden Hand 2	Th_{CO2}		Tm clath				Tm ice					Type	Th	
1			11	10.5	11		-4.9	-4.2	-2.9	-4.1				dark
2			12.7	10.3	10.7	10.5	-4.2	-4.7	-4.5	-4.3		3	293.1	
3			10.7	12	10.8	11.3	-4.6	-4.7	-4.8			3	317.6	2x bubble forms in H_2O and goes into CO_2 around -1 to 1
4							-4.6	-4.2	-4.5			1	296.4	
5			9.7	9.4	9.7	9.6	-7.3	-7.2	-6.2	-4.6	-6.2	4	306.3	uncertain about range
6							-4.7	-4.6				1	286.7	creates bubble around +13
7							-5.6	-5.3				1	292.6	
8	30.7		10	10	9.7							3	317.9	
9	19.2	19.7	10	11.8	10.4	10.4	-3.3	-3.4	-3.3			3	298.9	
10												1	316.2	
11												1	327.5	
12			9.7				-3.3	-0.4	-0.3	-1.2	-0.3	3	189.2	
13			11.3	11.5	11.4								empty	
14												1	289.3	
15							-3.5	-3.6				1	276.8	
16							-4.1	-3.5	-3.1	-3.1		1	283.9	

E-3a Blue-Eyed Maggie

		Tm ice					Type	Th	
1	-4.2	-4.3	-4.2					204.7	
2	-4.6	4.6	4.5					236.4	
3	-4.4	4.5	1.6	-4.5	-4.1	-2.3		209.2	unsure about scatter, kept refreezing to get to low numbers
4	-1	-1.7	-1.8	-2				streched	
5	-4.1	-3.9	-3.5	-3.3	-4	-3.5		171.8	unsure about scatter, kept refreezing to get to low numbers
6	-3.3	-3.5	-3.3					186.7	
7	-2.5	-3	-2.6	-3.3	-2.7			190.1	unsure about scatter, kept refreezing to get to low numbers
8		-3.2	-3.3	-2.6	-2.6	-2.6		169	
9		-3.6	-3.1	-3.7	-3.6			197.1	
10		-1.8	-1.7	-1.9				127.4	bubble disappears on freezing reappears ~-5°

E61

Paymaster	Th_{CO2} →v		Tm ice				Type		Th	
1			-2.4				4a		314.6	
2			0.4	1.2	0.7	0.2	1b		303.4	l→v
3			0							
4									313	
5	28.7		-4.5	-4.2	-4.3		4a			
6	28.2		-3.6	-4	-4.3	-3.2	4a		313.1	
7			-5.2	-4.2	-4.8			4	313.1	
8	25.7	30						4	313.1	
9	25.7		-0.2				4a		317.1	
10	24		-5.4	-5.8	-5.8		4a		313.5	
11							4a		330.2	
12								4	322.7	
13							4a		214.8	

E27 Elizabeth			Tm ice			Type	Th	Comments
1	-4.5	-4.5	-4.3			1	308.9	
2	-3.8	-3.8	-4			1	281.5	
3								
4	-4.4	-4.2	-4.2					
5						1	170	
6								
7	-4.2	-4.4	-4.1					
8	-4.2	-4	-4					
9	-5.3	-4.4	-4.9	-5	-4.9	1	307.1	
10	-5.7	-4.9	-4.7			1	314.7	
11						1	309.9	
12	-4.2	-4.4	-4.4			1	184.7	
13								
14	-2.3	-3.6	-3.4					clath present but too small
15	-4.4	-4.2	-4.4					
16	-4.2	-4.7	-4.6			1	203.9	
17	-4.4	-4.5				1	277.2	

E23 Argus	Tm ice					Type	Th
1	-4.7	-3.8	-4.5	-4.5	-4.4	1	238.8
2							
3	-3.2	-3.1	-3.2			1	132
4						1	252
5	-3	-3.2	-3.2				
6	-3.6	-4.6	-4.5	-4.4	-4.4	1	240.7
7	-3.3	-3.2	-3.3			1	234.1
8	-2.7	-3	-2.8			1	214.8
9	-3.4	-3.2	-3.5			1	204.5
10						1	205.1
11	-3.4	-3.5	-3.3			1	189.4
						1	198.5

E-8 Emma Darling vein	Tm ice			Type	Th	Td
1						215
2	-4.2	-4.2		1	188.5	
3	-4.8	-5.1	-5.2	1	170.9	
4	-4.9	-4.8		1	196.3	
5	-3.2					
6	0			1	353.7	

Emery vein section	Tm_{ice}			Type	Th	Comments
	-7.2	-7.3				
	-3.4	-3.3	-3.1			
	-3.9	-4	-3.9	1	324.3	nucleates 2nd bubble if short on Th
				1	314.7	
				1	317.4	
				1	308.8	
				1	205.2	
				1	319.2	
				1	319.2	
				1	319.2	
				1	222.7	
				1	193.2	
				1	306.8	
				1	322.1	
				1	300	
				1	219.2	
				1	314.7	
				1	316.9	
				1	338.5	
				1	276.3	
				1	322.5	
	-3.4	-3.3				

Hidden Hand	Tm_{CO2}		Tm_{ice}	Tm_{clath}	Th_{CO2} (→ l)			Type	Th	Td
1	-56.4			11.2	27.5	27.4		2	245	
2				10.9	29.8					
3				10.3	28.4			2		283.8
4	-56.4			10.9	28.2	27.9	28.2	2	301.9	
5				11	29.4					
6	-58.7			11.2	28.2			2	301.9	
7				11.2	28.2	28.3		2	301.9	
8		-4.3	-4.2					1	245.8	
9				11.2	27.8	27.7				
10				11.2	27.1					
11		-4.6						1	247	

Table A 2: Halo results

Sample	Mineral	Stars	Scalar									
			AlOH	Kx	ISM	CSM	MgOH	Fe3t	Fe3i	FeOH	AlFeMg	Comment
KCS-13-24 (South of district)	Mg-illite	2	2205.1	0.999	1.148	3.172	2332.7			2245.5	2205.1	
	FeMgChlorite	2										
	KaoliniteWX	1										
	Zoisite	1										
KCS-13-22 (South of district)	Calcite	3	INV		1.082		2338.1			INV	2338.1	
	Vermiculite	2										
	FeMgChlorite	1										
	Mg-illite	1										
KCS-13-22	Siderite	3										
E11	Ferrihydrite	3										
	Calcite	3										
	Dolomite	3										
E11	Ferrihydrite	3	2205.4		1.182			933	2.721		2339.6	
	Kutnohorite	2										
	Mg-illite	1										
	Calcite	1										
E66	K-illite	3	2208.2	1.043	0.963		2350.4				2208.2	
	KaolinitePX	3										
E66	K-illite	3	2208.2	1.038	1.003		2350.4				2208.2	
	KaolinitePX	3										
E26	Muscovite	3	2205.5		0.638		2348.2				2205.5	
	Mg-illite	3										
	Pyrophyllite	2										
E26	Muscovite	3	2206		0.635		2348.3				2206	
	K-illite	3										
E16	Ferrihydrite	2	2202.8		1.085		2345.1	970.8	1.543		2202.9	
	K-illite	2										
	Wavellite	1										

Sample	Mineral	Stars	AlOH	Kx	ISM	CSM	MgOH	Fe3t	Fe3i	FeOH	AlFeMg	Comment
	Jarosite	1										
E16	K-illite	3	2202.9		0.964		2346.5				2202.9	
E43	Ferrihydrite	3	2207.3		1.048		2349	964.8	1.289		2207.3	
	K-illite	3										
	Montmorillonite	3										
	Goethite	1										
E43	Ferrihydrite	3	2207.2		1.033		2348.4				2207.2	
	K-illite	3										
	Sepiolite	3										
	Montmorillonite	2										
E9	Dolomite	3										
E9	Dolomite	3										
E69	FeMgChlorite	2	2208.8	1.041	0.93	2.481	2343			2253.1	2343	
	K-illite	2										
	Halloysite	1										
E69	FeMgChlorite	3	INV	1.067	0.844	2.243	2341.4			2253.4	2341.4	
	K-illite	2										
	Mg-chlorite	1										
	Halloysite	1										
E68	K-illite	3	2208.7		0.731	INV	2343.3			INV	2208.7	
	Mg-chlorite	3										
E68	K-illite	3	2209.3		0.751		2346.7				2209.3	
E25	Mg-illite	3	2208.4	1.044	0.913		2346.8				2346.8	
	Clinozoisite	2										
	KaoliniteWX	1										
E25	Mg-illite	3	2207.5	1.04	0.962	2.702	2347.1			2251	2347.1	
	Clinozoisite	2										
	KaoliniteWX	2										
	FeMgChlorite	1										
E53	K-illite	3	2201.8		0.781		2342.4				2201.8	

Sample	Mineral	Stars	AlOH	Kx	ISM	CSM	MgOH	Fe3t	Fe3i	FeOH	AlFeMg	Comment
	Ankerite	3										
E53	K-illite		2201.9		0.843		2342.2				2201.9	
	Ankerite											
E48	Ferrihydrite	3	2207		0.839		2348.1	INV	1.352		2207	
	Muscovite	3										
	Mg-illite	3										
	Goethite	3										
E48	Muscovite	3	2205.3		0.861		2347.8				2205.3	
E4	K-illite	3	2206.9		0.643		2346.9				2206.9	
E4	K-illite	3	2207.5		0.679		2346.8				2207.5	
E7	K-illite	3	2207.9		0.629		2347.6				2207.9	
E7	Phengite	3	2208.6		0.624	INV	2347.4					
	Rectorite	3										
	Glaucophane	2										
E7	K-illite	3	2207.9		0.633		2347.7				2207.9	
E65	K-illite	3	2202.6		0.802		2345				2202.6	
E65	K-illite	3	2202		0.89		2343.3				2202	
	Ankerite	3										
E65	K-illite	3	2202.5		0.773		2345				2202.2	
	Phengite	3										
E57	Dolomite	3	2323.4							INV	2323.4	
	Ankerite	3										
	Fe-saponite	2										
E57	K-illite	3	2200.9		1.016		2335.1				2200.9	
	Dolomite	3										
ED-15	Dolomite	3										
ED-15	Dolomite											
ED-3	Muscovite	3	2206.1		0.873		2348.2				2206.1	
	Mg-illite	3										
ED-3	Muscovite	3	2208.5		0.994		2348.1				2208.5	

Sample	Mineral	Stars	AlOH	Kx	ISM	CSM	MgOH	Fe3t	Fe3i	FeOH	AlFeMg	Comment
	Mg-illite	3										
ED-11	K-illite	3	2205.5		0.677		2346.6				2205.5	
ED-11	Muscovite	3	2208.2		0.701		2347.8				2208.2	
ED-13	K-illite	3	2208.3		0.673		2345.3				2208.3	
ED-13	K-illite	3	2208.2		0.612		2347.6				2208.2	
ED-8	FeMgChlorite	3	INV	1.019	0.928	2.423	2336.7			INV	2336.7	
	K-illite	2										
	Phlogopite	1										
	Halloysite	1										
ED-8	Biotite	2	2208.7		0.942		2335.9				2335.9	
	K-illite	1										
	Calcite	1										
ED-14	Halloysite	2	2207.4	1.016	0.998		2330.8			INV	2330.8	
	Hornblende	2										
	Mg-illite	1										
ED-14	Hornblende	3	2206.4	1.005			2328.2			INV	2328.2	
	Phlogopite	2										
	Halloysite	1										
ED-12	Biotite	3	INV				2334.9			INV	2334.9	
	Hornblende	3										
ED-12	Biotite	3	INV				2333.8			INV	2333.8	
	Hornblende	3										
ED-9	K-illite	3	2207.1		0.701		2346.2				2207.1	
ED-9	K-illite	3	2208.3		0.656		2347.7				2208.3	
Em-34	K-illite	3	2204.6		0.804		2347.7				2204.6	
Em-34	K-illite	3	2204.2		0.953		2347.5				2204.2	
Em-31	FeMgChlorite	3	INV	1.005	0.989	2.627	2334.8			2250.2	2334.8	
	Mg-illite	2										
	KaoliniteWX	1										
	FeChlorite	1										

Sample	Mineral	Stars	AlOH	Kx	ISM	CSM	MgOH	Fe3t	Fe3i	FeOH	AlFeMg	Comment
Em-31	FeMgChlorite	3	INV	1.006	1.003	2.669	2333.9			INV	2333.9	
	Mg-illite	2										
	KaoliniteWX	1										
	FeChlorite	1										
Em-33	K-illite	3	2198		0.973		2333.3				2198	
	Dolomite	3										
Em-33	K-illite	3	2201.3		0.779		2344.7				2201.3	
	Dolomite	3										
Em-39	Stilpnomelane	3	INV		1.084	2.893	2343.6			INV	2343.6	brown-green
	FeMgChlorite	2										
	NH3_I/S	1										
	Calcite	1										
Em-39	Siderite	3	INV		1.159		2340.9				2340.9	green silica
	Biotite	1										
	Diaspore	1										
	Mg-illite	1										
Em-39	Epidote	2	INV	1.027	0.987		2339.5			INV	2339.5	light green
	Mg-illite	2										
	Roscoelite	1										
	Halloysite	1										
Em-37	Mg-illite	2	2009.4	1.025	0.972	2.565	2345.9			2252.8	2345.9	
	FeMgChlorite	2										
	KaoliniteWX	1										
Em-37	FeMgChlorite	2	2210.1		0.932	2.457	2346.9			2252.8	2346.9	
	Phengite	2										
	Mg-illite	1										
	Montmorillonite	1										
Em-38	FeMgChlorite	3	INV			2.805	2342.7			INV	2342.7	
	Montmorillonite	2										

Sample	Mineral	Stars	AlOH	Kx	ISM	CSM	MgOH	Fe3t	Fe3i	FeOH	AlFeMg	Comment
	Epidote	1										
Em-38	FeMgChlorite	3	INV		1.055	2.801	2340.1			INV	2340.1	
	Iron Saponite	3										
	Mg-illite	2										
Em-40	Phengite	3	2213.3		0.87	2.44	2345.5			2250.2	2345.5	groundmass
	FeMgChlorite	3										
	Montmorillonite	1										
Em-40	K-illite	2	2213.3		0.922		2341.1				2341.1	vein
	Ankerite	2										
Em-32	K-illite	3	2204.8		0.94		2348.3				2204.5	
Em-32	K-illite	3	2204.5		0.917		2346				2204.5	
Em-23	FeMgChlorite	3	INV		1.092	2.93	2343.7			2252.8	2343.7	
	Mg-illite	2										
	Tourmaline	1										
	Hydrobiotite	1										
Em-23	FeMgChlorite	3	INV		1.073	2.875	2343.9			2254.9	2343.9	
	Mg-illite	3										
Em-29	Mg-illite	3	2215.1		0.893	2.533	2345.8			2248.5	2345.8	clast
	FeMgChlorite	3										
	Muscovite	2										
Em-29	FeMgChlorite	3	INV		1.013	0.919	2341			2253.8	2341	clast
	Mg-illite	3										
	Calcite	2										
	Halloysite	1										
Em-29	Calcite	3	INV				2337.3			INV	2337.3	matrix
	Palygorskite	3										
	Beidellite	2										
Em-28	K-illite	3	2208.5		0.771		2347.1				2208.5	
Em-28	K-illite	3	2209.5		0.783		2347.2				2209.5	
Em-28	K-illite	3	2209.5		0.897		2337.2				2209.5	

Sample	Mineral	Stars	AlOH	Kx	ISM	CSM	MgOH	Fe3t	Fe3i	FeOH	AlFeMg	Comment
	Aragonite	3										
Em-35	K-illite	3	2205.8		0.818		2346.8				2205.8	
Em-35	K-illite	3	2205.8		0.9		2347				2205.8	
Em-27	Muscovite	3	2209		0.698		2347.1				2209	
	Mg-illite	3										
Em-27	K-illite	3	2208.5		0.749		2346.3				2208.5	
Em-27	Ferrihydrite	3	2210.2		0.974		2332.8				2332.8	vein
	Dolomite	2										
	K-illite	2										
	Calcite	1										
HHand-11	K-illite	3	2007.2		0.747		2346.9				2207.2	
HHand-11	K-illite	3	2206.6		0.75		2347.1				2206.6	
HHand-10	K-illite	3	2206.7		0.742		2347.5				2206.7	
HHand-10	K-illite	3	2205.7		0.686		2347.2				2205.7	
	Muscovite	3										
HHand-9	K-illite	3	2206.4		0.809		2346.4				2206.4	
HHand-9	Jarosite	2	2205.3		0.859		2345.5	INV	1.12		2205.3	
	K-illite	3										
HHand-8	K-illite	3	2205.2		0.958		2345				2205.2	
	Beryl	3										
HHand-8	Jarosite	3	2204.2		0.974		2344.1	INV	1.297		2204.2	
	K-illite	3										
HHand-7	Jarosite	3	2202.8					884.2	1.305			joining 2 veins
HHand-7	K-illite	3	2205.9		0.772		2346.7				2205.9	
HHand-6	K-illite	3	2204.7		0.974		2345.9				2204.7	
HHand-6	Jarosite	3	2203.4		1.041		2341.9	INV	1.31		2203.4	
	K-illite	2										
HHand-2	K-illite	3	2204.5		0.853		2347.1				2204.5	
	Magnesite	3										

Sample	Mineral	Stars	AlOH	Kx	ISM	CSM	MgOH	Fe3t	Fe3i	FeOH	AlFeMg	Comment
HHand-2	K-illite	3	2204.3		0.862		2347				2204.3	
	Magnesite	3										
HHand-4	Biotite	3	INV		1.094		2336.7			INV	2336.7	
	Hornblende	2										
	Mg-illite	1										
HHand-4	Biotite	3	2206.2	1.001	1.095		2334.1			INV	2334.1	
	Hornblende	2										
	Mg-illite	1										
	Calcite	1										
P-7	Ferrihydrite	2	2207.5		1.298		2343.1				2343.1	
	Vermiculite	3										
	FeChlorite	2										
	Mg-illite	1										
P-7	Ferrihydrite	2	INV		1.267		2342.6				2342.6	
	Vermiculite	3										
	FeChlorite	2										
	Mg-illite	1										
B-8	K-illite	3	2207.3		0.617		2348.2				2207.3	
B-8	K-illite	3	2206.5		0.64		2348.1				2206.5	
B-9	Muscovite	3	2205.7		0.755		2348.7				2205.7	
	K-illite	3										
B-9	Muscovite	3	2206.5		0.687		2347.9				2206.5	
	K-illite	3										
B-6	K-illite	3	2204.3		0.641		2347.5				2204.3	
B-6	K-illite	3	2204.3		0.635		2348				2204.3	
B-7	Muscovite	3	2205.8		0.791		2344.9				2205.8	
	K-illite	3										
B-7	Muscovite	3	2205.9		0.769		2346.8				2205.9	
	K-illite	3										
B-11	Muscovite	3	2204.9		0.764		2347.3				2204.9	

Sample	Mineral	Stars	AlOH	Kx	ISM	CSM	MgOH	Fe3t	Fe3i	FeOH	AlFeMg	Comment
	Mg-illite	3										
B-11	Muscovite	3	2204.8		0.763		2347.7				2204.8	
	Mg-illite	3										
	Brucite	2										
C-14	Ferrihydrite	3	2203.3		0.758		2345.4				2203.3	
	K-illite	3										
	Ankerite	3										
	Muscovite	2										
C-14	Ferrihydrite	3	2203		0.78		2346.5				2203	
	K-illite	3										
	Phengite	3										
	Ankerite	1										
C-9	Ferrihydrite	3	2207.7	0.949			2319.2					
	KaoliniteWX	3										
	Vermiculite	3										
	Ankerite	1										
C-9	Ferrihydrite	3	2207.8	0.954			2322					
	KaoliniteWX	3										
	Ankerite	2										
	Vermiculite	1										
E	Epidote	3	INV							INV	2340	
	Montmorillonite	3										
	Calcite	2										
E	FeChlorite	1	INV		0.919		2340.1			INV	2340.1	
	Epidote	3										
	Mg-illite	3										
	FeChlorite	2										
E	Calcite	3					2337					matrix
	Sepiolite	3										

Table A 3: Sulfur isotope data

Sample No.	Mineral	Sample Description	Location	$\delta^{34}S‰$
E-1-1PY	pyrite	associated with quartz veining	Hidden Hand mine	5.4
E-2-1SP	sphalerite	massive sulfide vein in altered basalt	Emma Darling mine	4.5
E-2-1PY	pyrite	massive sulfide vein in altered basalt	Emma Darling mine	5.4
E-2-1APY	arsenopyrite	massive sulfide vein in altered basalt	Emma Darling mine	3.4
E-4-1PY	pyrite	disseminated pyrite in altered basalt	Emma Darling mine	8.7
E-5-1GL	galena	massive sulfide vein in altered basalt	Emma Darling mine	4.1
E-5-1SP	sphalerite	massive sulfide vein in altered basalt	Emma Darling mine	5.5
E-6-1PY	pyrite	coarse grained quartz with sulfide veining	Emma Darling mine	6.2
E-6-1SP	sphalerite	coarse grained quartz with sulfide veining	Emma Darling mine	4.3
E-7-1PY	pyrite	disseminated pyrite in altered basalt	Black Eyed May	8.5
E-12-1GL	galena	white quartz with disseminated sulfides	Hidden Hand mine	3.8
E-12-1PY	pyrite	white quartz with disseminated sulfides	Hidden Hand mine	6.0
E-13-1PY	pyrite	disseminated sulfides in quartz veins	Hidden Hand mine	4.4
E-13-1GL	galena	disseminated sulfides in quartz veins	Hidden Hand mine	1.7
E-14-1PY	pyrite	massive sulfide vein with quartz veining	Hidden Hand mine	4.3
E-14-1SP	sphalerite	massive sulfide vein with quartz veining	Hidden Hand mine	3.6
E-14-1GL	galena	massive sulfide vein with quartz veining	Hidden Hand mine	1.7
E-21-1PY	pyrite	disseminated sulfides in quartz veins	Argus no. 6 adit	7.1
E-21-1SP	sphalerite	disseminated sulfides in quartz veins	Argus no. 6 adit	5.6
E-21-1GL	galena	disseminated sulfides in quartz veins	Argus no. 6 adit	3.5
E-22-1PY	pyrite	quartz veins with disseminated sulfides	Hidden Hand mine	5.3
E-22-2GL	galena	quartz veins with disseminated sulfides	Hidden Hand mine	3.0
E-22-2PY	pyrite	quartz veins with disseminated sulfides	Hidden Hand mine	5.6
E-22-2AP	arsenopyrite	quartz veins with disseminated sulfides	Hidden Hand mine	5.5
E-24-1SP	sphalerite	quartz veins with disseminated sulfides	Elizabeth mine	5.6
E-24-1GL	galena	quartz veins with disseminated sulfides	Elizabeth mine	3.8
E-24-2PY	pyrite	quartz veins with disseminated sulfides	Elizabeth mine	5.3
E-24-2GL	galena	quartz veins with disseminated sulfides	Elizabeth mine	4.1
E-27-1SP	sphalerite	disseminated sulfides and quartz veins	Elizabeth mine	3.9

Sample No.	Mineral	Sample Description	Location	$\delta^{34}S‰$
E-27-1GL	galena	disseminated sulfides and quartz veins	Elizabeth mine	1.9
E-27-1PY	pyrite	disseminated sulfides and quartz veins	Elizabeth mine	4.3
E-28-1SP	sphalerite	massive sulfide vein with quartz veining	Bonanza mine	4.3
E-28-1GL	galena	massive sulfide vein with quartz veining	Bonanza mine	3.9
E-28-1PY	pyrite	massive sulfide vein with quartz veining	Bonanza mine	4.3
E-29-1AP	arsenopyrite	disseminated arsenopyrite in quartz veins	Bonanza mine	6.4
E-31-1PY	pyrite	disseminated sulfides with quartz veins	Bonanza mine	4.0
E-31-2SP	sphalerite	disseminated sulfides with quartz veins	Bonanza mine	3.5
E-31-2GL	galena	disseminated sulfides with quartz veins	Bonanza mine	1.3
E-31-3AP	arsenopyrite	disseminated sulfides with quartz veins	Bonanza mine	5.6
E-32-1Gl	galena	quartz veins and disseminated sulfides	Emery west shaft	1.1
E-32-1SP	sphalerite	quartz veins and disseminated sulfides	Emery west shaft	4.1
E-32-1AP	arsenopyrite	quartz veins and disseminated sulfides	Emery west shaft	2.0
E-32-1PY	pyrite	quartz veins and disseminated sulfides	Emery west shaft	4.8
E-32-2PY	pyrite	quartz veins and disseminated sulfides	Emery west shaft	5.1
E-32-2GL	galena	quartz veins and disseminated sulfides	Emery west shaft	1.9
E-32-2SP	sphalerite	quartz veins and disseminated sulfides	Emery west shaft	3.4
E-32-3PY	pyrite	quartz veins and disseminated sulfides	Emery west shaft	5.2
E-32-3GL	galena	quartz veins and disseminated sulfides	Emery west shaft	1.7
E-32-4PY	pyrite	quartz veins and disseminated sulfides	Emery west shaft	5.8
E-32-4AP	arsenopyrite	quartz veins and disseminated sulfides	Emery west shaft	3.8
E-33-1AP	arsenopyrite	asenopyrite crystals etched from calcite	Emery main shaft	5.7
E-33-2PY	pyrite	disseminated sulfides in quartz veins	Emery main shaft	6.3
E-33-2SP	sphalerite	disseminated sulfides in quartz veins	Emery main shaft	5.4
E-33-2AP	arsenopyrite	disseminated sulfides in quartz veins	Emery main shaft	5.6
E-37-1PY	pyrite	massive sulfides with quartz veins	Emery main shaft	6.8
E-37-1GL	galena	massive sulfides with quartz veins	Emery main shaft	1.7
E-37-1AP	arsenopyrite	massive sulfides with quartz veins	Emery main shaft	4.8
E-37-2SP	sphalerite	massive sulfides with quartz veins	Emery main shaft	4.6
E-37-3SP	sphalerite	massive sulfides with quartz veins	Emery main shaft	6.4

Sample No.	Mineral	Sample Description	Location	$\delta^{34}S‰$
E-37-3GL	galena	massive sulfides with quartz veins	Emery main shaft	2.2
E-37-3AP	arsenopyrite	massive sulfides with quartz veins	Emery main shaft	5.2
E-40-1PY	pyrite	sulfides with carbonate and quartz veins	Emery east shaft	6.4
E-40-1GL	galena	sulfides with carbonate and quartz veins	Emery east shaft	2.1
E-40-1SP	sphalerite	sulfides with carbonate and quartz veins	Emery east shaft	4.3
E-42-1PY	pyrite	sulfides in altered basalt, quartz veins	Emery east shaft	7.0
E-42-1GL	galena	sulfides in altered basalt, quartz veins	Emery east shaft	1.8
E-42-1SP	sphalerite	sulfides in altered basalt, quartz veins	Emery east shaft	4.7
E-42-2AP	arsenopyrite	sulfides in altered basalt, quartz veins	Emery east shaft	6.4
E-44-1PY	pyrite	sulfides in silicified basalt, quartz veins	Sterret mine	7.0
E-44-1SP	sphalerite	sulfides in silicified basalt, quartz veins	Sterret mine	6.1
E-44-1GL	galena	sulfides in silicified basalt, quartz veins	Sterret mine	3.3
E-44-2AP	arsenopyrite	sulfides in silicified basalt, quartz veins	Sterret mine	6.3
E-46-1GL	galena	sulfides in altered basalt, quartz veins	Monday mine	4.1
E-46-1SP	sphalerite	sulfides in altered basalt, quartz veins	Monday mine	6.4
E-46-1PY	pyrite	sulfides in altered basalt, quartz veins	Monday mine	8.1
E-47-1PY	pyrite	sulfides in altered basalt, quartz veins	Monday mine	5.9
E-47-1SP	sphalerite	sulfides in altered basalt, quartz veins	Monday mine	7.2
E-48-1PY	pyrite	altered basalt with disseminated pyrite	Monday mine	6.7
E-49-1GL	galena	disseminated sulfides in altered basalt	Monday mine	4.3
E-49-1PY	pyrite	disseminated sulfides in altered basalt	Monday mine	6.7
E-51-1GL	galena	quartz veins in altered basalt, sulfides	Wednesday mine	3.7
E-51-1PY	pyrite	quartz veins in altered basalt, sulfides	Wednesday mine	7.3
E-51-2PY	pyrite	quartz veins in altered basalt, sulfides	Wednesday mine	6.4
E-53-1PY	pyrite	argillicly altered basalt with pyrite	Wednesday mine	8.8
E-55-1GL	galena	quartz vein with disseminated sulfides	Paymaster mine	1.3
E-55-1PY	pyrite	quartz vein with disseminated sulfides	Paymaster mine	5.7
E-55-2SP	sphalerite	quartz vein with disseminated sulfides	Paymaster mine	3.4
E-55-2GL	galena	quartz vein with disseminated sulfides	Paymaster mine	1.0
E-55-2PY	pyrite	quartz vein with disseminated sulfides	Paymaster mine	5.5

Sample No.	Mineral	Sample Description	Location	$\delta^{34}S‰$
E-55-2AP	arsenopyrite	quartz vein with disseminated sulfides	Paymaster mine	3.1
E-56-1SP	sphalerite	quartz vein with disseminated sulfides	Paymaster mine	3.9
E-56-1AP	arsenopyrite	quartz vein with disseminated sulfides	Paymaster mine	3.6
E-56-1GL	galena	quartz vein with disseminated sulfides	Paymaster mine	1.9
E-56-1PY	pyrite	quartz vein with disseminated sulfides	Paymaster mine	5.9
E-62-1GL	galena	quartz veins with disseminated sulfides	Paymaster mine	1.3
E-62-1PY	pyrite	quartz veins with disseminated sulfides	Paymaster mine	5.1
E-62-2SP	sphalerite	quartz veins with disseminated sulfides	Paymaster mine	3.8
E-62-2GL	galena	quartz veins with disseminated sulfides	Paymaster mine	2.3
E-65-1PY	pyrite	altered basalt with disseminated pyrite	Paymaster mine	8.6
E-67-1PY	pyrite	amygdaloidal basalt, pyrite in amygduals	prospect pit	6.5
E-68-1PY	pyrite	amygdaloidal basalt, disseminated pyrite	prospect pit	8.6

Table A 4: $\delta^{13}C$ (VPDB) and $\delta^{18}O$ (VPDB, VSMOW) from carbonate minerals

Sample No.	Mineral	Lab	$\delta^{13}C$ (VPDB, ‰)	$\delta^{18}O$ (VPDB, ‰)	$\delta^{18}O$ (VSMOW, ‰)
E3	Kutnohorite	University of Nevada-Reno	-7.2	-15.4	14.9
E31	Kutnohorite	University of Nevada-Reno	-5.3	-16.3	14.0
E70	Dolomite	University of Nevada-Reno	-2.7	-20.3	10.0
E13	Dolomite	University of Nevada-Reno	-6.0	-14.2	16.1
E20	Dolomite	University of Nevada-Reno	-5.0	-15.9	14.4
E9	Ankerite	University of Nevada-Reno	-4.5	-16.4	13.9
E36	Ankerite	University of Nevada-Reno	-3.9	-22.4	7.9
E63	Ankerite	University of Nevada-Reno	-1.0	-25.5	4.8
E60	Calcite	University of Nevada-Reno	-3.0	-19.2	11.1
E30	Calcite	University of Nevada-Reno	-2.4	-16.2	14.1
E57	Calcite	University of Nevada-Reno	-1.4	-26.9	3.4
Em-39	Unknown	UWY	-3.4	-20.8	9.5
P-15	Unknown	UWY	-4.0	-20.8	9.5
Em-41	Unknown	UWY	-2.8	-20.0	10.3
Em-38	Unknown	UWY	-3.6	-19.5	10.8
A-17	Unknown	UWY	-5.8	-13.5	16.8
Em-39	Unknown	UWY	-3.6	-20.2	10.1
Em-35	Unknown	UWY	-5.0	-16.5	13.8
Em-40	Unknown	UWY	-7.1	-16.6	13.7
A-13	Unknown	UWY	-1.5	-26.1	4.2
Em-28	Unknown	UWY	-6.5	-16.6	13.7
Em-27	Unknown	UWY	-5.8	-16.9	13.4
Em-36	Unknown	UWY	-5.6	-18.4	11.9
Em-32	Unknown	UWY	-5.4	-19.4	10.9
A-14	Unknown	UWY	-4.4	-18.1	12.2

Appendix B: Photographs

Paymaster

P-1: Sample contains large grains of sphalerite with pyrite, galena with milky and clear vein quartz.

P-2: Replaced breccia clasts by subhedral to euhedral pyrite with some sphalerite. Lighter color patches are carbonate-quartz. Matrix is dark gray and fine grained.

P-3: Galena and pyrite around outside of quartz-carbonate. Pyrite near these grains is large. Disseminated chalcopyrite near replaced wallrock with sphalerite, boulangerite, and galena.

P-4: Between bands of carbonate are bands of pyrite and arsenopyrite around brecciated pyrite and quartz.

P-5: Coarse-grained milky to translucent and zoned quartz with pyrite, sphalerite, and galena. Smaller patches of chalcopyrite.

P-6: Banded quartz-carbonate with veinlet of pyrite and fine-grained sphalerite and galena

P-8: Silicified breccia with pyrite and disseminated sulfides.

P-9: Brecciated carbonate-quartz-sulfides.

P-10: Chalcedony-carbonate breccia with propyliticly altered clasts. Carbonate (calcite?) crystals on top. Quartz-pyrite replace edges of clasts.

P-14: Subhedral well zoned quartz with interstitial galena.

Emery

Em-1: Propylitic alteration of amygdaloidal rock with a carbonate vein and carbonate infilling a fracture.

Em-2: Propylitic alteration with quartz-carbonate veinlet. Color difference in groundmass may be due to weathering.

Em-4: Carbonate vein cut and replaced by typical gray vein quartz. Rock is propylitically altered with argillic overprinting.

Em-6: Silicic alteration overprinting sericitic alteration, indicated by the pyrite

Em-7: Vein section with milky quartz vein and altered wall rock.

Em-9: Typical banded vein section

Em-13: Brecciated arsenopyrite-pyrite with comb quartz.

Em-14: Vein section attached to wall rock. Vein is quartz-sulfide with carbonates next to the wall rock.

Em-15: Sulfide-quartz vein with milky to translucent massive to comb quartz

Em-16: Vein section with wall rock clasts on bottom.

Em-17: Brecciated vein section. Quartz pieces have been rounded.

Em-18: Brecciated vein section.

Em-19: Minor quartz-pyrite-arsenopyrite veinlet.

Em-21: Wall rock replaced by pyrite. Banded vein section. Minerals from left to right: pyrite/arsenopyrite to sphalerite to arsenopyrite to thick band of pyrite to sphalerite to boulangerite/sphalerite to pyrite to sphalerite to pyrite/arsenopyrite

Em-21: Vein section. Banded sulfides surround a milky quartz vein.

Em-23: Amygdaloidal basaltic andesite with altered plagioclase. Groundmass altered to green with reddish carbonate material.

Em-24: Fine grained pyroxene basaltic andesite. Groundmass black to green-black with pyroxene phenocrysts.

Em-26: Very fine grained. Groundmass black with phenocrysts of pyroxene.

Em-27: Heavily altered wall rock. Groundmass is altered to cream and gray with saponite and pervasive pyrite. Veinlets of pyrite, quartz, sphalerite, and galena.

Em-28: Amygdaloidal basaltic andesite with pervasive pyrite. Groundmass is cream-green with some saponite. Amygdules filled with chalcedony/quartz or carbonate.

Em-29: Carbonate breccia. Clasts replaced by carbonate and chalcedony. Clast groundmass is dark green with some pyrite.

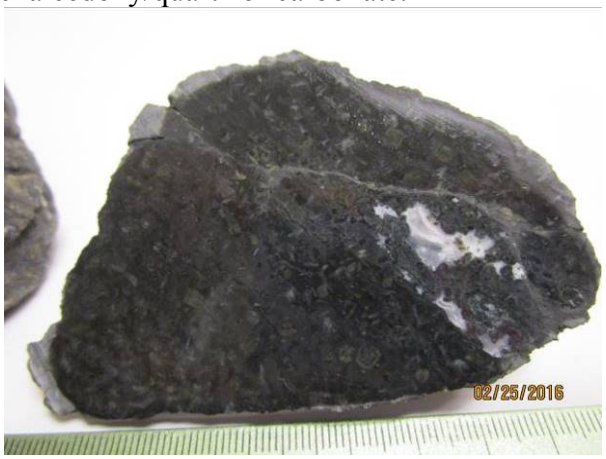

Em-30: Porphyritic feldspar-pyroxene basaltic andesite. Slightly propylitically altered, visible in pyroxenes. Area near amygdule high in carbonate.

EM-32: Amygdaloidal basaltic andesite with pervasive pyrite. Groundmass color varies from cream to gray to yellow-green. Stringers of sphalerite and carbonate present. Top of sample shows open-space growth in quartz and weathered sphalerite.

Em-33: Vein material galena, sphalerite, pyrite, quartz and carbonate on top of bleached wall rock with saponite and pervasive pyrite.

Em-35: Amygdaloidal basaltic andesite. Groundmass cream to light gray with pyrite throughout. Saponite present. Amygdules filled with chalcedony/quartz. Vein is pyrite, sphalerite, boulangerite, and quartz.

Em-36: Carbonate veining in heavily altered wall rock. Wall rock contains pyrite. Groundmass is grayish-green and silicified.

Em-37: Amygdaloidal basaltic andesite. Plagioclase altered to orange-brown. Groundmass is pea soup green. Amygdules filled with dark green (chlorite) and chalcedony.

Em-38: Amygdaloidal basaltic andesite propylitically altered. Groundmass is pale green. Amygdules dark green (chlorite) to filled with chalcedony/carbonate.

Em-39: Carbonate breccia. Clasts altered by carbonate-rich fluids. Clasts formerly amygdaloidal basaltic andesite.

Em-40: Altered porphyritic feldspar basaltic andesite with pervasive pyrite. Carbonate vein of ankerite (?). Groundmass pale green.

Argus

A-5: Carbonate breccia cemented by sulfides.

A-7: Fracture filling of alternating quartz and carbonate.

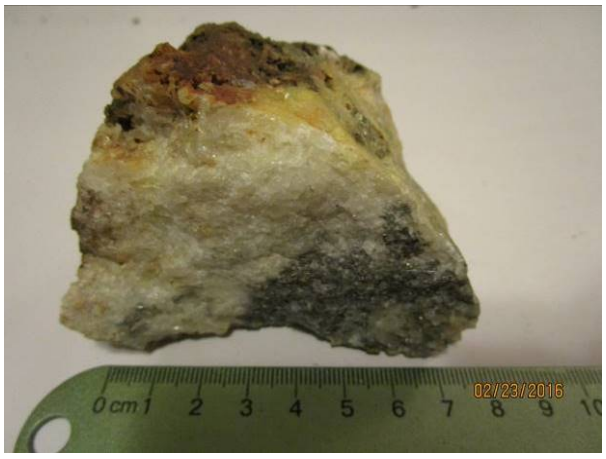

A-8:Comb quartz with arsenopyrite.

A-12: Massive quartz with pods of galena.

A-13: Weathered carbonate alteration.

A-14: Cut by carbonate veinlets and stringers. Sample is argillicly altered.

Emma Darling

ED-1: Propylitic alteration of basaltic andesite.

ED-3: Amygdaloidal with altered plagioclase and pyroxene. Vein is sphalerite, pyrite, and boulangerite. Sample wetted for picture.

ED-5: Quartz intergrown with pyrite.

ED-6: Propylitic alteration of porphyritic feldspar basaltic andesite

ED-7: Altered wallrock with sph-gal vein

ED-8: Altered porphyritic feldspar basaltic andesite. Plagioclase are altered. Pyrite pervasive and in two veinlets.

ED-10: Breccia ore vein section. Slab is slightly polished with some oxidation. Quartz and carbonate are intergrown with sulfides.

ED-11: Heavily altered amygdaloidal basaltic andesite. Pyrite pervasive in wall rock with preference for replacing amygdules. Vein is pyrite, sphalerite, boulangerite, and quartz.

ED-12: Slightly altered porphyritic feldspar-pyroxene basaltic andesite.

ED-13: Altered amygdaloidal basaltic andesite. Pyrite replacing amygdules.

ED-15: Carbonate breccia. Brown veining from carbonate weathering. Clasts are medium gray. Disseminated sulfides throughout.

Bonanza

B-1: Quartz-carbonate veinlet in propylitically altered wallrock

B-2: Breccia ore

B-4: Breccia ore

B-5:Propylitically altered wallrock with quartz-carbonate vein

B-6: Silicic alteration overprinting sericitic. Clasts are rounded to sub angular with sulfide-quartz veining

B-7: Sericitic alteration with stringers of quartz-sphalerite-pyrite and fine-grained sulfides. Pyrite pervasive through rock.

B-8: Sericitically altered clasts in disseminated quartz-sulfide matrix. Example of breccia ore.

B-9: Sericitic alteration of clasts with sulfide-quartz veins and a cross-cutting carbonate vein

B-10: Sericitic/argillic altered clasts in quartzt-sulfide matrix

B-11: Coarse arsenopyrite with some pyrite and disseminated sulfides in veinlets around sericiticly altered wall rock.

Hidden Hand

HHand-1: Silicified wallrock with disseminated sulfides

HHand-2: Argillic altered wall rock with quartz-sulfide veining.

HHand 4: Porphyritic feldspar basaltic andesite. Plagioclase and pyroxene are altered. Matrix is black-green with disseminated pyrite.

HHand 6: Silicified breccia. Clasts bleached with weathered out pyrite molds. Quartz veining contains disseminated sulfides.

HHand 7:Silicified breccia. Clasts altered and weathered. Remnant plagioclase laths visible. Quartz veining contains Fe-oxides.

HHand 8: Silicified breccia. Clasts heavily altered and weathered. Quartz veining contain Fe-oxides.

HHand 9: Silicified breccia. Quartz veins contain disseminated sulfides. Clasts are heavily altered but still have outlines of replaced plagioclase and pyroxene.

HHand 10: Silicified breccia. Quartz veins contain disseminated sulfides. Clasts heavily altered but still have outlines of replaced plagioclase and pyroxene.

HHand 11: Clast from silicified breccia. Some quartz veinlets. Replaced plagioclase and pyroxene visible as white spots on picture.

Thin Sections

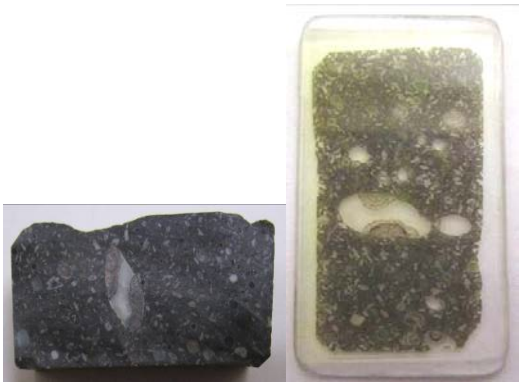

KCS-13-22

KCS-13-24

E26

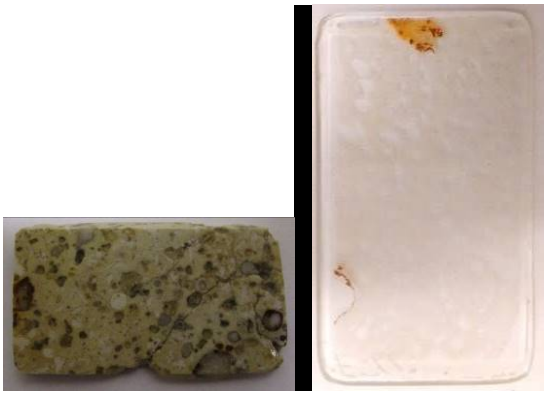

E66

E4

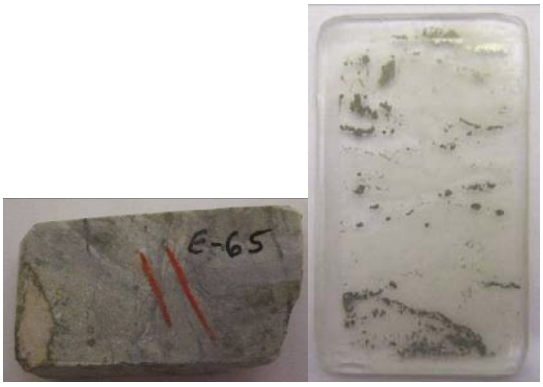

E65

E57

E69

E48

E25

E68

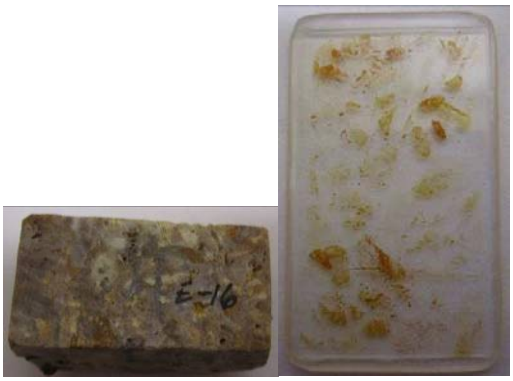

E16

E7

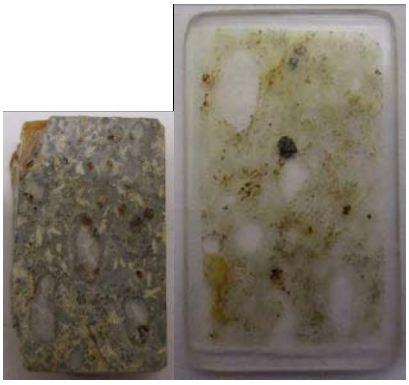

E67

E53

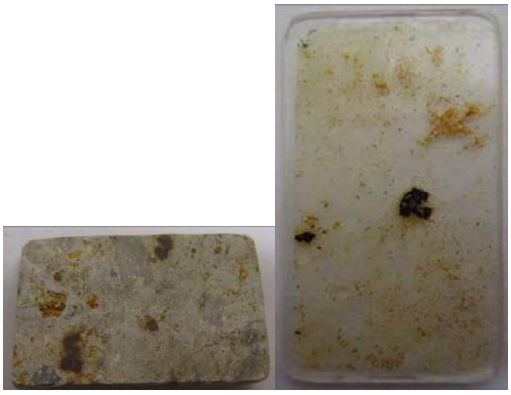

E43

E9

E11

SIGNATURE PAGE

This is to certify that the thesis prepared by Jarred Zimmerman entitled "Reexamination of the ore-forming processes in the Emery mining district, Powell, Co., Montana" has been examined and approved for acceptance by the Department of Geological Engineering, Montana Tech of the University of Montana, on this 2nd day of August, 2016.

Chris Gammons, PhD, Professor
Department of Geological Engineering
Chair, Examination Committee

Diane Wolfgram, PhD, Professor
Department of Geological Engineering
Member, Examination Committee

Stan Korzeb, Economic Geologist, Research Professor
Montana Bureau of Mines and Geology
Member, Examination Committee